Technical Report No. 1
Document No. P-7376-TR1
Contract No. NAS 5-25341
June 1979

Prepared for
NASA Goddard Space Flight Center
Greenbelt, Maryland 20771

Handbook for the estimation of microwave propagation effects — link calculations for earth-space paths

(Path Loss and Noise Estimation)

Robert K. Crane
David W. Blood

ENVIRONMENTAL RESEARCH & TECHNOLOGY, INC.
CONCORD, MA • LOS ANGELES • ATLANTA • PITTSBURGH
FORT COLLINS, CO • BILLINGS, MT • HOUSTON • CHICAGO

1. Report No.	2. Government Accession No.	3. Recipient's Catalog No.

4. Title and Subtitle	5. Report Date
Handbook for the Estimation of Microwave Propagation Effects - Link Calculations for Earth-Space Paths (Path Loss and Noise Estimation)	June 1979
	6. Performing Organization Code: Technical Report No. 1
7. Author(s): Dr. Robert K. Crane and David W. Blood	8. Performing Organization Report No.: P-7376-TR1
	10. Work Unit No.
9. Performing Organization Name and Address: Environmental Research & Technology, Inc., 696 Virginia Road, Concord, Massachusetts 01742	11. Contract or Grant No.: NAS 5-25341
	13. Type of Report and Period Covered: Technical Report, Sept. 1978 to May 1979
12. Sponsoring Agency Name and Address: NASA Goddard Space Flight Center, Greenbelt, Maryland 20771, Technical Officer: Dr. Louis J. Ippolito	14. Sponsoring Agency Code

15. Supplementary Notes

The authors gratefully acknowledge the helpful consultations of Dr. L. Ippolito of NASA/GSFC during the period of reporting.

16. Abstract

This report provides the path loss and noise estimation procedures as the basic input to systems design for earth-to-space microwave links operating at frequencies from 1 to 300 GHz. Topics covered include gaseous absorption, attenuation by rain, scintillation, low elevation angle effects, radome attenuation, diversity schemes, noise emission by atmospheric gases, emission by rain and antenna contributions.

These sections are part of a handbook preparation project entitled "Handbook for the Estimation of Microwave Propagation Effects," to include point-to-point microwave and remote sensing systems design.

The models presented provide step-by-step procedures useful to system engineers in system design, evaluation and frequency management.

17. Key Words (Suggested by Author(s))	18. Distribution Statement
Microwave Propagation Communication Links Earth-space Satellite Paths Atmospheric Absorption Rain Attenuation Millimeter Waves	Unlimited

19. Security Classif. (of this report)	20. Security Classif. (of this page)	21. No. of Pages	22.
Unclassified	Unclassified	86	

TABLE OF CONTENTS

LIST OF ILLUSTRATIONS

LIST OF ILLUSTRATIONS (cont)

LIST OF ILLUSTRATIONS (cont)

LIST OF TABLES

1. INTRODUCTION

As satellite and earth relay communication services continue to expand in volume of usage, increased information bandwidth requirements, and new applications, a consistent demand will be toward the use of higher frequencies where permissible. The imminent use of millimeter wavebands (above 30 GHz) has prompted theoretical and experimental studies of the limitations imposed by the atmosphere on line-of-sight relay and earth-to-space (both up- and down-link) propagation paths. The studies have shown that limitations arise mainly from signal attenuation (absorption and scattering by the medium), noise emission (natural), or interference (man-made) produced in part or wholly by propagation phenomena. One of the principle causes of both attenuation, noise and potential interference is that caused by rain or hydrometeors. Although the physics of scattering by hydrometeors is well in hand (Crane, 1971), several different methodologies have developed to attempt to treat this particular phenomenon, having a totally statistical occurrence behavior as opposed to gaseous absorption and emission by the atmosphere which is continuously present with only a statistical variation about the mean. Attenuation caused by rain as well as the gaseous contribution increases significantly to many tens of decibels at the higher frequencies deeper into the millimeter wavebands.

It has therefore become imperative to have a consistent single model available for a standard of comparison for other models when dealing with rain attenuation problems in system design and experimentation at the higher frequencies. This report offers such a model as a proposed standard technique. The latest refinements to the Global Rain Prediction Model are incorporated in this handbook. The basic model (with fewer refinements) has previously been submitted for inclusion by the CCIR (CCIR, 1978a) as a handbook tool for general application. With a sizeable amount of measurement data from satellite links operating at frequencies up to 30 GHz now becoming available, the model can be easily evaluated beyond that accomplished at present. The model is also amenable to further refinements and updates as these data comparisons are made and additional higher frequency data become available. Cases of model usage and comparisons will be of extreme value, if fed back, to provide the basis of information on which these further refinements may be made.

The frequency range treated in this report is from 1 to 300 GHz (30 cm to 1 mm wavelengths). The gaseous attenuation model spans this range although caution should be exercised in its use at frequencies above 200 GHz due to theoretical uncertainties in the water vapor model. The rain model presented only covers the 1 to 100 GHz (30 cm to 3 mm wavelength) portion of the frequency range, although use at higher frequencies is possible given adequate relationships between specific attenuation and rain rate.

This report provides the path loss and noise estimation procedures as the basic input to system design for earth-to-space link calculations. These sections are part of a handbook preparation project for a complete manual entitled "Handbook for the Estimation of Microwave Propagation Effects." The handbook is designed to be used on three different levels, (1) for step-by-step system design, (2) as a source book for communication system evaluation and frequency management, and (3) for an up-to-date survey of microwave propagation physics. This section on link calculations for earth-space-paths defines the propagation models used for system parameter estimation and compares model predictions with observations. The propagation phenomena are only described in sufficient detail to be useful in system evaluation and frequency management. Other sections of the handbook provide a survey of the propagation physics, link calculations for ground-to-ground paths, and remote sensing system design. A goal for the complete project is to provide a treatment of available microwave data in a consistent manner with step-by-step procedures for system design, curves, and computer adaptable algorithms to simplify parameter estimation for the user.

2. PATH LOSS ESTIMATION

2.1 Gaseous Absorption

Of the phenomena affecting earth-to-space propagation paths at microwave frequencies, those due to gaseous absorption and rain are of prime importance in system planning. The first of these, signal strength attenuation due to atmospheric absorption, is of fundamental concern in system frequency selection, design and operation due to the strong frequency dependence produced by molecular absorption lines at frequencies above 20 GHz. Atmospheric absorption must be dealt with continuously, whereas the attenuation due to rain, clouds and fog, etc. must be treated statistically on a percent of time basis. The gaseous specific attenuation (dB/km) is predictable for a given set of layer parameters, e.g. sea level pressure, temperature and humidity. Figure 1 (CCIR, 1977) shows the absorption characteristics as a function of frequency for the spectrum from 1 GHz through RF, I.R. and optical frequencies. Here the attenuation (per unit distance) contribution of the gaseous constituents of the medium are compared with those due to rain, at different rainfall rates, and also due to fog. Though the overall attenuation characteristics are very complex, the discussion in this report is limited to wavelengths greater than one millimeter (frequencies below 300 GHz) where only four of the absorption bands are of concern.

2.1.1 Model

Molecular absorption experienced on a path operating at centimeter or millimeter wavelengths is due primarily to the atmospheric water vapor and oxygen content (Waters, 1976). The absorption bands are centered at frequencies of 22.2 GHz (H_2O), 60 GHz (O_2), 118.8 GHz (O_2), and 183 GHz (H_2O). The lower three of these bands are depicted in Figure 2 which presents the integrated zenith attenuation from 1 to 160 GHz. The total one-way attenuation is shown from different starting heights to the top of the atmosphere. The curves were computed (Crane, 1971) for temperate latitudes* and moderate absolute humidity conditions (7.5 g/m^3 at the surface).

*U.S. Standard Atmosphere, July, 45°N.

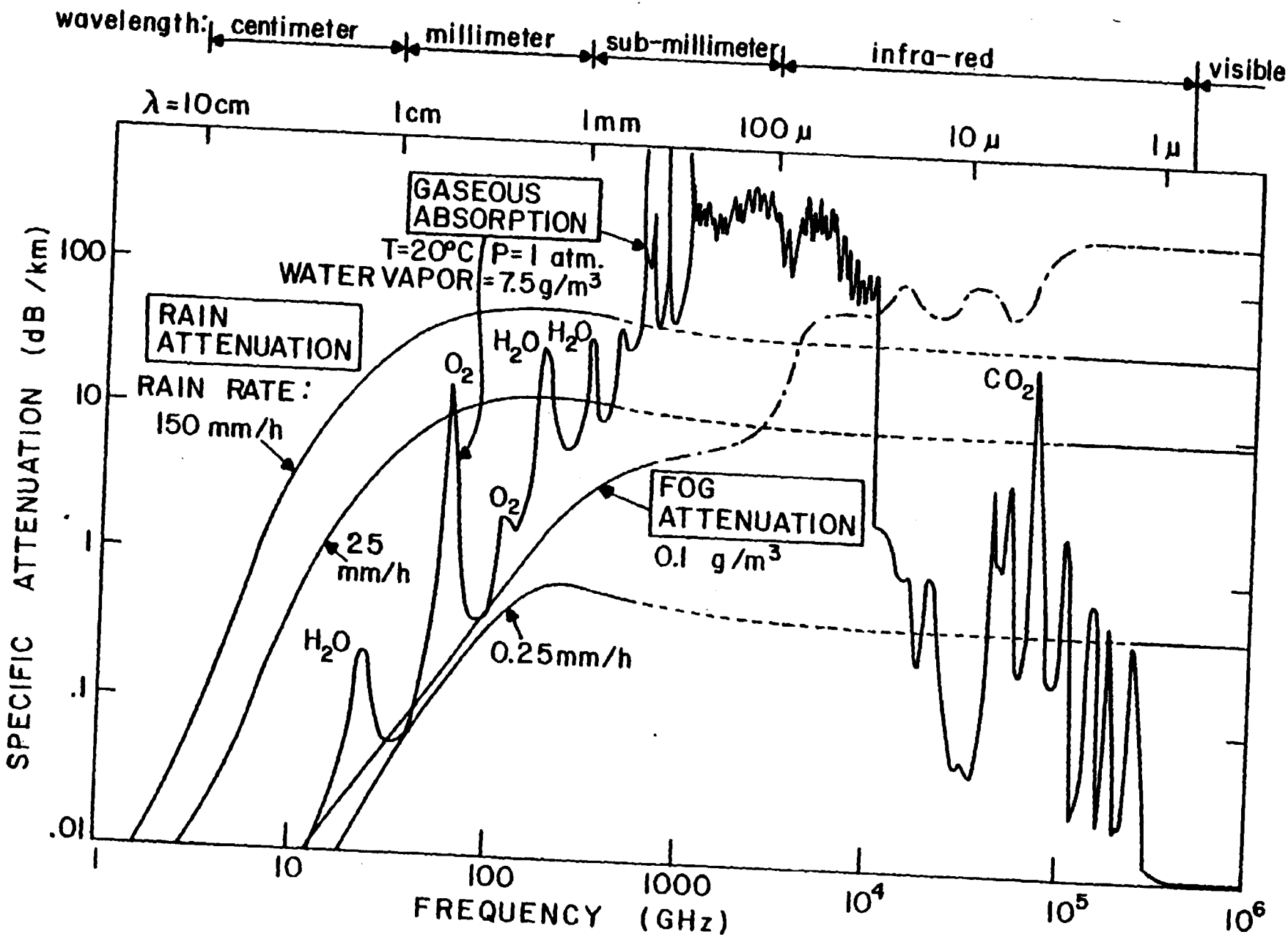

Figure 1 Specific attenuation due to gaseous constituents

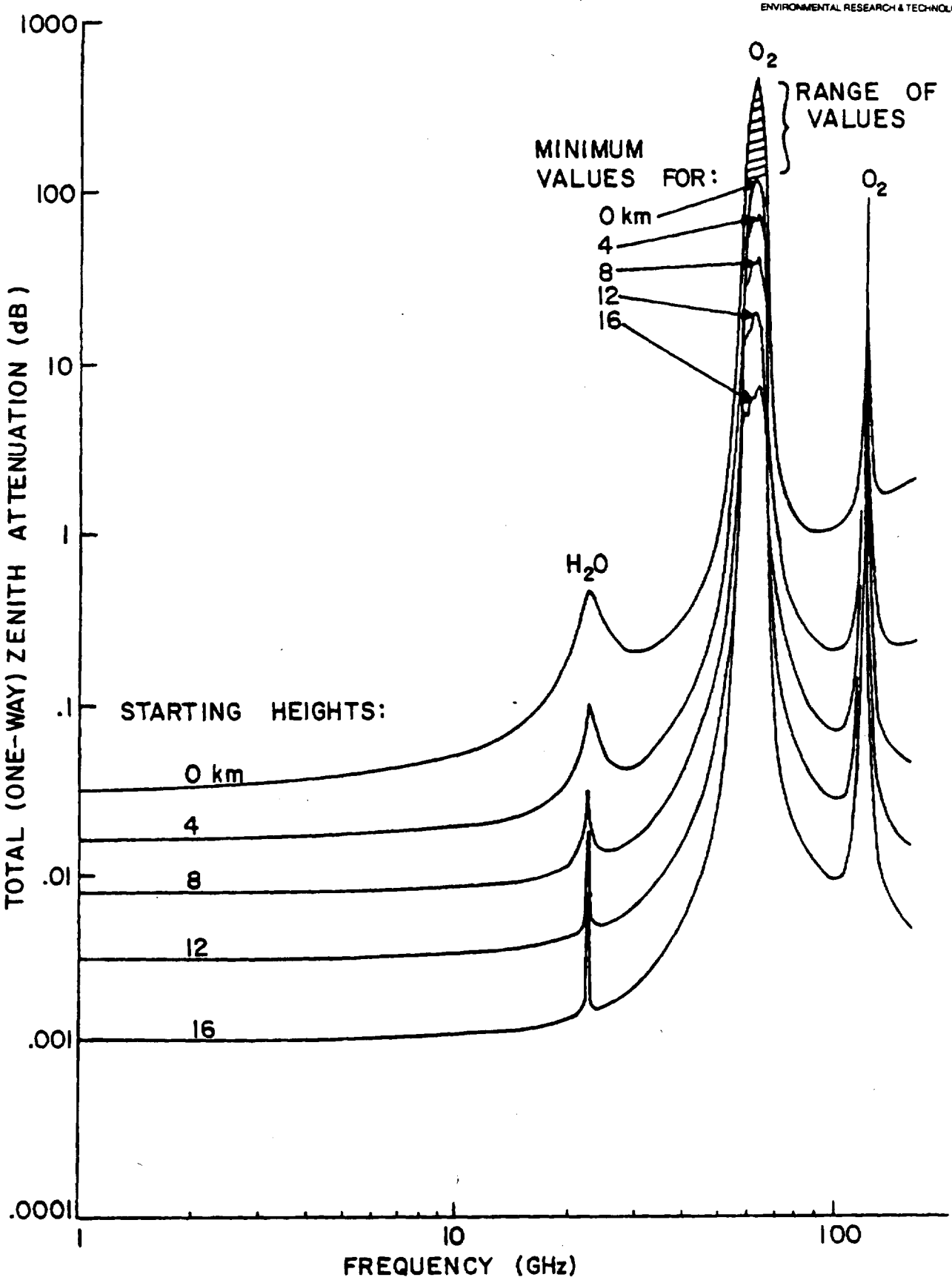

Figure 2 Theoretical one-way zenith attenuation from specified height to top of the atmosphere for a moderately humid atmosphere (ρ_o = 7.5 g/m^3 at the surface)

The mean zenith attenuation and standard deviation of attenuation for calculations made using a 220 profile sample of atmospheric conditions spanning all seasons and geographical locations (Crane, 1976), is presented in Figure 3. These results show, for example, that at frequencies between 30 and 35 GHz, the variability of water vapor and temperature produces less than a .14 dB (1σ) uncertainty in the zenith signal strength for a path from the surface to space. For oblique paths through the atmosphere, the attenuation as a function of elevation angle is given by the zenith attenuation multiplied by the cosecant of the elevation angle. The cosecant law does not hold for elevation angles less than about 6° due to earth curvature and refraction effects. Most satellite communications systems operate at elevation angles above 6° or a cosecant of 10. The maximum error introduced by using the above model for the computation of attenuation due to water vapor, therefore, is approximately 1.4 dB for frequencies in the 30 to 35 GHz range.

To obtain the total zenith attenuation at any geographic location, a more general model has been developed based on local surface absolute humidity and temperature. A regression analysis based on global data (Crane, 1976) yields a computation of the total zenith attenuation (τ_{90}) using the following relationship:

$$\tau_{90} = a + b\rho_0 - c\,T_0 \quad \text{(dB)} \tag{1}$$

where τ_{90} = total zenith attenuation from the surface to the top of the atmosphere (dB)

ρ_0 = mean local surface absolute humidity (g/m^3)

T_0 = mean local surface temperature (°C)

a,b,c = empirical coefficients derived from model (Table 1 and Figure 4) at appropriate frequency

The use of the more general model using local surface data produces a reduction in the (1σ) zenith attenuation variability (uncertainty) to about .035 dB at frequencies between 30 and 35 GHz for the case cited above.

To obtain the oblique path attenuation due to gaseous absorption, a cosecant law approximation may be used to 6° elevation as illustrated in Figure 5. The moderate humidity (ρ_s = 7.5 g/m^3) mid-latitude model

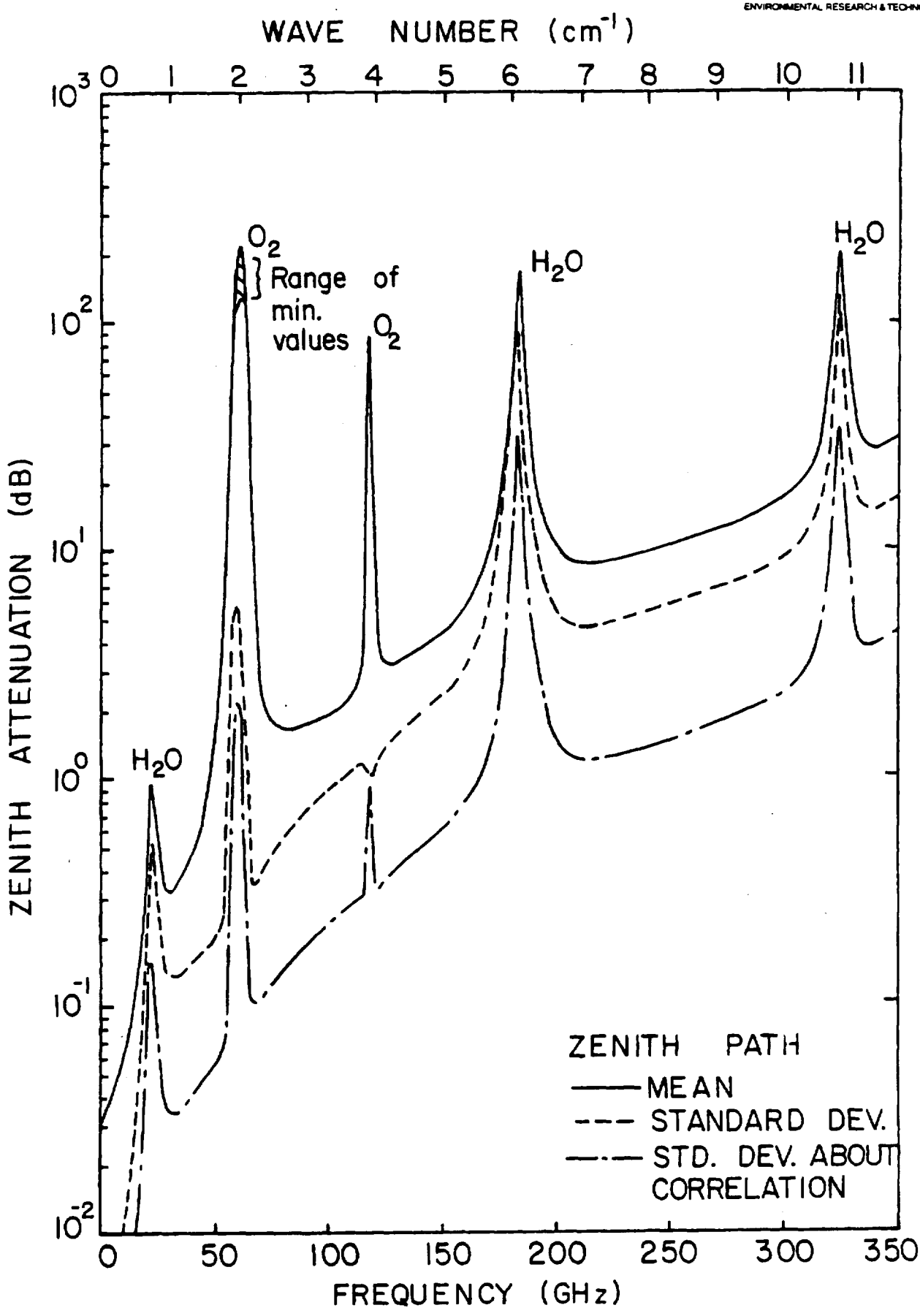

Figure 3 Total zenith attenuation (dB) and deviation about the all season and location mean (dB) for a one-way path through the atmosphere from the surface

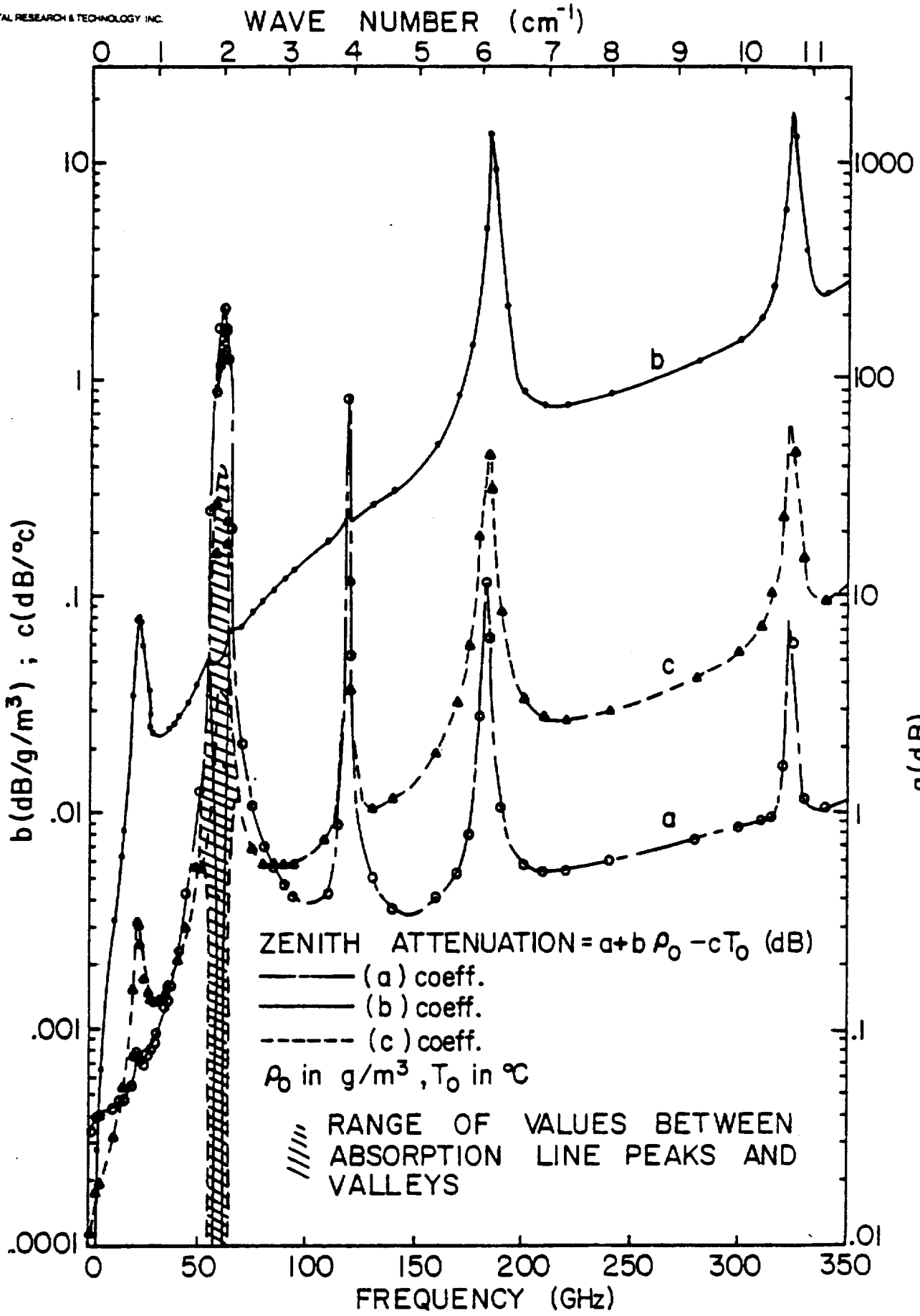

Figure 4 Coefficients a, b and c for equation 1 to compute the total zenith attenuation (τ_{90}) knowing the surface conditions

TABLE 1

COEFFICIENTS FOR COMPUTING TOTAL ZENITH ATTENUATION:

$$\tau_{90} = a + b\,\rho_o - c\,T_o \quad (dB)$$

Frequency F - GHz	Coefficients a(F)	b(F)	c(F)
1	3.3446E-02	2.7551E-06	1.1189E-04
2	3.6196-02	2.7567E-06	1.3327-04
4	3.9669E-02	2.7599E-04	1.7620E-04
6	4.0448E-02	6.5086E-04	1.9645E-04
12	4.3596E-02	3.1768E-03	3.1470E-04
15	4.6138E-02	6.3384E-03	4.5527E-04
16	4.7195E-02	8.2112E-03	5.3568E-04
20	5.6047E-02	3.4557E-02	1.5508E-03
22	7.5989E-02	7.8251E-02	3.0978E-03
24	6.9102E-02	5.9116E-02	2.4950E-03
30	8.5021E-02	2.3728E-02	1.3300E-03
35	1.2487E-01	2.3681E-02	1.4860E-03
41	2.3683E-01	2.8402E-02	2.1127E-03
45	4.2567E-01	3.2766E-02	2.9945E-03
50	1.2671E 00	3.9155E-02	5.7239E-03
55	2.4535E 01	4.8991E-02	-1.2125E-03
70	2.1403E 00	7.3246E-02	1.0436E-02
80	7.0496E-01	9.5860E-02	5.8635E-03
90	4.5760E-01	1.2185E-01	5.7369E-03
94	4.1668E-01	1.3320E-01	5.9439E-03
110	4.3053E-01	1.8465E-01	7.8499E-03
115	8.9351E-01	2.0292E-01	1.1297E-02
120	5.3532E 00	2.2125E-01	3.6311E-02
140	3.6788E-01	3.1894E-01	1.1941E-02
160	4.1446E-01	5.0635E-01	1.9078E-02
180	2.8087E 00	5.0360E 00	1.9198E-01
200	5.6172E-01	8.9655E-01	3.3943E-02
220	5.4358E-01	7.7720E-01	2.7580E-02
240	6.0124E-01	8.7887E-01	3.0693E-02
280	7.5941E-01	1.2220E 00	4.2753E-02

TABLE 1

(continued)

Frequency F - GHz	Coefficients		
	a(F)	b(F)	c(F)
300	8.5290E-01	1.5400E 00	5.5148E-02
310	9.0485E-01	1.9747E 00	7.3496E-02
320	1.6584E 00	6.1318E 00	2.3785E-01
330	1.1328E 00	3.9445E 00	1.5540E-01
340	1.0722E 00	2.5597E 00	9.6881E-02
350	1.2005E 00	2.9613E 00	1.1381E-01

(labeled M) is shown for the total zenith attenuation from the surface ($\theta = 90°$). The oblique attenuation (total atmospheric loss, L_{atm}) may be obtained by:

$$= \frac{1}{\sin\theta}\left[a + b\rho_o - c\,T_o\right]$$

$$L_{atm} = \tau_{90} \cdot \text{cosecant } (\theta) \qquad \text{(dB)} \qquad (2)$$

for $\theta > 6°$ elevation

For elevations below six degrees, the attenuation may be estimated by interpolating between the 6° and 0° (horizontal) elevation attenuation curves. The latter was obtained by raytracing over the 0° elevation path through the atmosphere starting at the surface height and obtaining the line integral of attenuation along the ray path.

2.1.2 Procedure

The following steps may be used to obtain the total gaseous absorption over an earth-to-space propagation path:

Step 1 - Obtain the appropriate mean surface absolute humidity $\rho_o(g/m^3)$, for example, from the maps of Figure 6a, February or 6b, August (Bean and Dutton, 1966), and the mean surface temperature T_0 (°C).

Step 2 - Compute the zenith attenuation using equation (1) with values of a, b and c from Figure 4 at the required frequency.

Step 3 - Compute the oblique path attenuation (L_{atm}) at the desired elevation angle (θ) using equation (2), $\theta > 6°$ el. or by interpolation as described, $\theta < 6°$ el.

2.1.3 Comparison with Experiment

The multiple regression zenith attenuation model, derived from 220 profile samples of general atmospheric conditions, is shown in Figure 7 compared with measurements. The frequency, 22.235 GHz, is within the water vapor absorption band. The mean surface temperature from the global sample set was 14.6°C. Shown also in the figure is the theoretical trend obtained by Waters which has a dependency only on ρ_o. For the limited number of measurements, either line could be described as representative of the observations and the model including a surface temperature

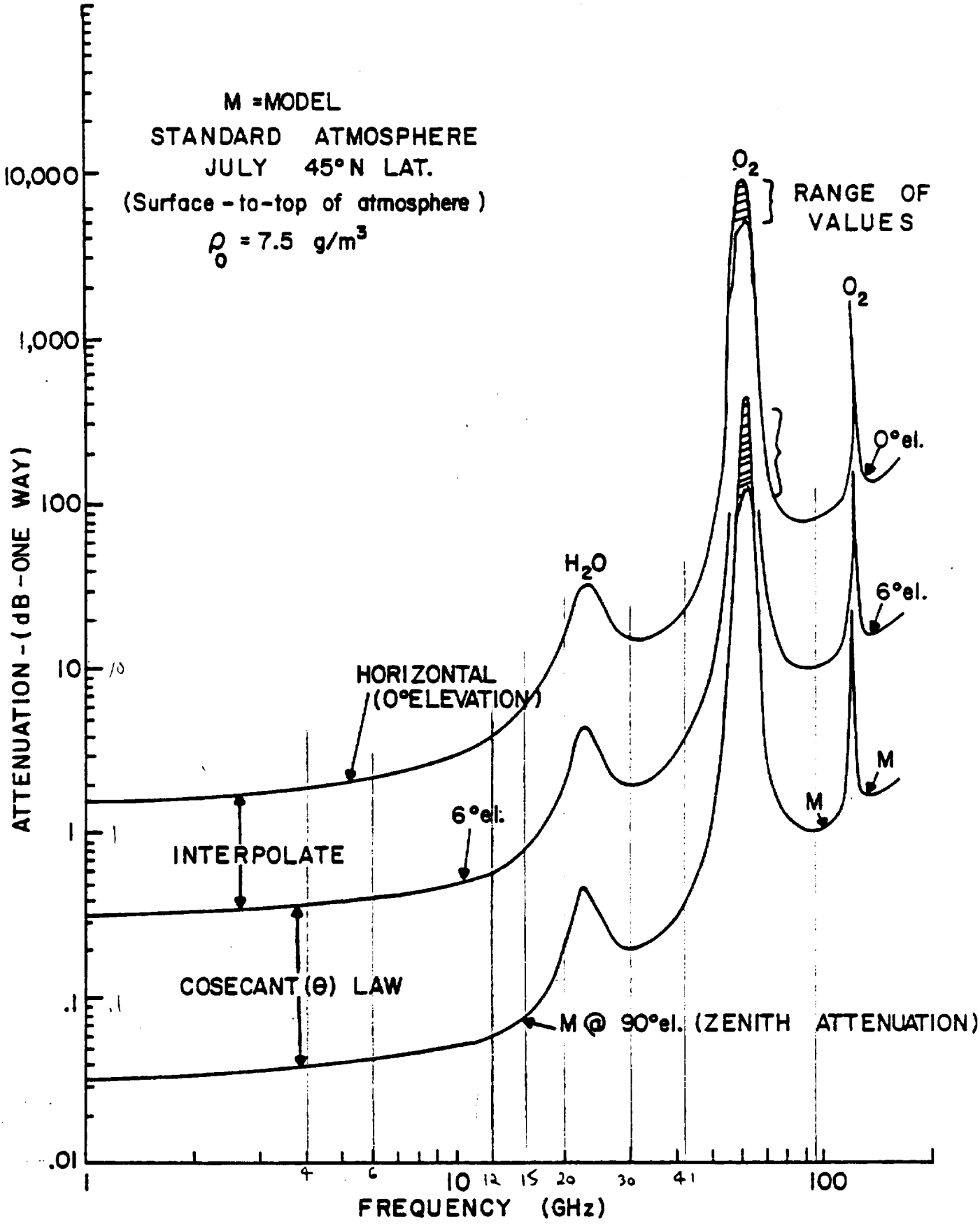

Figure 5 Illustration of oblique path attenuation through the atmosphere compared with the zenith model value (M)

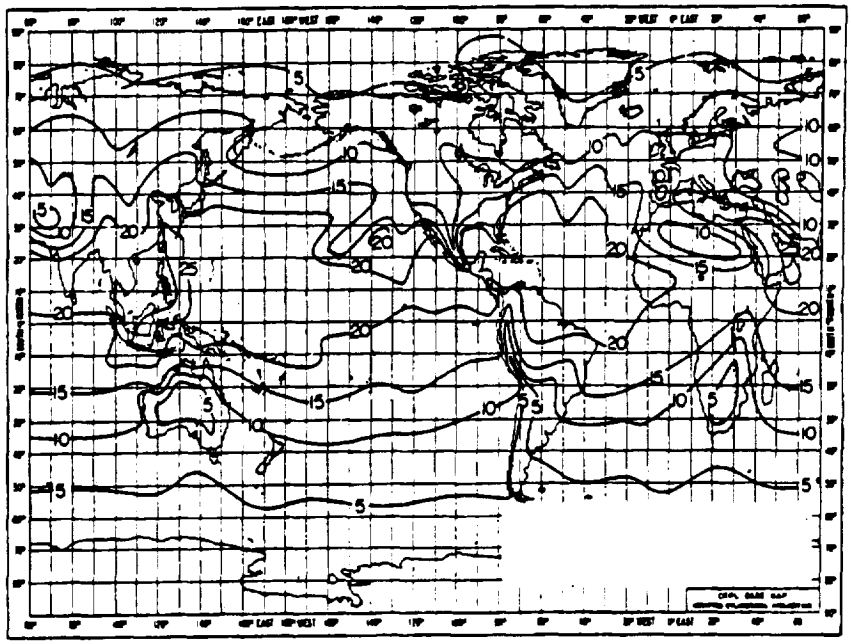

a) FEBRUARY

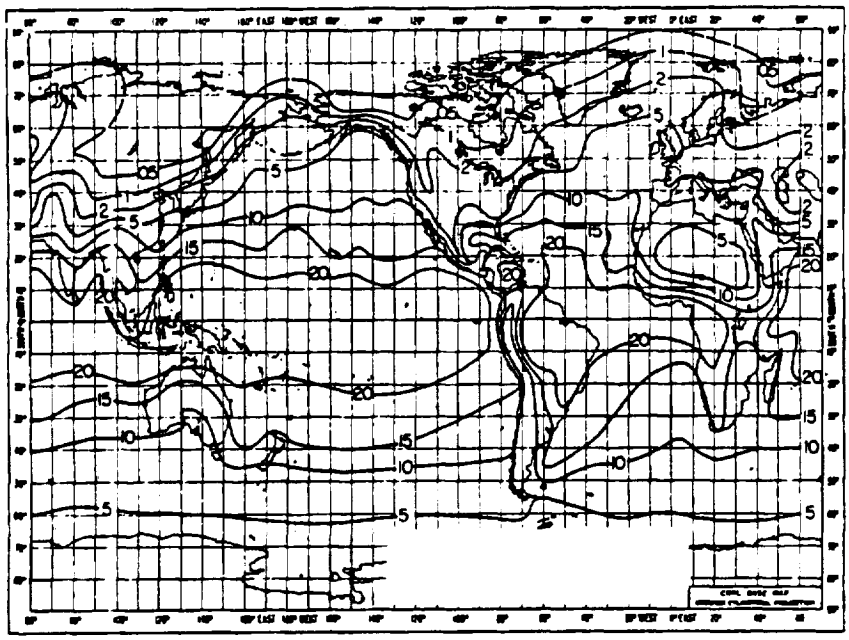

b) AUGUST

Figure 6 Global map of (ρ_o) average absolute humidity (g/m^3) at the surface [Bean and Dutton, 1966] for February and August

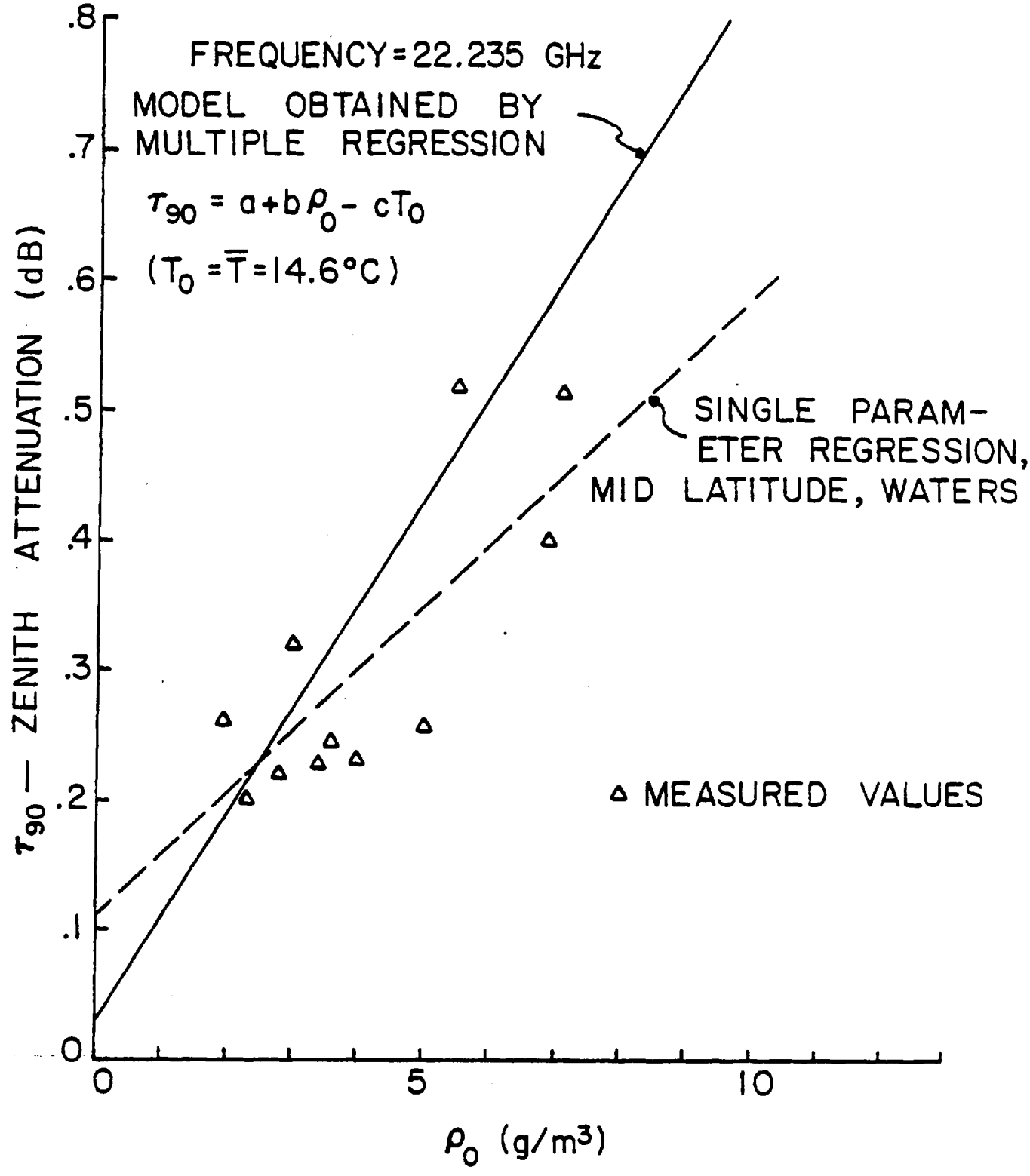

Figure 7 Comparison of humidity dependence of zenith attenuation computed (equation 1) with measured values at 22.235 GHz

dependence is reasonably well supported.

2.2 Attenuation by Rain

Rain-caused attenuation affects, in a major way, earth-space propagation paths operating at centimeter or millimeter wavelengths. When rainy weather is experienced along the link, the system performance will degrade in ways which may be reliably estimated. However, due to the randomness of the events occurring in the troposphere, only statistical predictions can be considered which factor into system designs. Recent modelling based on a global climatology of rain (Crane, 1977a; Crane, 1979b) has provided a means of coupling the rain statistics with the attenuation theory. These results are described here for the purpose of system design and prediction rather than elaborating on the theory or background covered in the references. Several comparisons with experimental results support the model (Crane, 1979b) and argue for its adoption for general application to system design.

2.2.1 Model

The model described is used for the estimation of the annual attenuation distribution to be expected on a specific propagation link. It differs from some of the models currently available in that it is based entirely on meteorological observations, not attenuation measurements. The model was tested by comparison with attenuation measurements. This procedure was used to circumvent the requirement for attenuation observations over a span of many years. The model is an extension of the Global Prediction Model developed by Crane for the 1978 CCIR Special Preparatory Meeting (CCIR, 1978a). The model is based upon the use of independent, meteorologically derived estimates for the cumulative distributions of point rainfall rate, horizontal path averaged rainfall rate, the vertical distribution of rain intensity, and upon a theoretically derived relationship between specific attenuation and rain rate obtained using median observed drop size distributions at a number of rain rates.

The first step in application of the model is the estimation of the instantaneous point rain rate distribution (R_p). The Global Prediction Model provides median distribution estimates for broad geographical regions; eight climate regions A through H are designated to classify

regions covering the entire globe. Figures 8 and 9 show the geographic rain climate regions for the continental and ocean areas of the earth. The United States and European portions are further expanded in Figures 10 and 11, respectively.

The climate regions depicted by the global model are very broad. The upper and lower rain rate bounds provided by the nearest adjacent region have a ratio of 3.5 at 0.01 percent of the year for the proposed CCIR climate region D, for example, producing an attendant ratio of upper-to-lower bound attenuation values of 4.3 dB at 12 GHz. This uncertainty in the estimated attenuation value can be reduced by using rain rate distributions tailored to a particular area if long term statistics are available. For convenience, region D has further been subdivided into regions D_1, D_2 and D_3 for the United States area only (Figure 10).

The values of R_p may be obtained from the rain rate distribution curves of Figure 12. Figure 12a shows the curves for the eight global climate regions designated A through H for one minute averaged surface rain rate as a function the percent of year that rain rate is exceeded. The distributions for the Region D subdivisions are shown in Figure 12b. Numerical values for R_p are provided in Table 2.

A path averaged rainfall rate ($R_{path} = \bar{R} = rR_p$, where r is defined as the effective path average factor) is useful for the estimation of attenuation for a line-of-sight radio relay system but, for the estimation of attenuation on a slant path to a satellite, account must be taken of the variation of specific attenuation with height. The atmospheric temperature decreases with height and, above some height, the precipitation particles must all be ice particles. Ice or snow do not produce significant attenuation; only regions with liquid water precipitation particles are of interest in the estimation of attenuation. The size and number of rain drops per unit volume may vary with height. Measurements made using weather radars show that the reflectivity of a rain volume may vary with height but, on average, the reflectivity is roughly constant with height to the height of the 0°C isotherm and decreases above that height. The rain rate may be assumed to be constant to the height of the 0°C isotherm at low rates and this height may be used to define the upper boundary of the attenuating region. A high correlation between the 0°C height and the height to which liquid rain

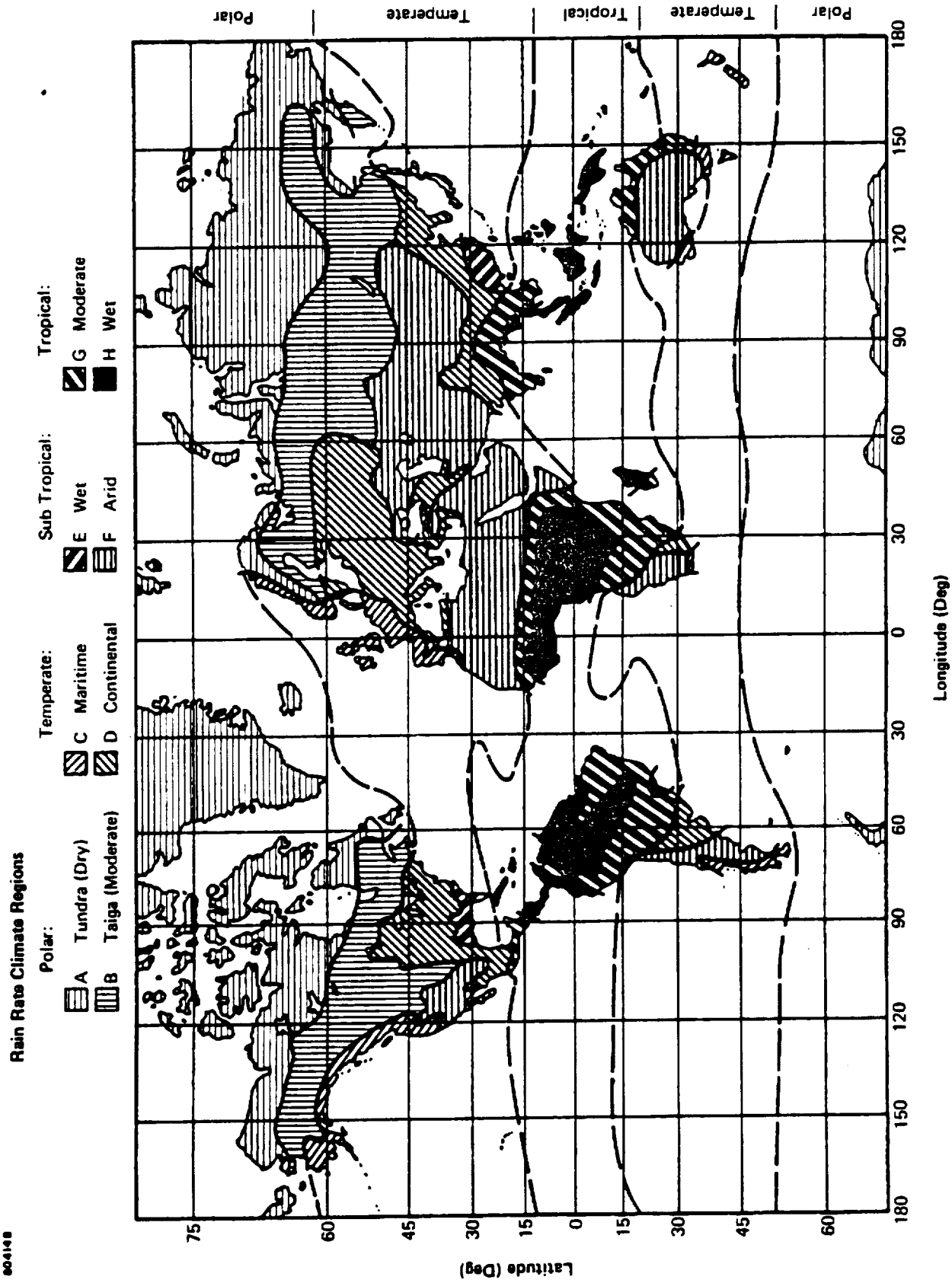

Figure 6 Global rain rate climate regions for the continental areas.

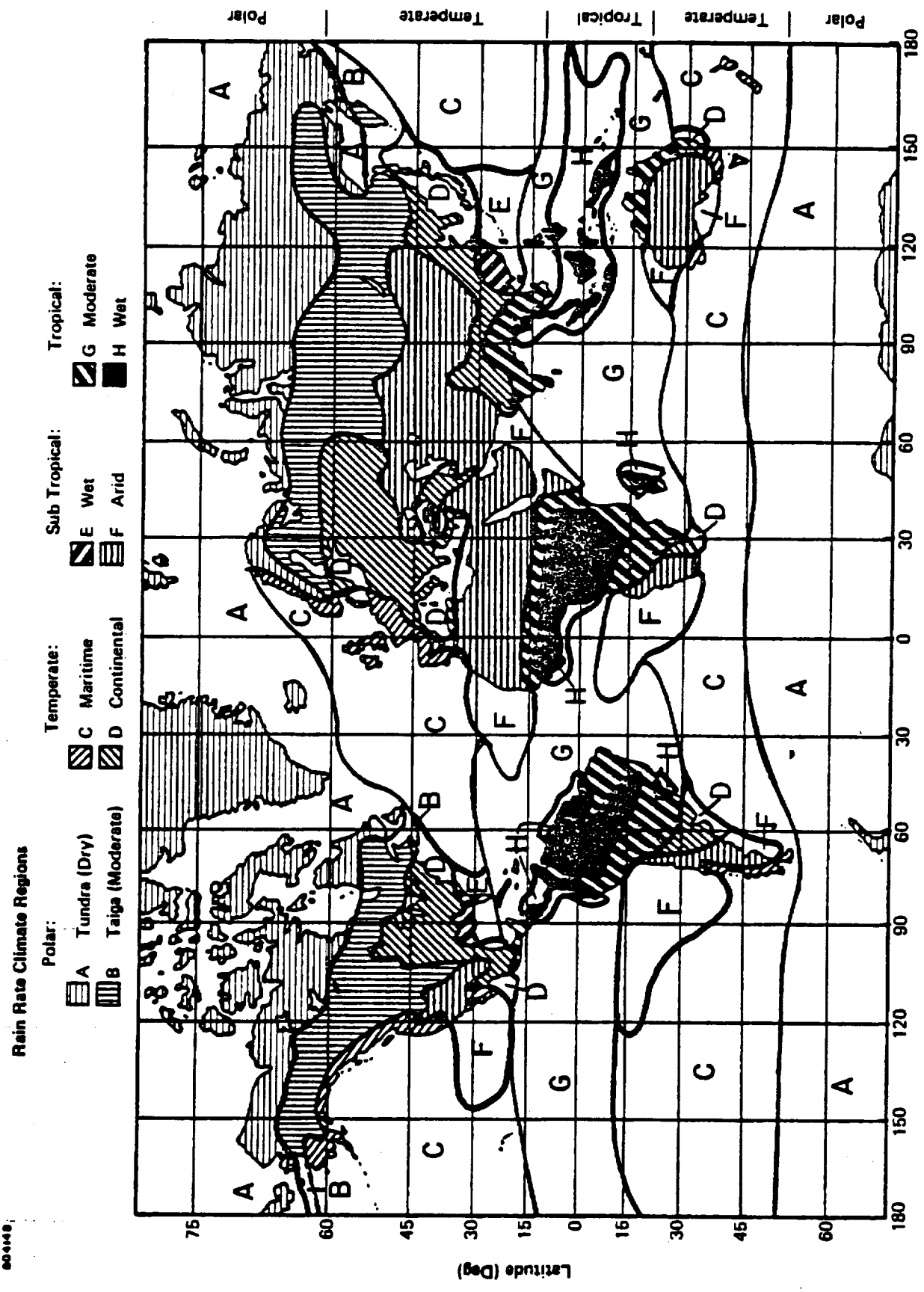

Figure 9 Global rain rate climate regions including the ocean areas

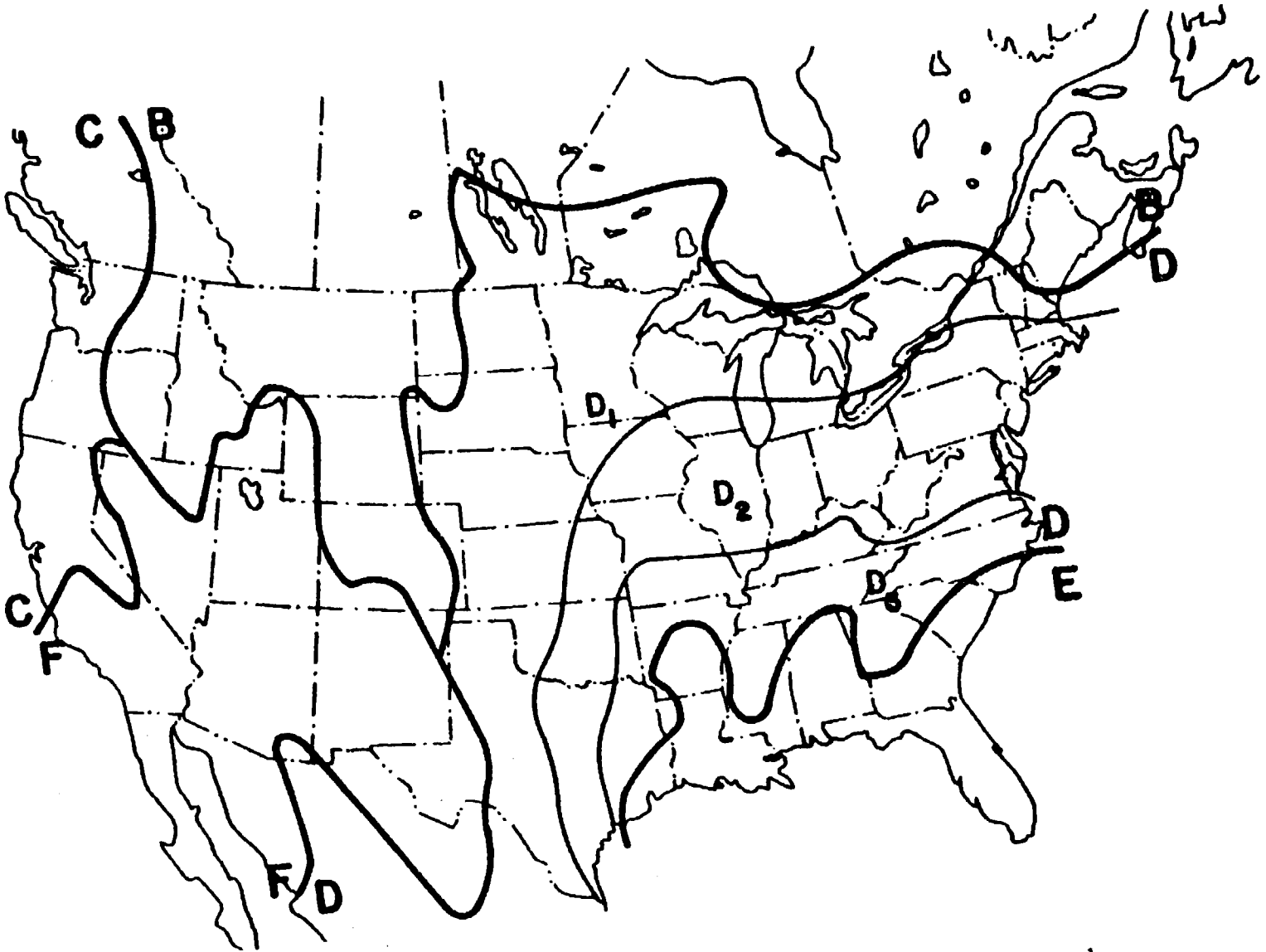

Figure 10 Rain rate climate regions for the Continental United States showing the subdivision of Region D

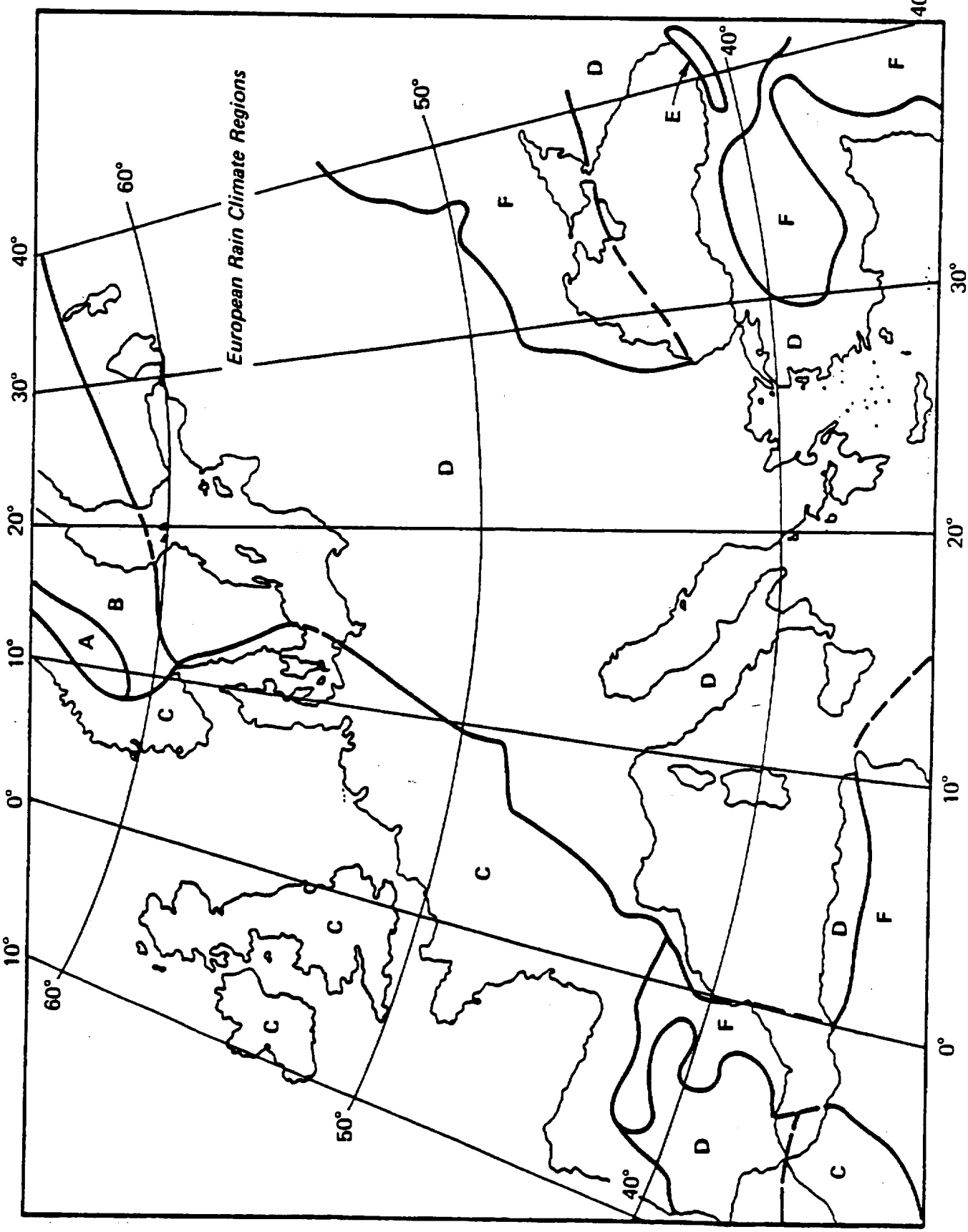

Figure 11 Rain rate climate regions for Europe

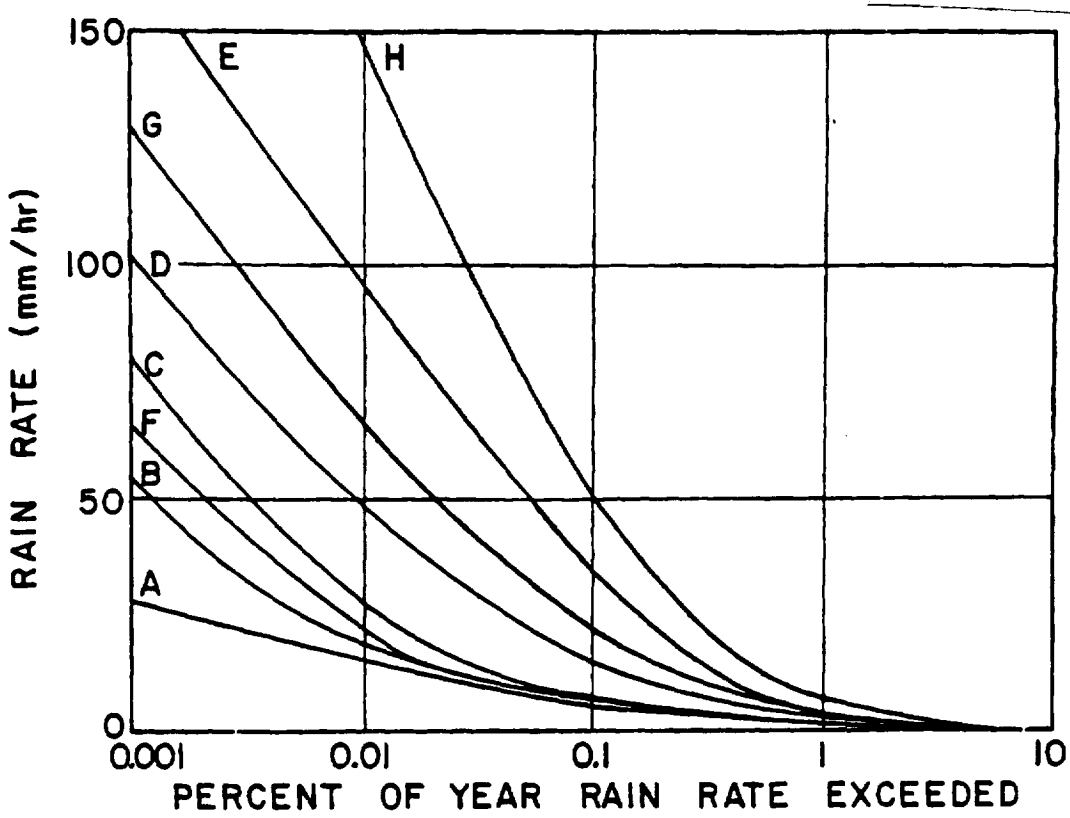

(a) Climate Regions A to H

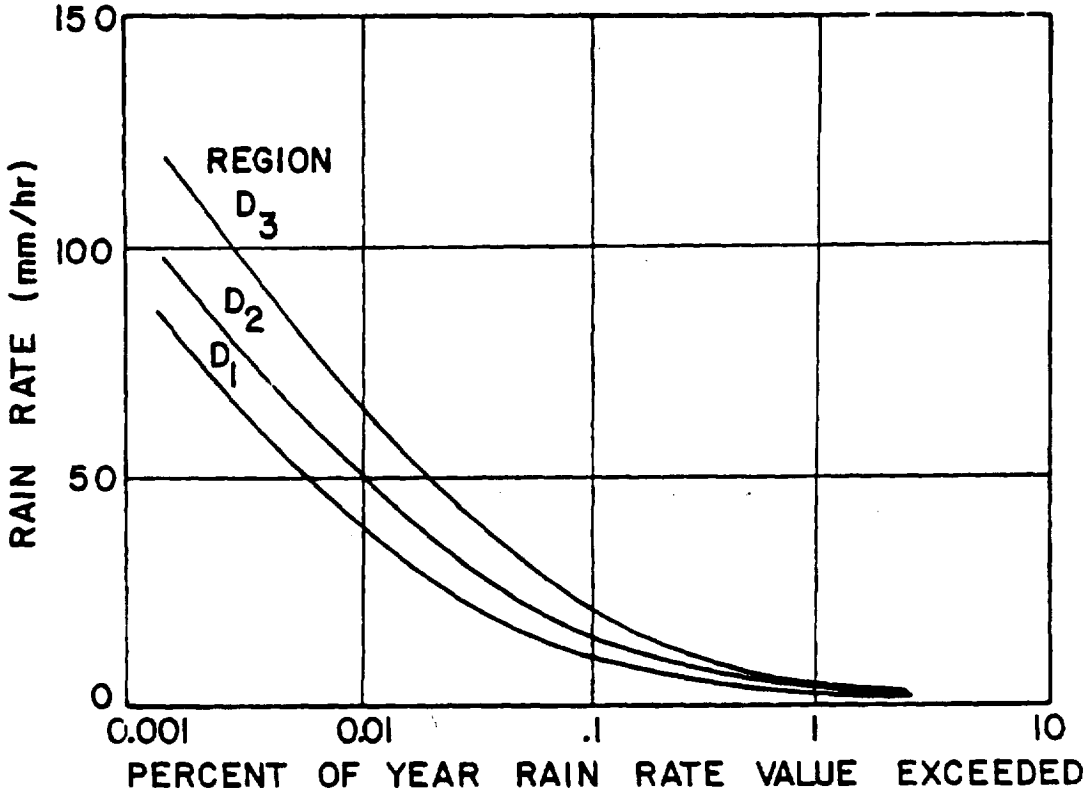

(b) Climate Regions D divided into three subregions (D_2 = D above)

Figure 12 Point rain rate distributions as a function of percent of year exceeded

TABLE 2

POINT RAIN RATE (R_p) DISTRIBUTION VALUES (mm/hr)

VERSUS PERCENT OF YEAR RAIN RATE IS EXCEEDED

Percent of Year	Rain Climate Region:									
	A	B	C	D_1	D_2	D_3	E	F	G	H
0.001	28	54	80	90	102	127	164	66	129	251
0.002	24	40	62	72	86	107	144	51	109	220
0.005	19	26	41	50	64	81	117	34	85	178
0.01	15	19	28	37	49	63	98	23	67	147
0.02	12	14	18	27	35	48	77	14	51	115
0.05	8	9.5	11	16	22	31	52	8.0	33	77
0.1	6.5	6.8	7.2	11	15	22	35	5.5	22	51
0.2	4.0	4.8	4.8	7.5	9.5	14	21	3.2	14	31
0.5	2.5	2.7	2.8	4.0	5.2	7.0	8.5	1.2	7.0	13
1.0	1.7	1.8	1.9	2.2	3.0	4.0	4.0	0.8	3.7	6.4
2.0	1.1	1.2	1.2	1.3	1.8	2.5	2.0	0.4	1.6	2.8

drops exist in the atmosphere should not be expected for the higher rain rates because large liquid water droplets are carried aloft above the 0°C height in the strong updraft cores of intense rain cells. It is necessary to estimate the rain layer height appropriate to the path in question before proceeding to the total attenuation computation since even the 0°C isotherm height depends on latitude and general rain conditions.

As a model for the prediction of attenuation, the average height of the 0°C isotherm for days with rain was taken to correspond to the height to be expected one percent of the year. The highest height observed with rain was taken to correspond to the value to be expected 0.001 percent of the year, the average summer height of the -5°C isotherm. The latitude dependences of the heights to be expected for surface point rain rates exceeded one percent of the year and 0.001 percent of the year were obtained from the latitude dependences provided by Oort and Rasmussen. The resultant curves are presented in Figure 13. For the estimation of model uncertainty, the seasonal rms uncertainty in the 0°C isotherm height was 500 m or roughly 13 percent of the average estimated height. The value of 13 percent is used to estimate the expected uncertainties to be associated with Figure 13.

The correspondence between the 0°C isotherm height values and the excessive precipitation events showed a tendency toward a linear relationship between R_p and H_o where H_o is 0°C isotherm height for high values of R_p. Since, at high rain rates, the rain rate distribution function displays a nearly linear relationship between R_p and log P (P is probability of occurrence), the interpolation model used for the estimation of H_o for P between 0.001 and one percent is assumed to have the form, $H_o = a + b \log P$. This relationship was used to provide the intermediate values displayed in Figure 13.

The complete model for the estimation of attenuation on an earth-space path starts with the determination of the vertical distance between the height of the earth station and the 0°C isotherm height ($H_o - H_g$ where H_g is the ground station height) for the percentage of the year (or R_p) of interest. The path horizontal projection distance (D) can then be obtained by:

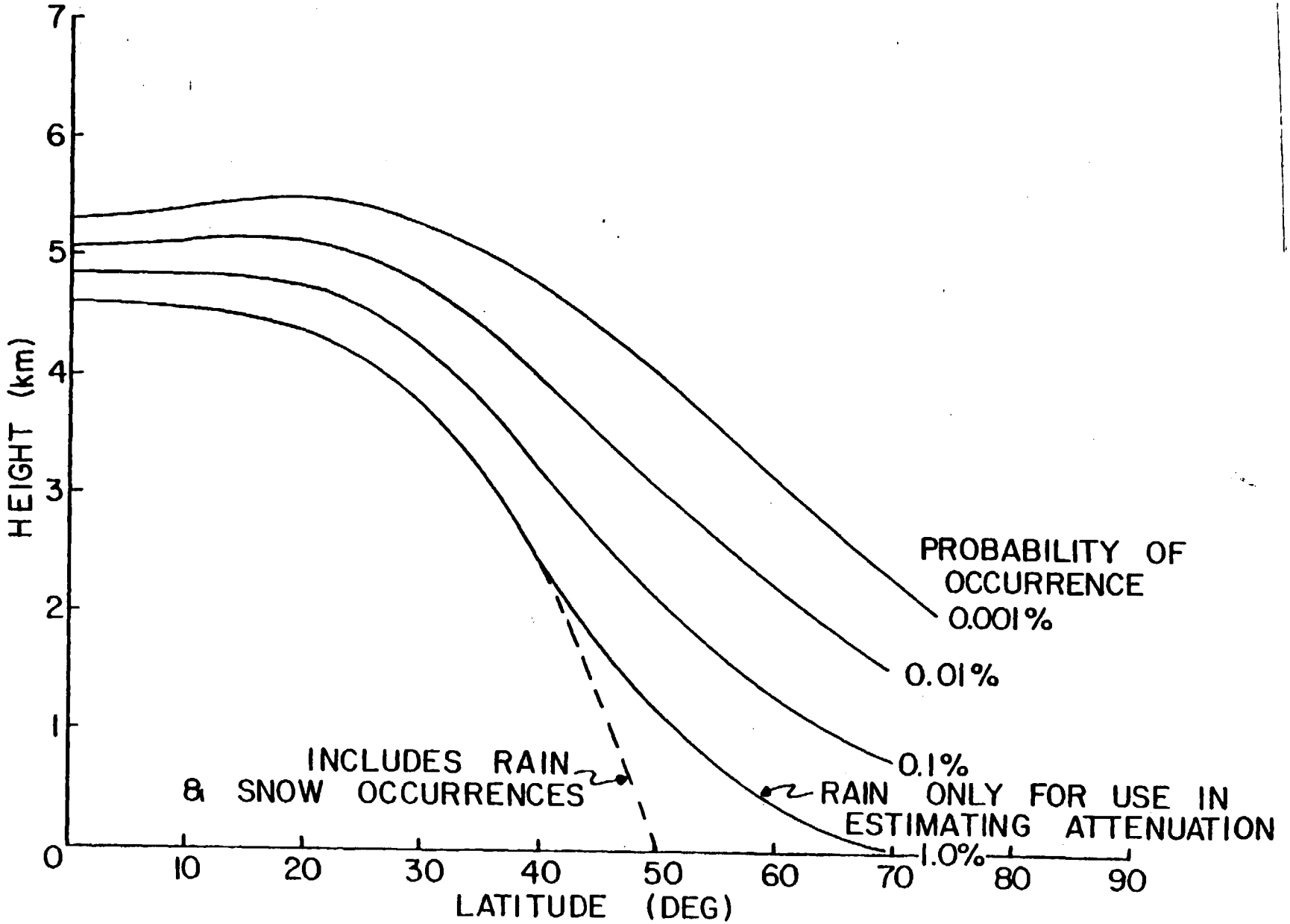

Figure 13 Latitude dependence of the rain layer 0°C isotherm height (H_o) as a function of probability of occurrence

$$D = (H_o - H_g)/\tan\Theta;\ \Theta \geq 10^\circ$$

$$= E\psi,\ \psi \text{ in radians};\ \Theta < 10^\circ \qquad (1)$$

where H_o = height of 0°C isotherm

H_g = height of ground terminal

Θ = path elevation angle

and

$$\psi = \sin^{-1}\left[\frac{\cos\Theta}{(H_o + E)}\left(\sqrt{(H_g + E)^2 \sin^2\Theta + 2E(H_o - H_g) + H_o^2 - H_g^2}\right.\right.$$

$$\left.\left. - (H_g + E)\sin\Theta\right)\right],$$

E = effective earth's radius (8500 km).

The specific attenuation may be calculated for an ensemble of rain drops if their size and shape number densities are known. Experience has shown that adequate results may be obtained if the Laws and Parsons (1943) number density model is used for the attenuation calculations (Crane, 1966) and a power law relationship fit to calculated values to express the dependence of specific attenuation on rain rate (Olsen et. al., 1978). The parameters α and β of the power law relationship:

$$a = \alpha R_p^{\beta} \qquad (2)$$

where a = specific attenuation (dB/km)

R_p = point rain rate (mm/hr)

are both a function of operating frequency. Figures 14 and 15 give the multiplier, $\alpha(F)$ and exponent $\beta(F)$, respectively, at frequencies from 1 to 100 GHz. The appropriate α and β parameters may also be obtained from Table 3 and used in computing the total attenuation from the model.

The total attenuation is obtained by integrating the specific attenuation along the path. The resulting equation to be used for the estimation of slant path attenuation is:

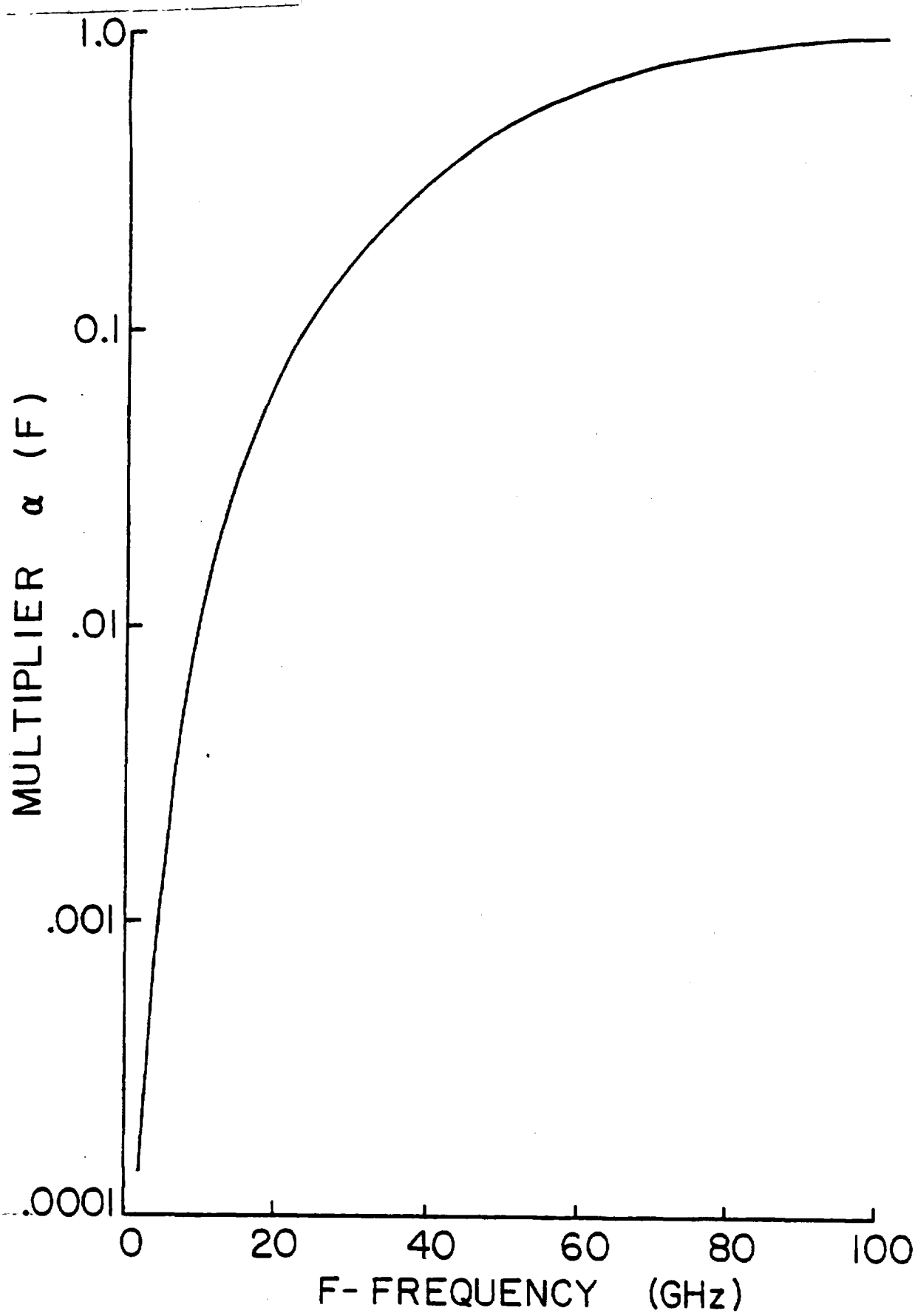

Figure 14 Multiplier (∝) in the power law relationship between specific attenuation and frequency

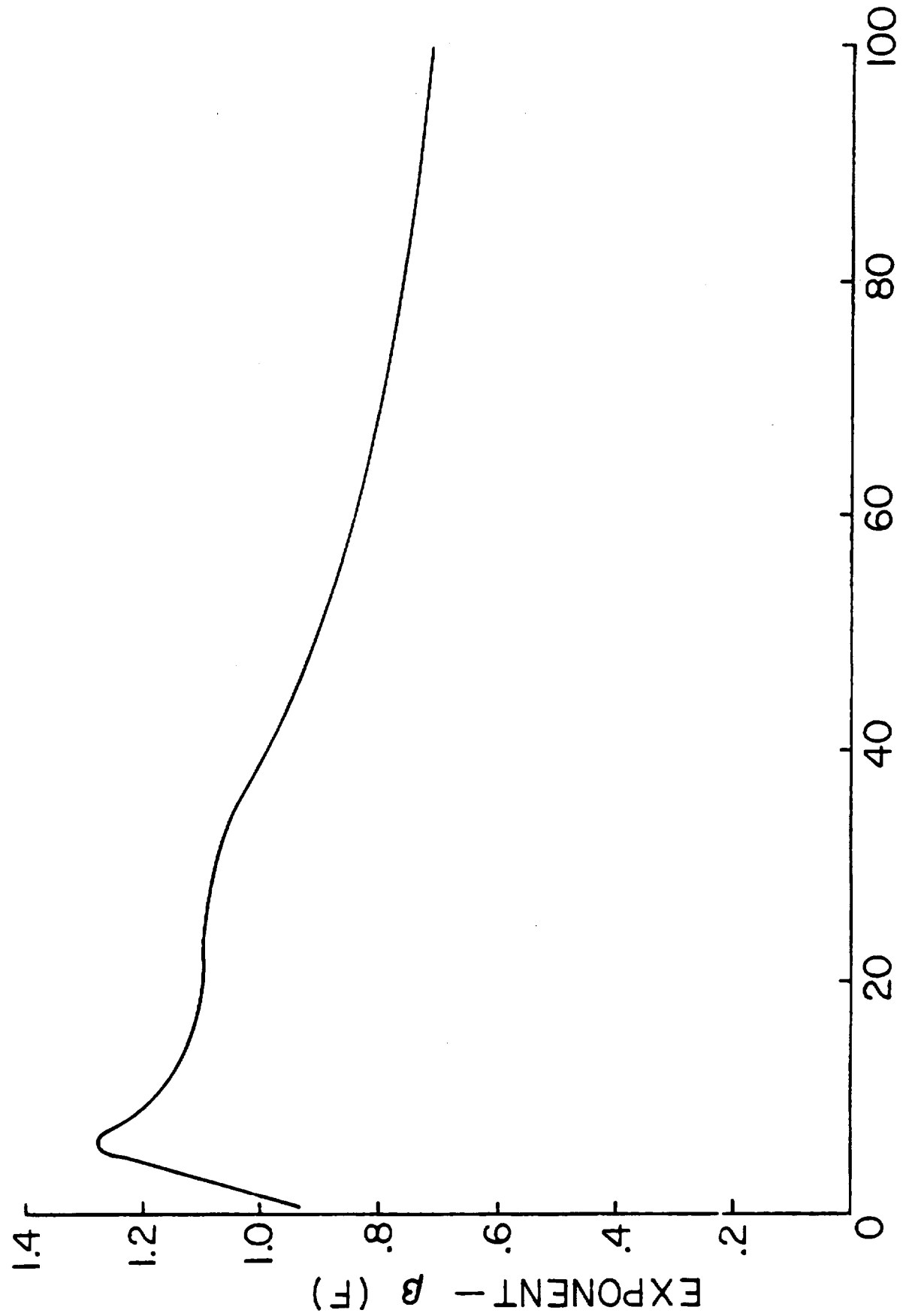

Figure 15 Exponent (β) in the power law relationship between specific attenuation and frequency

TABLE 3

PARAMETERS FOR COMPUTING SPECIFIC ATTENUATION:

$a = \alpha R_p^{\beta}$ (db/km), 0°C, Laws and Parsons*

Frequency F - GHz	Multiplier $\alpha(F)$	Exponent $\beta(F)$
1	0.00015	0.95
4	0.00080	1.17
5	0.00138	1.24
6	0.00250	1.28
7.5	0.00482	1.25
10	0.0125	1.18
12.5	0.0228	1.145
15	0.0357	1.12
17.5	0.0524	1.105
20	0.0699	1.10
25	0.113	1.09
30	0.170	1.075
35	0.242	1.04
40	0.325	0.99
50	0.485	0.90
60	0.650	0.84
70	0.780	0.79
80	0.875	0.753
90	0.935	0.730
100	0.965	0.715

*cf Crane (1966)

$$A = \frac{\alpha R_p^{\beta}}{\cos\Theta}\left[\frac{e^{u\beta d}-1}{u\beta} - \frac{b^{\beta}e^{c\beta d}}{c\beta} + \frac{b^{\beta}e^{c\beta D}}{c\beta}\right]; \quad \Theta \geq 10^{\circ} \qquad (3)$$

where u, b, c and d are empirical constants, defined in the next section, that depend on the point rain rate.

For lower elevation angles, $\Theta < 10^{\circ}$,

$$A = \frac{L}{D} \cdot \alpha R_p^{\beta}\left[\frac{e^{u\beta d}-1}{u\beta} - \frac{b^{\beta}e^{c\beta d}}{c\beta} + \frac{b^{\beta}e^{c\beta D}}{c\beta}\right]$$

where $L = \sqrt{(E + H_g)^2 + (E + H_o)^2 - 2(E + H_g)(E + H_o)\cos\psi}$

ψ = path central angle defined above.

2.2.2 Procedure

The following steps apply the rain attenuation model to a general earth-to-space path:

Step 1 - At the earth terminal's geographic latitude and longitude, obtain the appropriate climate region: A to H (1 of 8 regions), using either Figure 8 (land areas), 9 (includes ocean areas), 10 (United States) or 11 (Europe). If long term rain rate statistics are available for the location of the ground terminal, they should be used instead of the model distribution functions.

Step 2 - Select probabilities of occurrence (P) covering range of interest; percent of time rain rate exceeded (e.g., .01, .1 or 1%).

Step 3 - Obtain the terminal point rain rate R_p (mm/hr) using Figures 12a or 12b curves, or Table 2, or long term measured values if available of rain rate vs the percent of year rain rate is exceeded at the climate region and probabilities of occurrence (Step 2).

Step 4 - For an earth-to-space link through the entire atmosphere, obtain the rain layer height from the height of the 0°C isotherm (melting layer) H_o at the path latitude (Figure 13). The heights will vary correspondingly with the probabilities of occurrence (Step 2). To interpolate, plot $H_o(P)$ vs Log P and use a straight line to relate H_o to P.

Step 5 - Obtain the horizontal path projection D of the oblique path through the rain volume (equation 1):

$$D = \frac{H - H_g}{\tan\theta} \quad ; \theta \geq 10°$$

H = height of elevated terminal* (km); $H < H_o$

H_g = height of ground terminal (km)

θ = path elevation angle

*Note: $H = H_o$ for earth-to-space links (from Step 4) and H_o will vary with the probability of occurrence, $H_o = H_o(P)$.

Step 6 - Test $D \leq 22.5$ km; if true, proceed to the next step. If $D > 22.5$ km, the path is assumed to have the same attenuation value as for a 22.5 km path but the probability of occurrence is adjusted by the ratio of 22.5 km to the path length:

$$\text{new probability of occurrence, } P' = P\left(\frac{22.5 \text{ km}}{D}\right)$$

where D = path length projected on surface (>22.5 km)

Step 7 - Obtain the parameters $\alpha(F)$ and $\beta(F)$, relating the specific attenuation to rain rate, from Table 3 or Figures 14 and 15, or equivalent observed data where:

F = operating frequency (GHz)

Step 8 - Compute the total attenuation due to rain using R_p, α, β, θ, D (equation 3):

$$A = \frac{\alpha R_p^{\beta}}{\cos\theta}\left[\frac{e^{u\beta d}-1}{u\beta} - \frac{b^{\beta}e^{c\beta d}}{c\beta} + \frac{b^{\beta}e^{c\beta D}}{c\beta}\right] \quad ; \theta \geq 10°$$

where A = total path attenuation due to rain (dB)

α, β = parameters relating the specific attenuation to rain rate (from Step 7), $a = \alpha R_p^{\beta}$ = specific attenuation

R_p = point rain rate (Step 3)

θ = elevation angle of path

D = horizontal path distance (from Step 5)
$d \leq D \leq 22.5$ km

u, b, c, d are empirical constants:

$$u = \frac{\ln[be^{cd}]}{d}$$

$$b = 2.3\, R_p^{-0.17}$$

$$c = 0.026 - 0.03 \ln R_p$$

$$d = 3.8 - 0.6 \ln R_p$$

or alternatively: (if $D < d$),

$$A = \frac{\alpha R_p^{\beta}}{\cos\theta}\left[\frac{e^{u\beta D}-1}{u\beta}\right]$$

or if $D = 0$, $\theta = 90°$,

$$A = (H - H_g)[\alpha R_p^{\beta}]$$

2.2.3 Comparison with Experiment

Recent observations using the CTS, COMSTAR and ATS-6 satellite beacons allow the evaluation of the model at a number of frequencies and locations in regions D2 and D3 of the United States. An example of observations at CTS at 11.7 GHz (Ippolito, 1979) together with model predictions is given in Figure 16. The observations match (within 1 dB) the region D2 model between .015 and .024 percent of the year, match the tailored distribution between .012 and .02 percent of the year, and match the measured rain rate distribution over the .005 and .02 percent range. Since, on average, the two-year distribution is expected to be within 27 percent of the model distribution at 0.01 percent of the year and 33 percent of the model at 0.001 percent of the year, the data are replotted in Figure 17 on a percentage basis to better assess the agreement between measurement and model. In this figure, agreement is evident at percentages of the year smaller than 0.04; the region D2 model is within the expected uncertainty range, the tailored-rain rate model provides better agreement with measurement, and the measured rain rate data provide the best attenuation estimate. The measurements show significant disagreement in the .04 to 1 percent range. Since the attenuation values expected in this range are less than 6 dB, the calibration uncertainty (.5 dB) and the data quantization used to generate the distribution (2 dB) may affect the comparison.

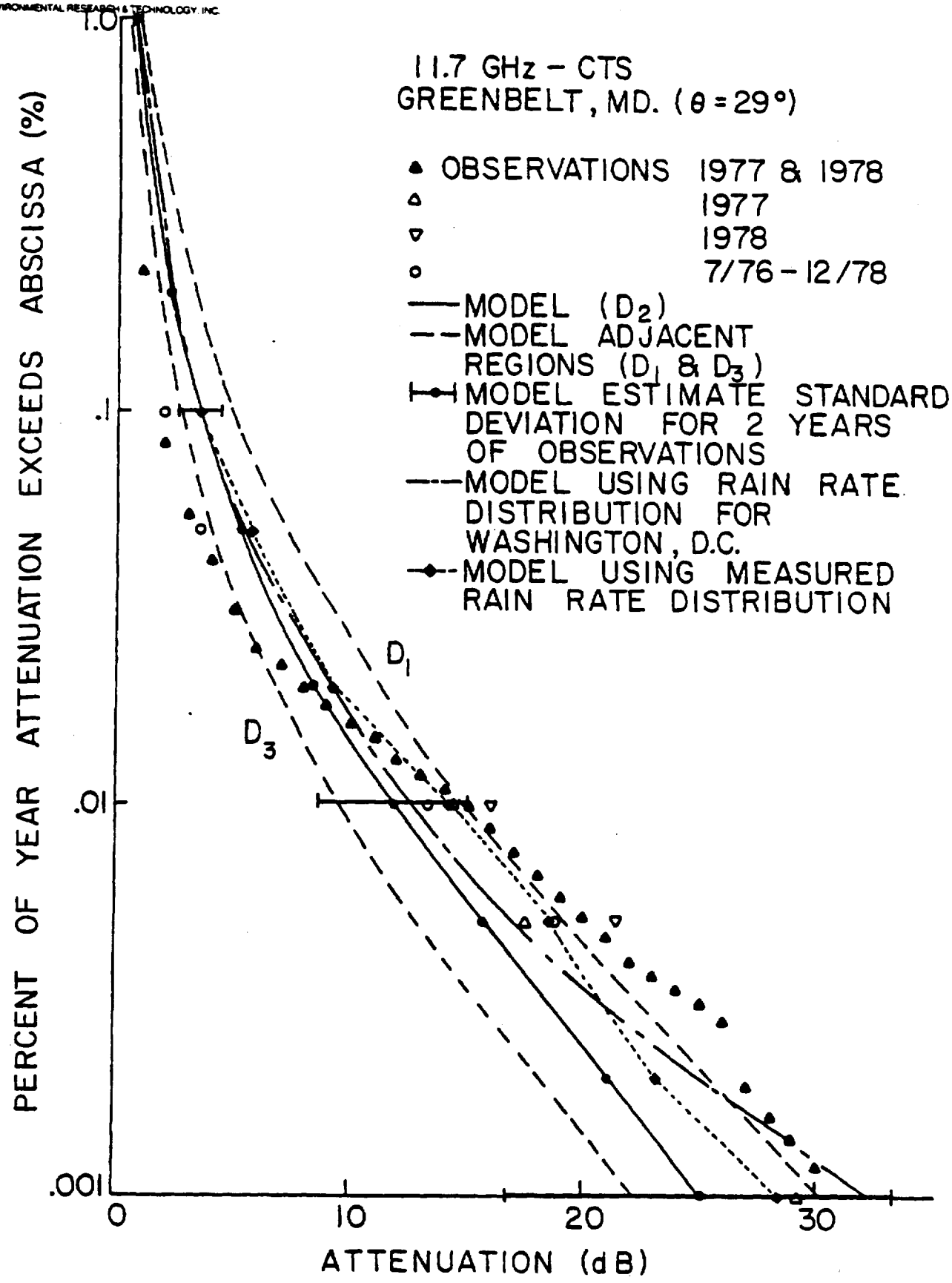

Figure 16 Comparison of CTS attenuation observations at 11.7 GHz (after Ippolito) with model estimates

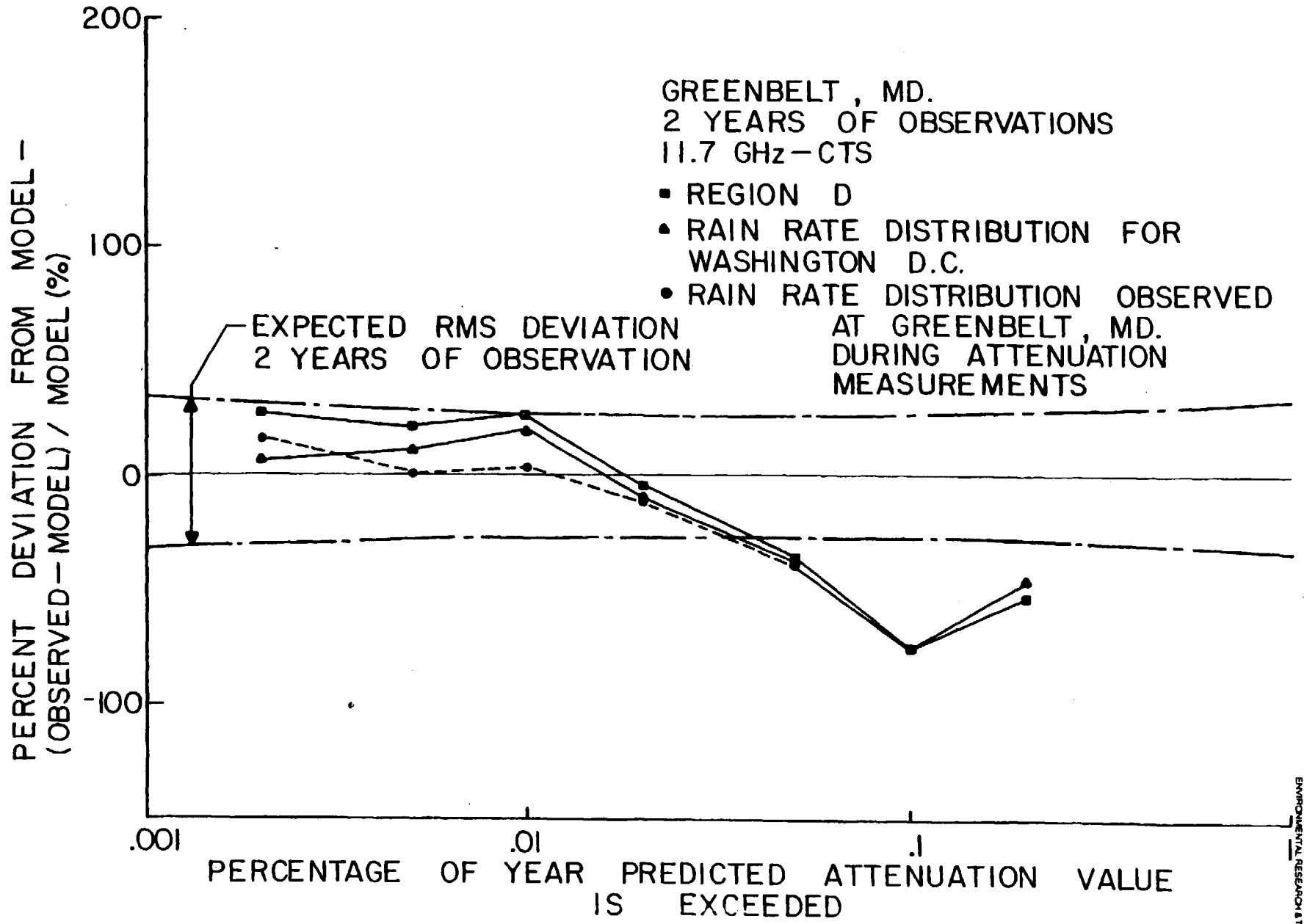

Figure 17 Comparison of observations (Figure 16) as percent deviation from the model estimate

Comparisons between a larger sample of observations and model calculations are presented in Figure 18. The data presented in this figure include the comparison already presented in Figure 17, 11.7 GHz CTS observations from Waltham, MA (Nackoney, 1978), Holmdel, N.J. (Rustako, 1979), Blacksburg, VA (Stutzman and Bostian, 1979), and Austin, TX (Vogel, 1979); 19.04 GHz and 28.56 GHz - COMSTAR observations from Holmdel, NJ (Arnold et al, 1979), Clarksburg, MD (Harris and Hyde, 1977), Wallops Island, VA (Goldhirsh, 1979) and Blacksburg, VA (Stutsman and Bostian, 1979); and 20 and 30 GHz-ATS-6 (Ippolito, 1976). These data show good agreement between measurement and model for percentages of the year less than 0.1; on average the observations deviate from their model predictions by less than eight percent. The rms deviation of all the measurements about the models is 25.7 percent, in agreement with the 29 percent rms expected uncertainty (at 0.1 and .01 percent of the year).

If all the data are used, the rms deviation increases to 48 percent. The data for the entire range are strongly affected by the large uncertainties associated with the Blacksburg measurements at percentages greater than 0.1 percent. Since the Blacksburg and Rosman measurements are for relatively high stations (0.7 km at Blacksburg, 0.88 km at Rosman) in close geographic location (although differing rain climate subregions), the good agreement at Rosman and the other stations and poor agreement at Blacksburg at percentages greater than 0.1 percent may indicate instrumental difficulties in this percentage range. A review of the calibration procedures used at Blacksburg indicates that the probable cause of uncertainty is the use of monthly calibration constants to process all the data acquired within the month; the daily variation in calibration could produce the relatively high attenuations in the 0.1 to one percent range. It is noted that excepting the data from Blacksburg, the comparison between observation and measurement is excellent, with less than a 25 percent rms difference over the entire percentage range for frequencies of 19 GHz and above and less than 26 percent rms for all frequencies. The agreement between observations and climate region model predictions are within the 29 percent rms deviation value expected for a one-year set of observations.

The slant path attenuation model provides attenuation estimates at all possible elevation angles. The sun tracker observations made in

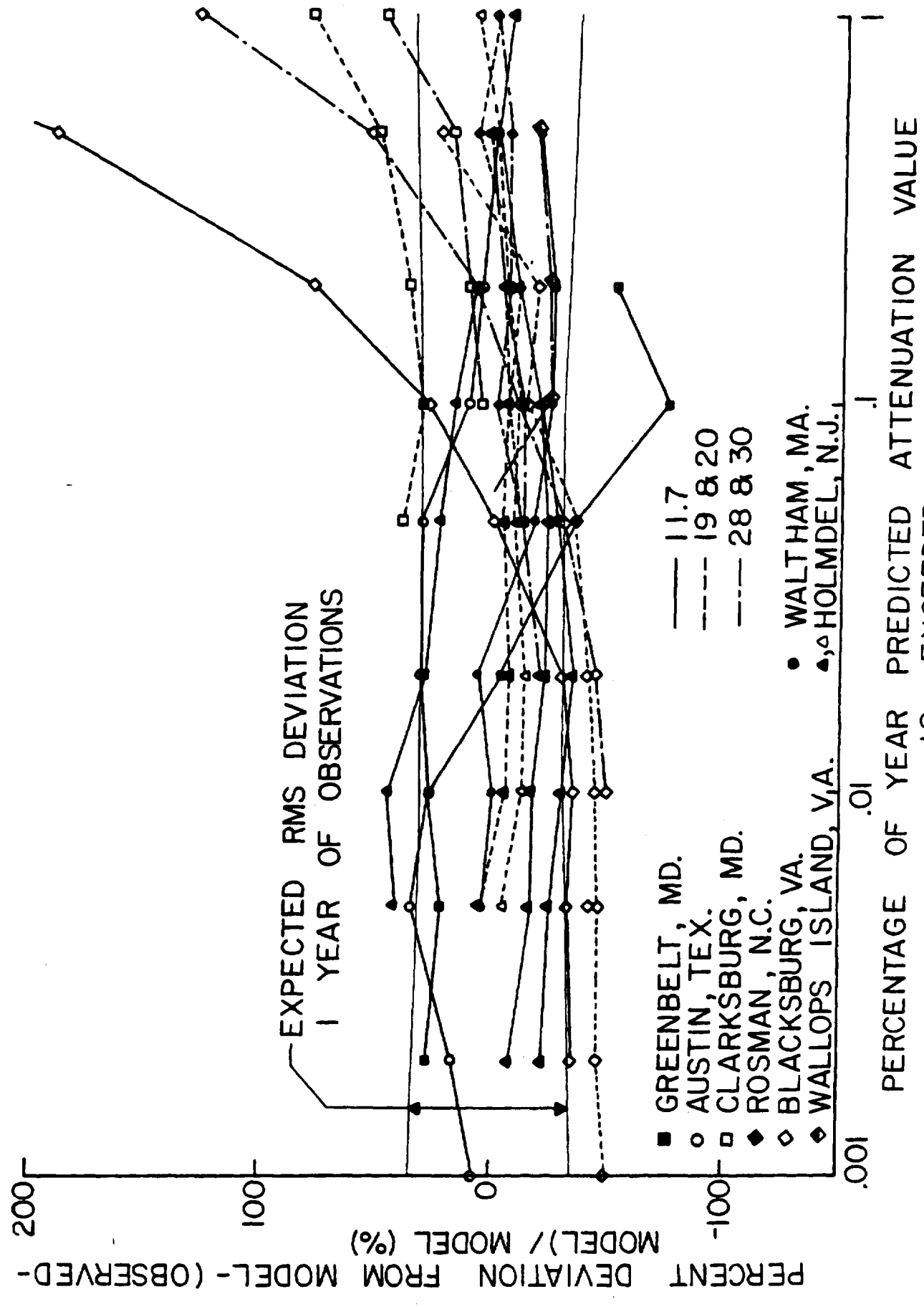

Figure 18 Comparison of observations as percent deviation from the model estimate for seven locations and three frequencies

the early seventies provide data for comparison with elevation angle dependence estimates. Kinase and Kinpara (1973) provided data on the elevation angle variation of 11.7 GHz attenuation observations for Klang, Malaysia (climate Region H). The model calculations for 10 and 20 mm/h (0.66 and 0.33 percent of the year respectively) are presented as a function of elevation angle in Figure 19 together with the observations for the same probabilities of occurrence. The model results and measurements show definite departures from a simple cosecant of the elevation angle dependence at both high and low elevation angles. The model agrees with observation at the rms deviation expected for observations which vary in elevation angle in synchronism with the sun (53% rms). The data for all elevations and both probabilities of occurrence have a 48 percent rms deviation about the model predictions; at elevation angles above 10°, the rms deviation is less than 36%.

These data show excellent agreement between the prediction model and observations on slant paths through the atmosphere.

A set of comparisons for a 20-km point-to-point path between modeled and measured attenuation values (Valentin, 1977) are presented in Figure 20. Good agreement between the model estimates and measurements are evident at all but the highest frequency. In these observations, the 39 GHz measurements clearly have some problems in that the attenuation at 29 GHz exceeds that at 39 GHZ for percentages of time larger than 0.3%. Also, difficulty is evident at the lower frequencies at larger percentages of the time when the attenuation at 15 GHz exceeds the value at 29 GHz. For measurements in the 20 to 40 dB range, agreement between the measurements and model estimates is excellent except at 30 GHz. For these observations, the dynamic range was not sufficient to make observations at 0.001 percent of the year at 19 GHz and higher frequencies on a 20-km path.

2.3 Scintillation

The propagation effects classified as scintillation-producing are attributable to two regions of the atmosphere. Though generally considered secondary to the effects due to molecular absorption and rain attenuation, the fluctuation losses may, under certain circumstances, impact significantly on earth-to-space communication paths. The effects

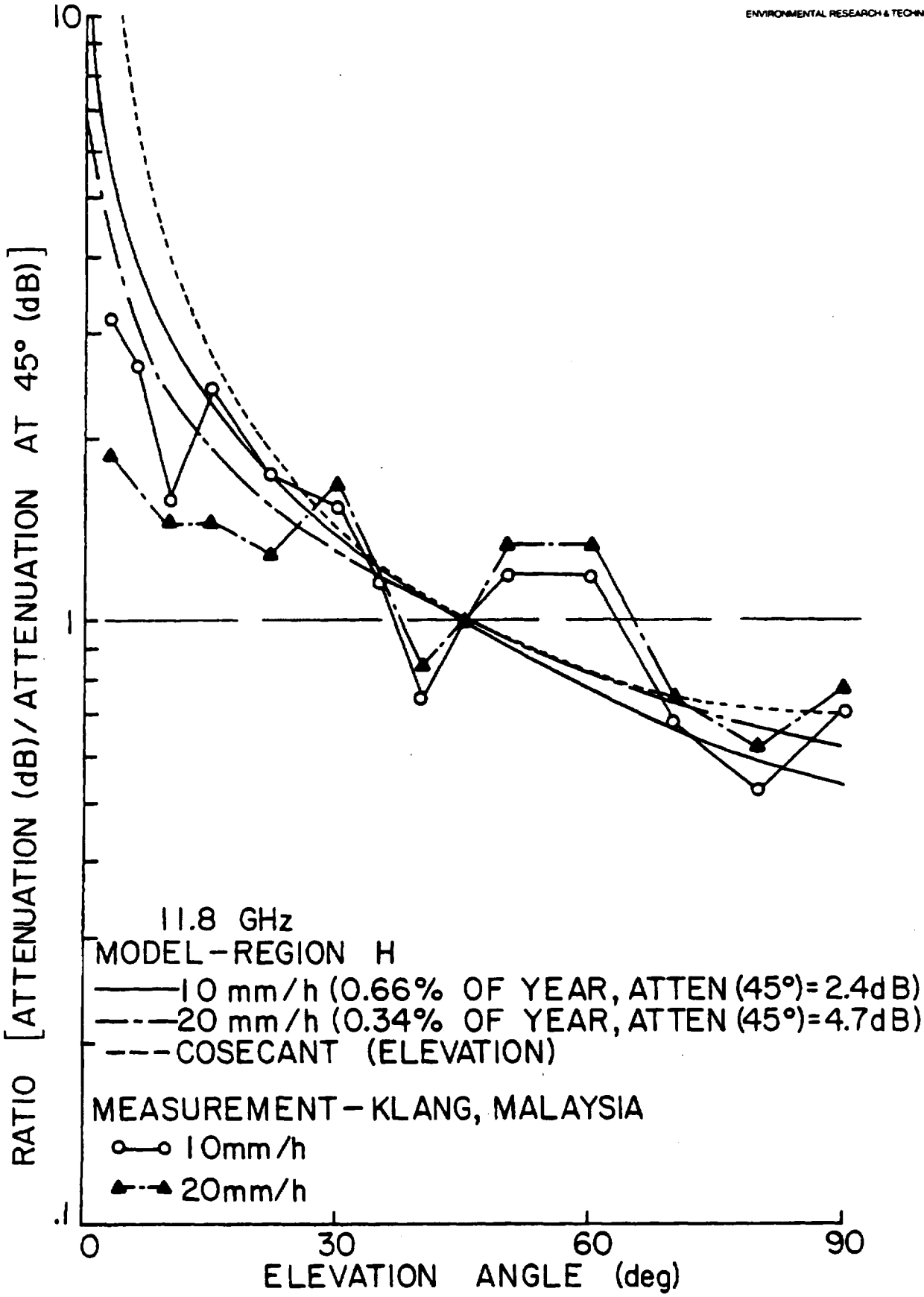

Figure 19 Elevation angle dependence of 11.8 GHz suntracker observations at Klang, Malaysia (Climate Region H; after Kinase and Kinpara) compared with model estimate

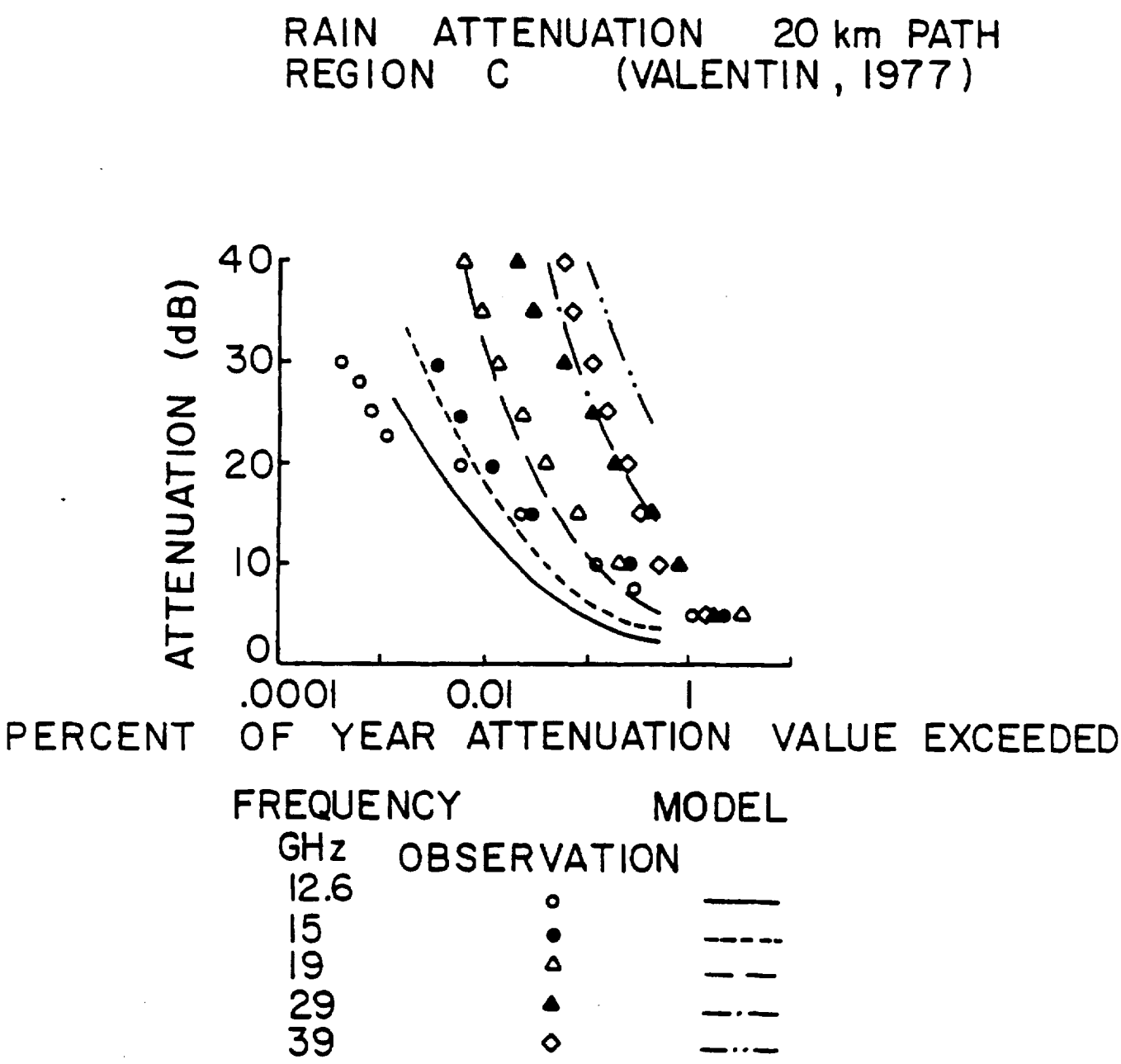

Figure 20 Comparison of point-to-point observations at five frequencies on a 20-km path with model estimates

produced by both the troposphere and ionosphere, sometimes termed signal fluctuation (or fast fading), are caused by inhomogeneity in the index of refraction along the propagation path; under extreme conditions, this inhomogeneity may result in internal atmospheric multipaths. The tropospheric effects are produced in the lowest altitude region (first few kilometers) of the path by local features such as high humidity gradients and temperature inversion layers leading to small height intervals in which the refractive index profile departs markedly from the expected general exponential decrease with altitude. To a first approximation, the refractive index structure is horizontally stratified and the regions of departure appear as thin horizontal layers. Superimposed on these layers, the refractive index at a particular height will change slightly in an oscillatory manner due to internal waves and in a random manner due to turbulence. The internal multipath effects producing fast fading are experienced when rays propagate over a considerable distance at highly oblique angles through the near-horizontally-oriented smaller scale inhomogeneities. Though this usually affects line-of-sight propagation more at low elevation angles (below 5° elevation at frequencies below X-band), the amplitude fluctuations depend on wavelength and may significantly affect higher frequencies (above 10 GHz) at increasingly higher elevations. The effects are seasonally dependent and are variable from day-to-day as well as geographically.

2.3.1 Ionospheric Scintillation

Ionospheric induced scintillation, also produced by inhomogeneity in the ionospheric refractive index due to electron density irregularities, is mostly produced near the height of the maximum electron density (F-region) of the ionosphere. Again, this may be experienced at low elevations where much of the ionosphere is traversed or at any elevation when disturbed ionospheric conditions (such as those classed as "spread-F") are experienced. There are particular geographic regions where such conditions prevail (e.g., equatorial regions or high latitudes where the propagation paths intersect the auroral zones) and become significant in path selection and/or design. The ionospheric scintillation effects are predominately a "lower frequency" effect due to the λ^2 frequency dependence of the refractive index in ionized regions and are commonly exper-

ienced only below 4 GHz. The effects, related to electron density irregularities are variable diurnally, seasonally, and depend on the current sun spot number of the solar cycle. Additionally, solar-geophysical distrubances affecting the earth's geomagnetic field may influence the occurrences. For most systems operating above 10 GHz, the amplitude scintillation and absorption effects due to ionospheric contributions are secondary to other system error budgets and may be neglected. For more specific information on the character of signal effects related to ionospheric scintillation and the impact on transionospheric systems, several references may be consulted (Crane, 1977, 1978, 1976a), including a discussion in CCIR Report 263-3 (1976). In particular, for any propagation links or services planned at the equatorial or high latitude locations using lower frequencies, a study of the effects due to penetration of the ionosphere should definitely be made.

2.3.2 Tropospheric Scintillation

Tropospheric induced scintillation effects result in several propagation characteristics which may be of significance at the higher frequencies. The three effects of significance to the higher frequencies at greater elevation angles are the angle-of-arrival and amplitude fluctuations produced by inhomogeneity in the clear-air refractive index, and the antenna aperture (signal gain) degradation relatable to the finite scale sizes of the irregularities. The angle-of-arrival effects produce a slight angular variation of the received signal about the apparent angular position (also affected by average refractive bending) of the rays from the satellite source. The elevation angle variations are typically 10 times larger than the azimuthal variations. Data obtained from satellite observations made using a large aperture tracking antenna at Haystack Observatory, Westford, Mass. (at X-band), suggests that angle scintillation is not likely to be important for antenna beamwidths larger than 0.3° at all elevation angles or beamdwidths larger than 0.01° at all elevation angles higher than 10°. The elevation angle fluctuations are of the same order of magnitude as the expected uncertainty in refraction correction using surface refractivity values. Figure 21 (Crane, 1976b) indicates the range of extremes in the RMS fluctuations in elevation angle versus elevation on the 120 foot (36.6 m)

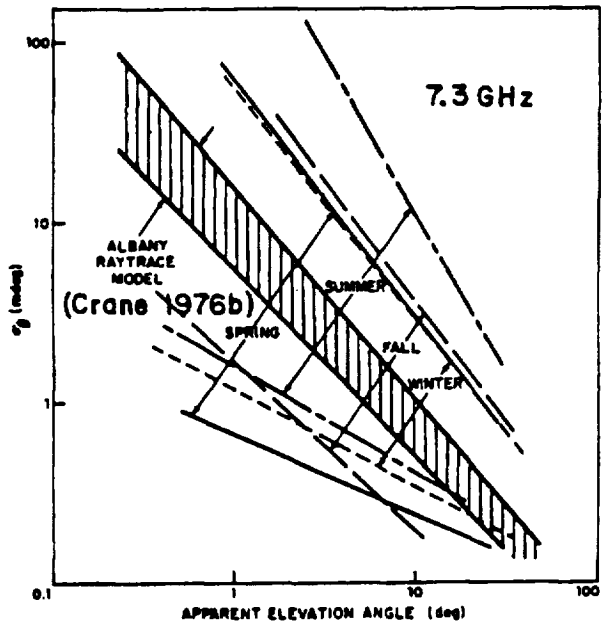

Figure 21 RMS fluctuations in elevation angle for a full year period

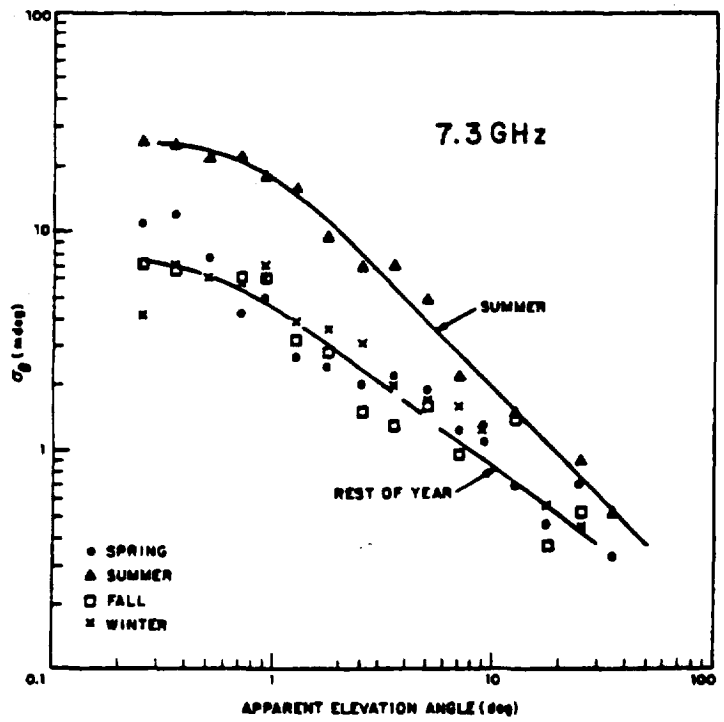

Figure 22 Median RMS fluctuations in elevation angle by season

antenna at 7.3 GHz. A seasonal dependence was identified, as shown, throughout a year of observations sampled at different times of day, seasons, and meteorological conditions. It is expected that these magnitudes of angle-of-arrival effects may be expected over a variety of operating conditions relatively independent of frequency. For reference also, the median RMS fluctuations by season are also shown in Figure 22. These data, ranging in initial elevation angles from the horizon to 43°, represent the minimum elevation angle measurement uncertainties (within a five-minute observation period) to be expected due to the troposphere. Single antenna radar or communication systems probably will not achieve better measurement accuracies or lower angular position uncertainties, respectively, than these for paths traversing the complete troposphere.

Amplitude fluctuations produced by the troposphere exhibit a frequency dependence predictable by theory. The observed data from the Haystack measurements show a range of variability at 7.3 GHz as indicated in Figure 23 through the seasons. The ordinate is RMS fluctuations in log received power σ_χ (dB) versus the apparent satellite elevation angle. Measurements at UHF (Millstone Hill Radar, near Haystack) as well as X-band, produced tropospheric scintillation observations which were in qualitative agreement with predictions of weak scintillation theory for elevation angles above 2 to 3°. The theory would predict a $(\text{frequency})^{7/12}$ dependency for the log power fluctuation intensity assuming an isotropic turbulent layer and weak scintillation, $\sigma_\chi < 5$ dB (Crane, 1977). When these assumptions are valid, the amplitude scintillation variance due to turbulent fluctuations reduce to an expression (as obtained by Tatarski, 1967) given by:

$$\sigma_\chi^2 = \left(\frac{20}{\ln 10}\right)^2 0.56\, k^{7/6} \cdot \int_0^L Cn^2(\rho) \cdot \rho^{5/6}\, d\rho \qquad (1)$$

where: σ_χ = log power RMS fluctuation (dB)

k = wave number = $2\pi/\lambda$, (λ = operating wavelength)

$Cn(\rho)$ = refractive index structure constant (variable along ray path)

ρ = distance along ray path

L = total length of ray path

Precise knowledge, therefore, of the amplitude fluctuation depends on a knowledge of the refractive index structure function along any given oblique path. Since this is usually unknown in detail, approximations would need to be made to model Cn^2 for a specific location. At 10 GHz, the signal may fluctuate at levels between 0.1 and about 1.0 dB depending upon elevation angle and conditions (see Figure 23) with the requirement that elevation angles are above about 3 degrees. At 100 GHz, the levels scale in frequency to lie correspondingly between 0.4 and 3.8 dB, depending on elevation angle and upon (low or high) fluctuation conditions if the refractive index structure is invariant over the frequency range.

The third tropospheric effect of significance, antenna aperture degradation, is dependent on the scale sizes of the refractive inhomogeneities relative to the antenna diameter. The effect, sometimes expressed as antenna gain-loss, occurs because the antenna aperture and the propagating medium are coupled. For a propagation path traversing the troposphere to a distant satellite, the Fresnel zone sizes may be defined as:

$$F = \sqrt{n\lambda z} \qquad (2)$$

where: n = order of Fresnel zone

z = the reduced path length

$= \frac{\rho(L-\rho)}{L}$

L = total length of ray path

ρ = position along ray path

λ = operating wavelength

When the scale size of refractive index irregularities L_o is small compared to the Fresnel zone size, the scattering can be described as isotropic and weak scattering theory as described holds. The scattering mechanism is usually classed as small scale turbulence. At higher microwave frequencies, L_o can become larger than the Fresnel zone causing anisotropic scattering and considerable spatial curvature of the incident wavefronts. For increasingly large antenna apertures, a size, D, is reached at which the antenna gain, predicated on a plane wavefront, is degraded.

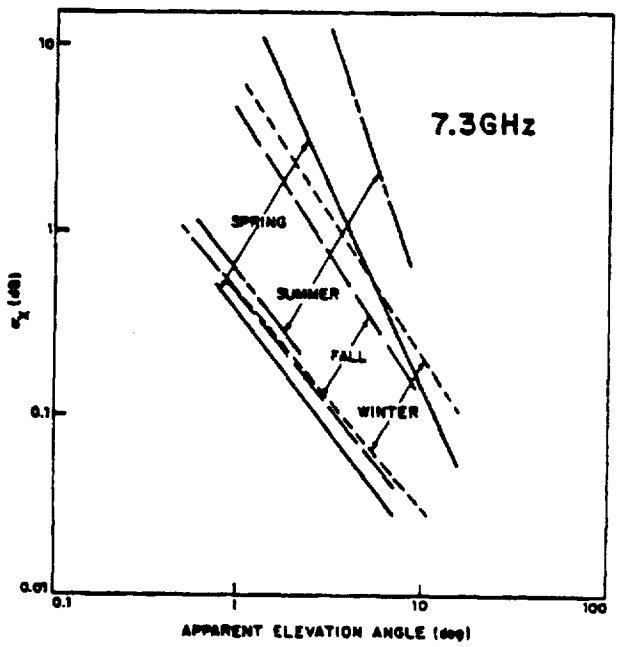

Figure 23 RMS fluctuations in log power (dB) for a full year period

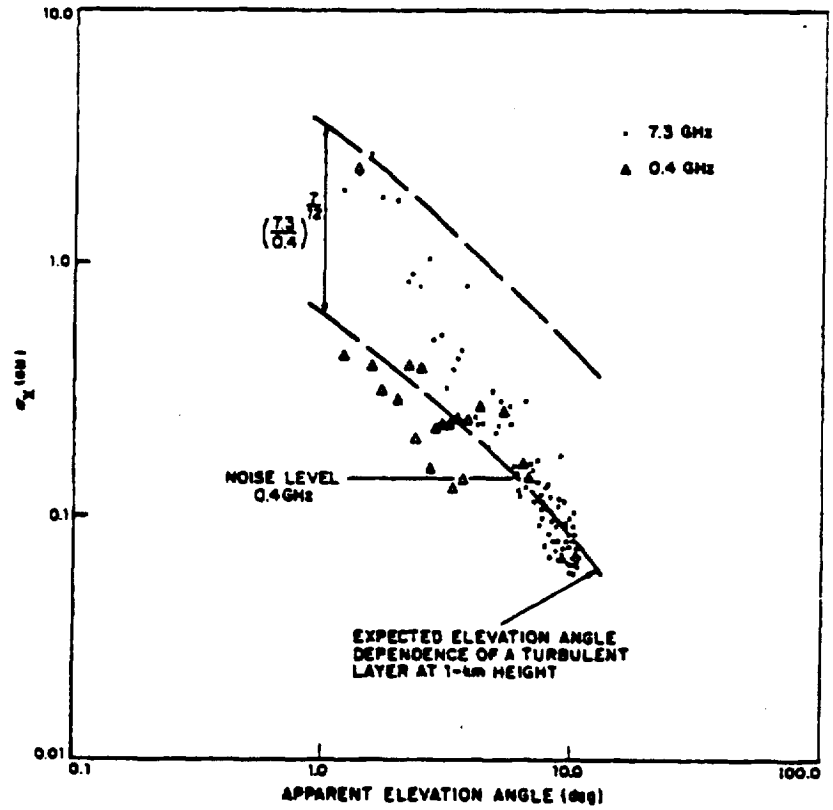

Figure 24 RMS fluctuations in log power at X-band and UHF, 29-30 April 1975

With further curvature, some of the fluctuations due to a corrugated wavefront are spatially averaged by the antenna. Further, as the elevation angle increases, the Fresnel zone size (given by Eq. 2) continues to decrease due to the rapidly decreasing distance ρ between the producing layer and the antenna. The result is therefore a reduction in the fluctuation depth due to antenna averaging and a reduction in the effective antenna gain (i.e. gain-loss). An example of this effect occurring, is shown in Figure 24 for the Haystack 36.6 m antenna. There was a fall-off in the 7.3 GHz RMS fluctuations from the level predicted (dashed line), as the elevation angle increased above two degrees, until the fluctuation level at 10 degrees reached that obtained at UHF. For the prediction, a turbulent layer height of 1 km was assumed. Tatarski (1967) showed that the RMS fluctuations are reduced by 20 percent when the diameter of a uniformly weighted circular aperture is one-half the first Fresnel zone size ($D = \sqrt{\lambda z}/2$).

The tropospheric scintillation model presented is based upon the Haystack measurements and the theory described. An assumed average height of 1 km was used to a thin turbulent layer. The rms fluctuation level used as a reference point for the model corresponds to the annual mean at one degree elevation obtained at Haystack Observatory. As a result of the theory and a cosecant Θ power law fit approximation for a 1 km high layer, the following fluctuation model dependencies were obtained for the model:

$$\sigma_\chi(F,\Theta,D) = \sigma_{\chi,REF}\left(\frac{F}{7.3}\right)^{7/12}\left(\frac{\csc\Theta}{\csc 1^\circ}\right)^{0.85}\left(\frac{G(R)}{G(R)_{REF}}\right)^{1/2} \text{(dB)} \quad (3)$$

where:

$\sigma_{\chi,REF}$ = reference rms fluctuation at 1°, 7.3 GHz, Haystack, D = 36.6 m (dB)

{$\sigma_{\chi,REF}$ = 1.883 dB is used in the model}

F = operating frequency (GHz)

Θ = apparent elevation angle

G(R) = antenna aperture averaging factor, Tartarski (1967)

$G(R)_{REF}$ = value for Haystack at 1°, D = 36.6 m

A piecewise linear approximation to Tartarski's antenna aperture averaging factor, G(R) was made as follows:

$$G(R) = 1.0 - 1.4\left(\frac{R}{\sqrt{\lambda L}}\right) \quad ; \quad 0 \leq \frac{R}{\sqrt{\lambda L}} \leq 0.5$$

$$= 0.5 - 0.4\left(\frac{R}{\sqrt{\lambda L}}\right) \quad ; \quad 0.5 < \frac{R}{\sqrt{\lambda L}} \leq 1.0 \qquad (4)$$

$$\cong 0.1 \quad ; \quad 1.0 < \frac{R}{\sqrt{\lambda L}}$$

where: R = effective radius of circular antenna aperture (m)

= $(\eta)^{1/2}\frac{D}{2}$, D = physical diameter of reflector and η = antenna efficiency factor {$\eta = 0.56$, $(\eta)^{1/2} = 0.75$ assumed in model}

L = slant distance to height of a horizontal thin turbulent layer

= $[h^2 + 2 r_e h + (r_e \sin\theta)^2]^{1/2} - r_e \sin\theta$

h = height of layer {h = 1000 m assumed in model}

r_e = effective earth radius including refraction {$r_e = 8.5 \times 10^6$ m in model}

λ = operating wavelength (m)

For computational purposes, equation (3) reduces to the following:

$$\sigma_\chi(F,\theta,D) = K \cdot F^{7/12} (\csc\theta)^{0.85} (G(R))^{1/2} \quad (dB) \qquad (5)$$

where: $K = 2.5 \times 10^{-2}$

The model has been tested successfully against several sources of experimental observations exercising the frequency, elevation angle and aperture dependencies. Figure 25 shows the model compared with the annual mean 7.3 GHz data beyond the reference point value. A very good fit is observed with elevation angle. For comparison, the data for a specific recording period from Figure 24 is included which departs from the mean but lies within the uncertainty bounds. The Millstone 0.4 GHz

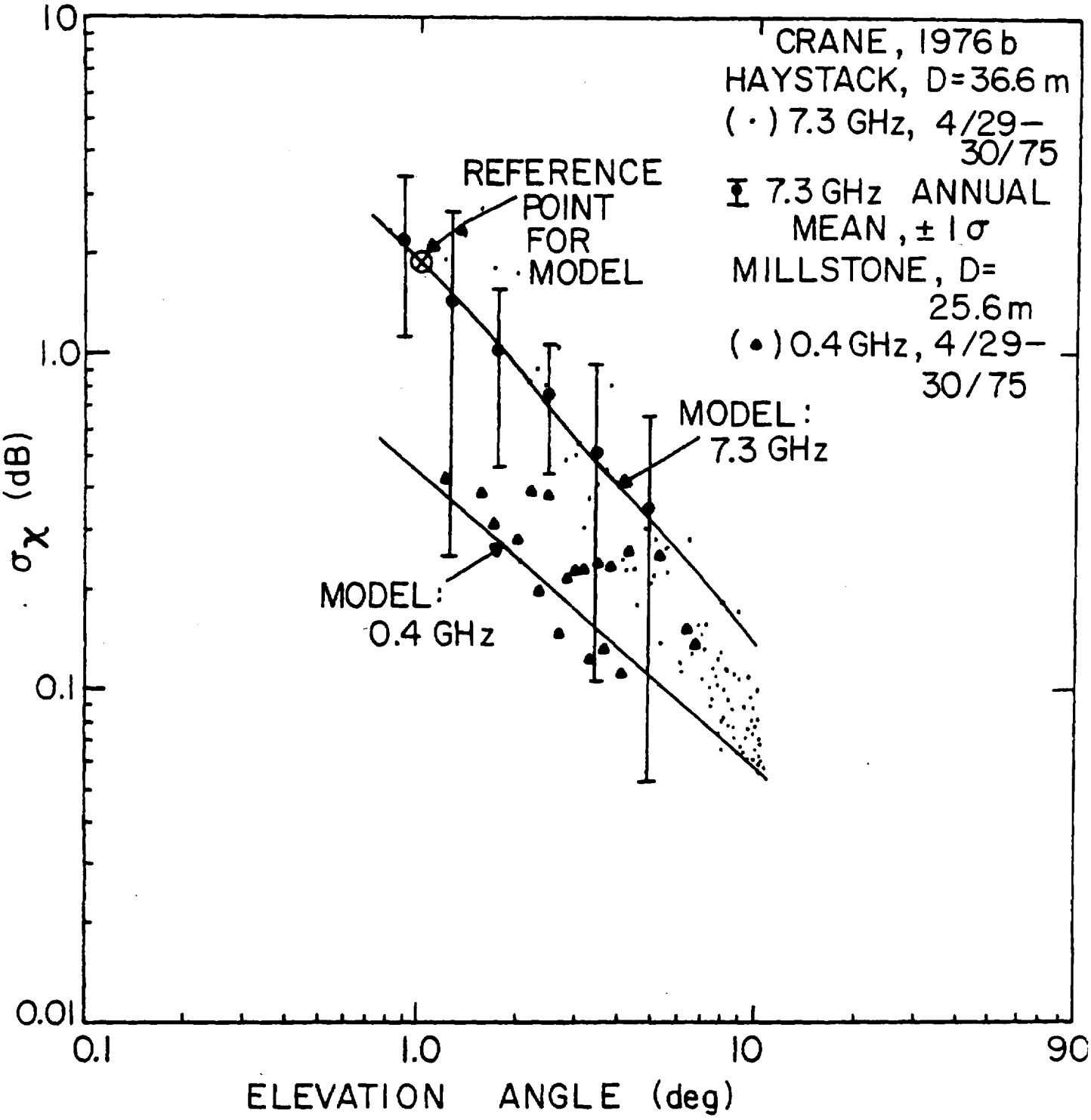

Figure 25 Comparison of tropospheric scintillation model with Haystack (7.3 GHz) and Millstone (0.4 GHz) observations

data for the same period is shown compared with the model curve at this frequency. The 4 and 6 GHz data obtained in Japan by Yokoi (1970) are compared with the model predictions in Figure 26 over the elevation angle range of 5 to 50 degrees. Again, a favorable match occurs between the observations and the model.

Finally, the ATS-6 measurements are compared with the model over the frequency range of 2 to 30 GHz. Figure 27 shows the Ohio State University measurements, Baxter and Hodge (1978), at 2 GHz (D = 9.1 m) and of Hodge, et al (1976) at 20 and 30 GHz (D = 4.6 m). In this figure, the data are shown in terms of amplitude variance (S^2) as opposed to rms log power. The conversion for small amplitudes is:

$$S^2 = 20 \log_{10} \left[\frac{\sigma_\chi}{8.68} \right] \quad \text{(dB)} \qquad (6)$$

The model curves agree well with the measurements expecially at 2 and 30 GHz over the elevation angle range from 1 to 45 degrees. The model, therefore, appears generally applicable over a wide range of the parameters to predict the rms fluctuation losses, on average, to be expected at any location. Figure 28 depicts a specific family of curves using equation (5) for a fixed antenna aperture diameter D, of ten meters.

2.3.3 Procedure

To estimate losses due to tropospheric scintillation L_{scint}(dB), the following steps may be used:

Step 1 - Obtain a value of $R/\sqrt{\lambda L}$ to test the region of aperture averaging in equation (4). The antenna diameter D, elevation angle θ and the operating wavelength, $\lambda = c/F$, are required input variables.

Step 2 - Compute the appropriate aperture averaging factor G(R) from equation (4), depending on the range of $R/\sqrt{\lambda L}$ from step 1.

Step 3 - Compute the tropospheric scintillation loss $L_{scint} = \sigma_\chi(F,\theta,D)$ using equation (5). Note that a correction for elevation angle-of-arrival fluctuations is not needed if the antenna beamwidth is larger than that indicated by the maximum values in Figures 21 or 22.

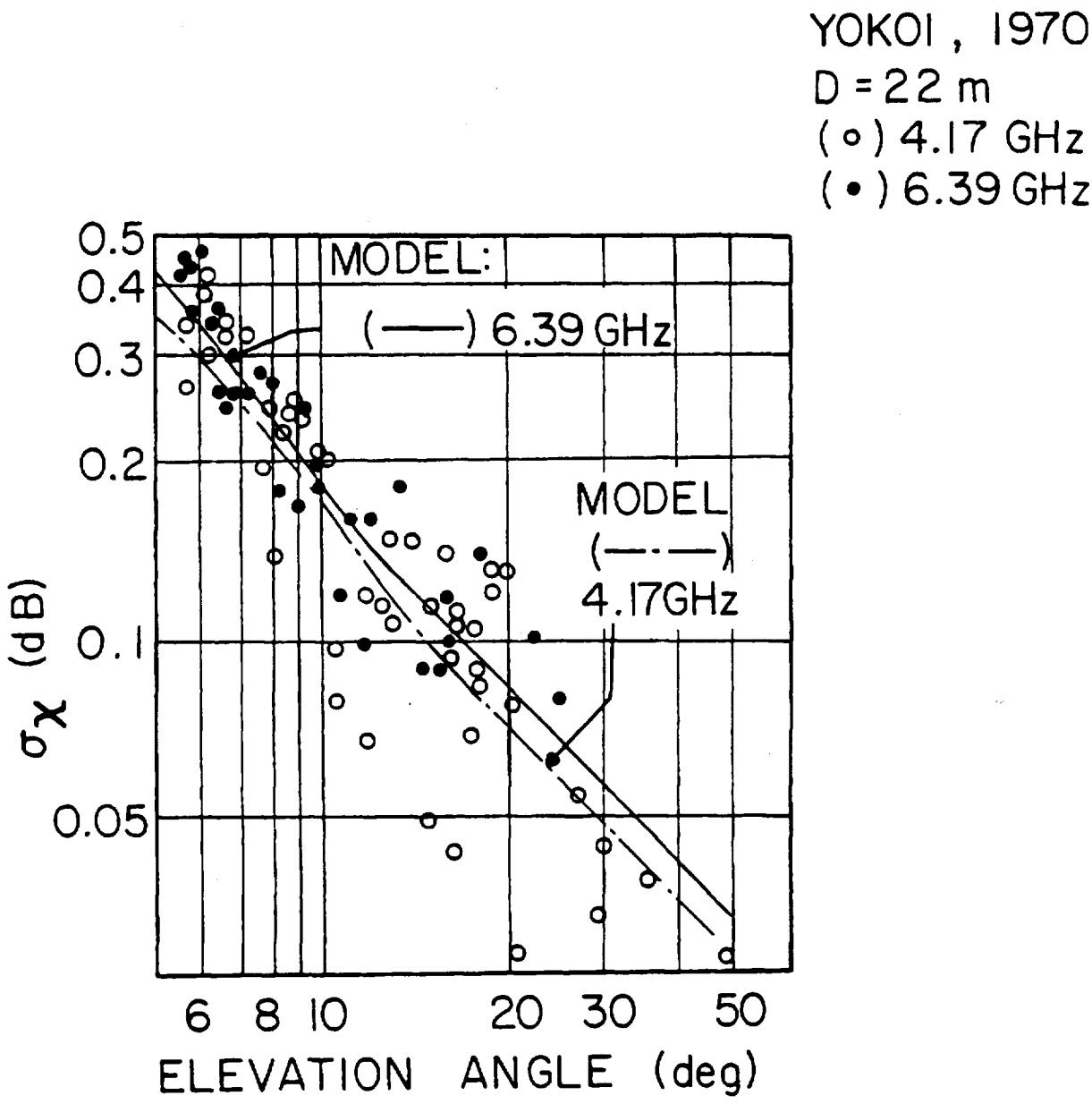

Figure 26 Comparison of model predictions with observations at 4 and 6 GHz (after Yokoi)

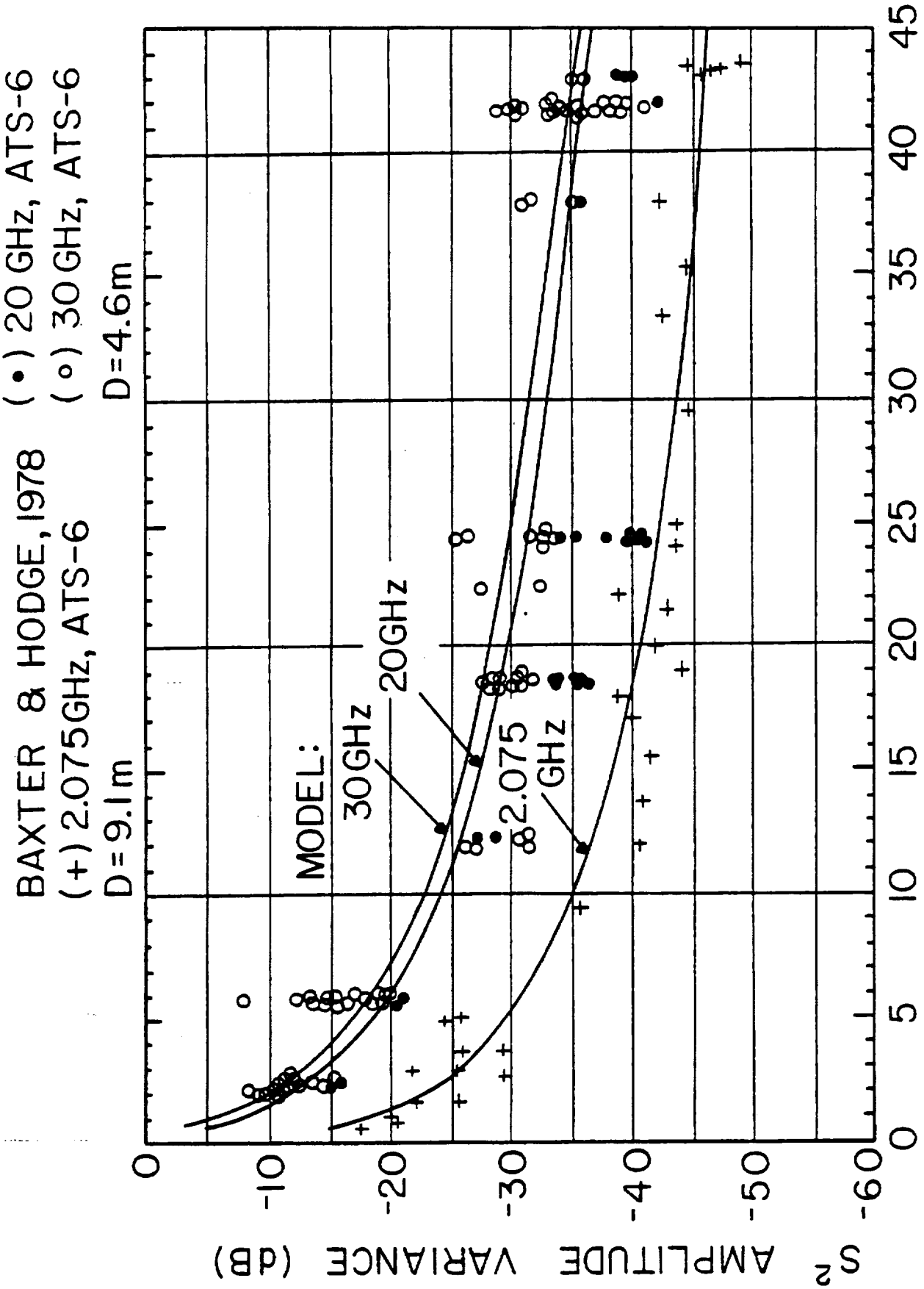

Figure 27 Comparison of model predictions (amplitude variance) with ATS-6 observations at 2, 20 and 30 GHz

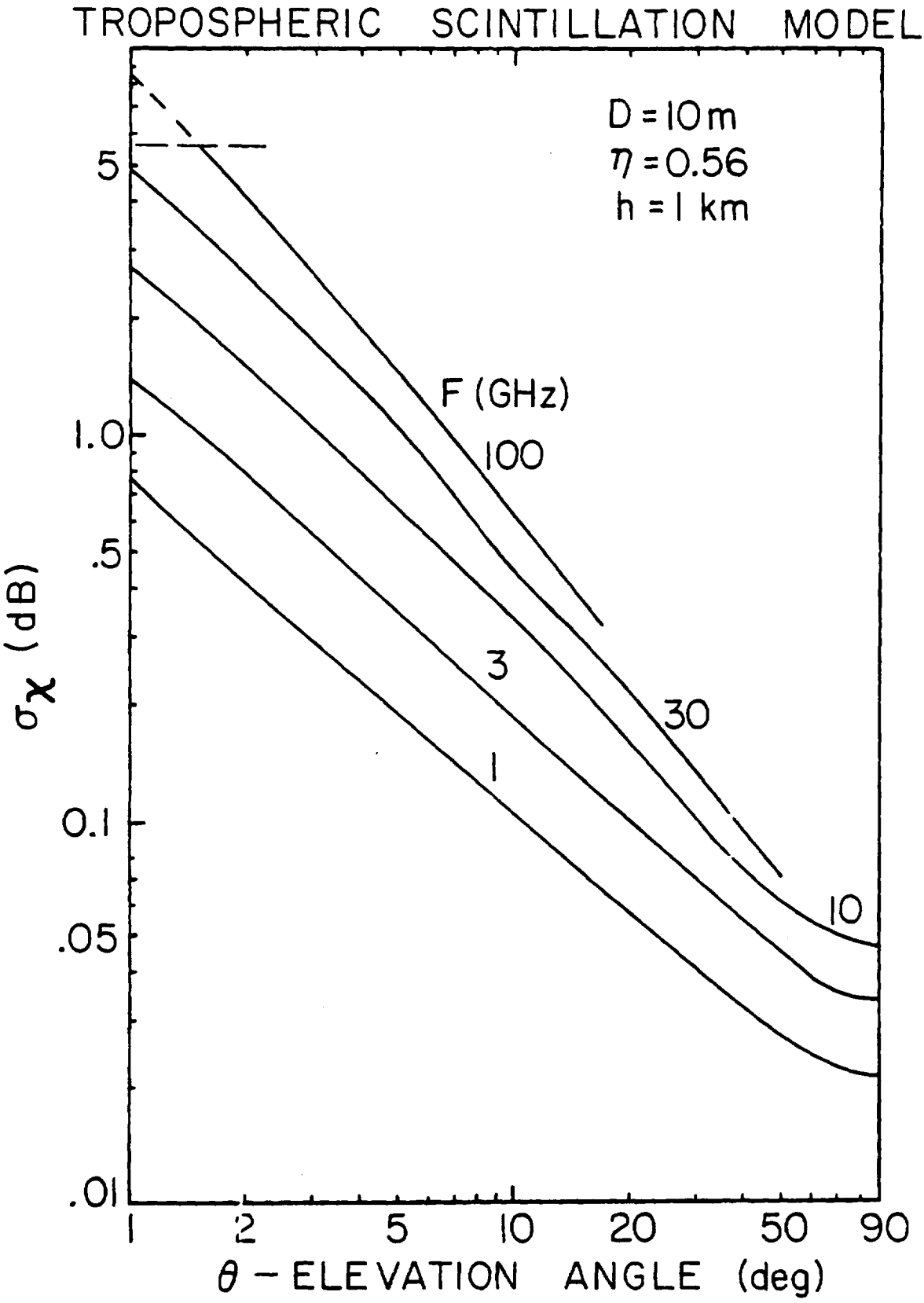

Figure 28 Model predictions of RMS fluctuations for an antenna diameter of 10 meters

2.4 Low Elevation Angle Effects

Observations of slowly setting satellites (Crane, 1976b) show that strong signal amplitude fading (or scintillation) occurred at elevation angles below 2 to 3 degrees due to the troposphere. The strong fading (greater than 5 dB) was a result of a number of randomly occurring multipath events which produced accompanying angle-of-arrival scintillation. During the strong scintillation multipath events, signal depolarization was noted. The change in apparent polarization was presumed to be caused by the response of the antenna (Haystack, 36.6 meter diam., 7.3 GHz) to the multiple signals received at slightly differing angles of arrival. These propagation effects are dominated by large scale refractive index perturbations or layers. They are to be distinguished from weak scintillation effects not only because of larger fading depths but characteristic slower fades, low elevation angle occurrence (below 3 degrees (McCormick and Maynard, 1972) and the associated angle-of-arrival effects.

Another low angle effect of significance to earth-space paths is that due to defocusing (divergence) of the near-horizon rays due to the average atmospheric refractivity profile. Though not a large attenuation effect (order of 1 dB at one degree elevation), an average defocusing persists and should be factored into system margins for geometry involving the low angles.

2.4.1 Atmospheric Multipath

It has generally been accepted and substantiated for microwave point-to-point transmission paths that the mechanism for severe frequency-selective fading is attributable to multiple paths produced within the troposphere by refractive layers (Ruthroff, 1971). The multiple path fading mechanism is also responsible for the low elevation scintillation effects on earth-to-satellite paths (Crane, 1976b; McCormick and Maynard, 1972). Data from Ottawa, Canada (McCormick and Maynard, 1972), 7.3 GHz, have been compiled on a seasonal basis as shown in Figures 29a to d, in terms of percentage distribution. The data base consists of 654 hours of observation on a 9.1 m tracking antenna at elevation angles between 0 and 8 degrees (one degree increments) during the period 1967-1971, grouped into four seasons as indicated. The data were normalized to an "unper-

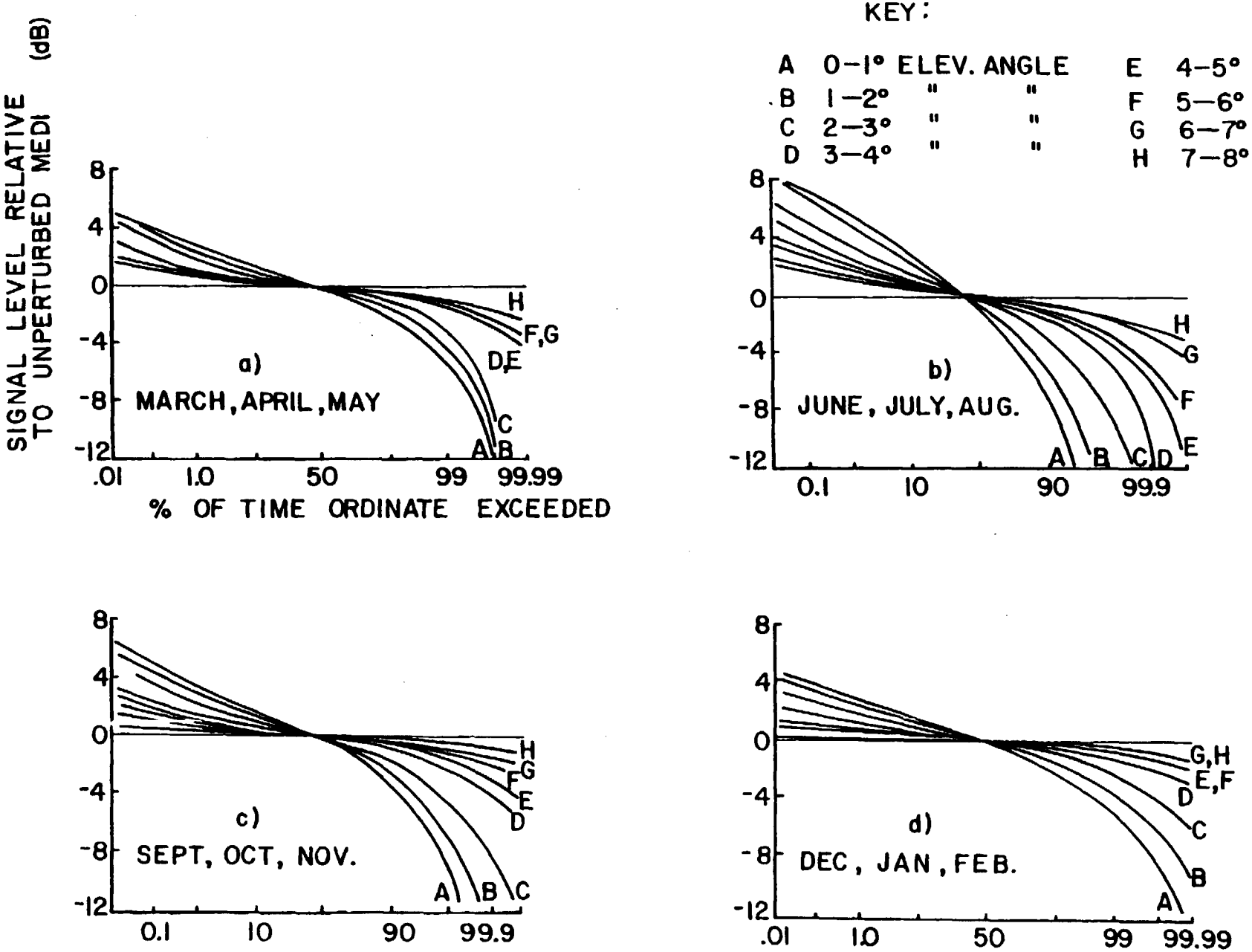

Figure 29 Percentage distribution of signal level relative to median for fading on low elevation earth-to-satellite paths [McCormick and Maynard, 1972]

turbed" 15-minute median signal level (i.e., the median level that would occur in the absence of the fading). The 15-minute period is long enough to contain several of the longest-period fades, and short enough to remove changes in median level due to the motion of the satellite (some were near-geostationary with a slow drift). It is apparent that fading is much worse in summer months than in the winter, with spring and fall intermediate to these extremes. For elevation angles less than 4 degrees, the system margin required to overcome fading undergoes a rapid increase. A sample set of the 15-minute period median level data is shown in Figure 30 as a function of elevation angle. Approximately 300 hours of measurements are shown from Ottawa during a three-week period in October and November 1970 (McCormick and Maynard, 1972). The dashed line represents the median signal level in the absence of losses. The solid line indicates the calculated effect of focusing losses due to regular refraction. The highly nonlinear departure from the solid curve below 3 degrees is attributable to the strong fading due to atmospheric multipath although some ground multipath may influence the measurements below one degree. Figure 31 shows the combined seasonal and elevation effects on fading depth at the 99.9 percent of time exceeded level. The latter provides a means of estimating system fade margins primarily attributable to the low elevation atmospheric multipath effects to be expected over continental locations. For a fixed path length, the fading attenuation distribution would be predicted to go as $1/\lambda$ (λ = free space wavelength) (Ruthroff, 1971). Therefore, an adjustment of fading depths with frequency may be made but exercised with caution, at the users option, due to a pausity of supporting observational data.

2.4.2 Spreading Loss

Signal loss may also result from atmospheric defocusing (focusing loss) which arises due to spreading of the antenna beam caused by the variation of refractive bending with elevation angle at low elevations. Though this effect may be considered negligible for all elevation angles above 5° where focusing losses are of the order of 0.1 dB, the loss term becomes significant below this angle. Figure 32 (Crane, 1976c) shows the focusing loss through the complete atmosphere due to atmospheric refraction effects. These results were obtained by raytracing through numer-

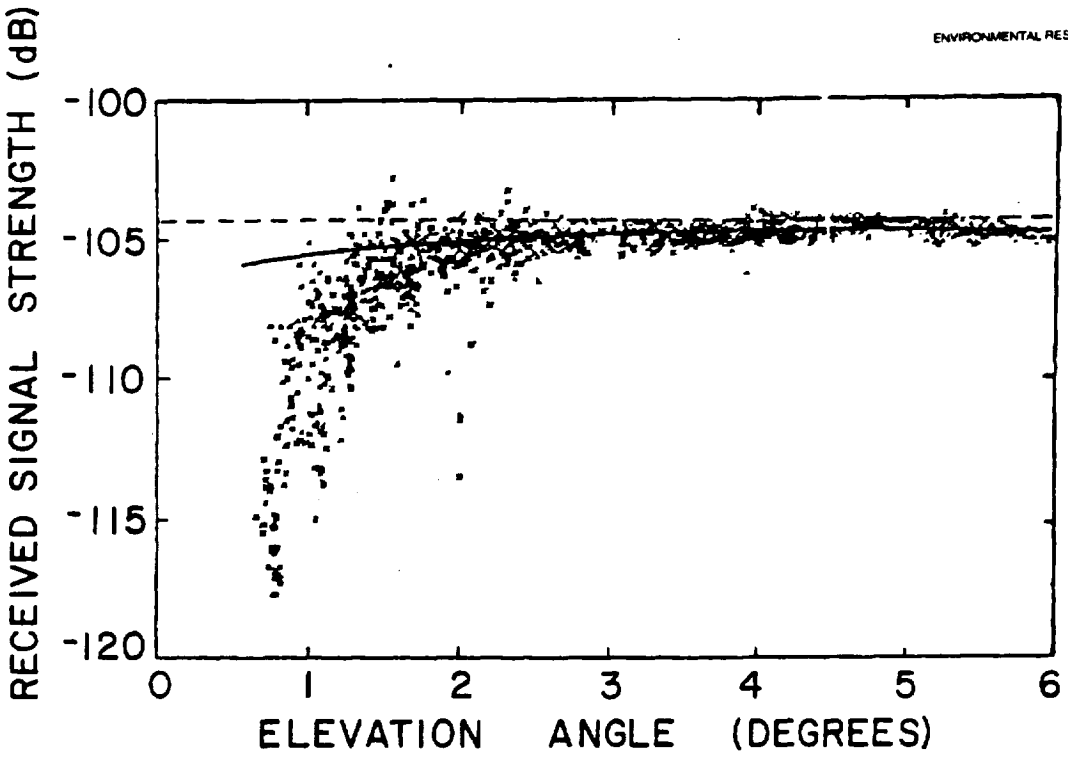

Figure 30 Median signal level as a function of elevation angle [McCormick and Maynard, 1972]

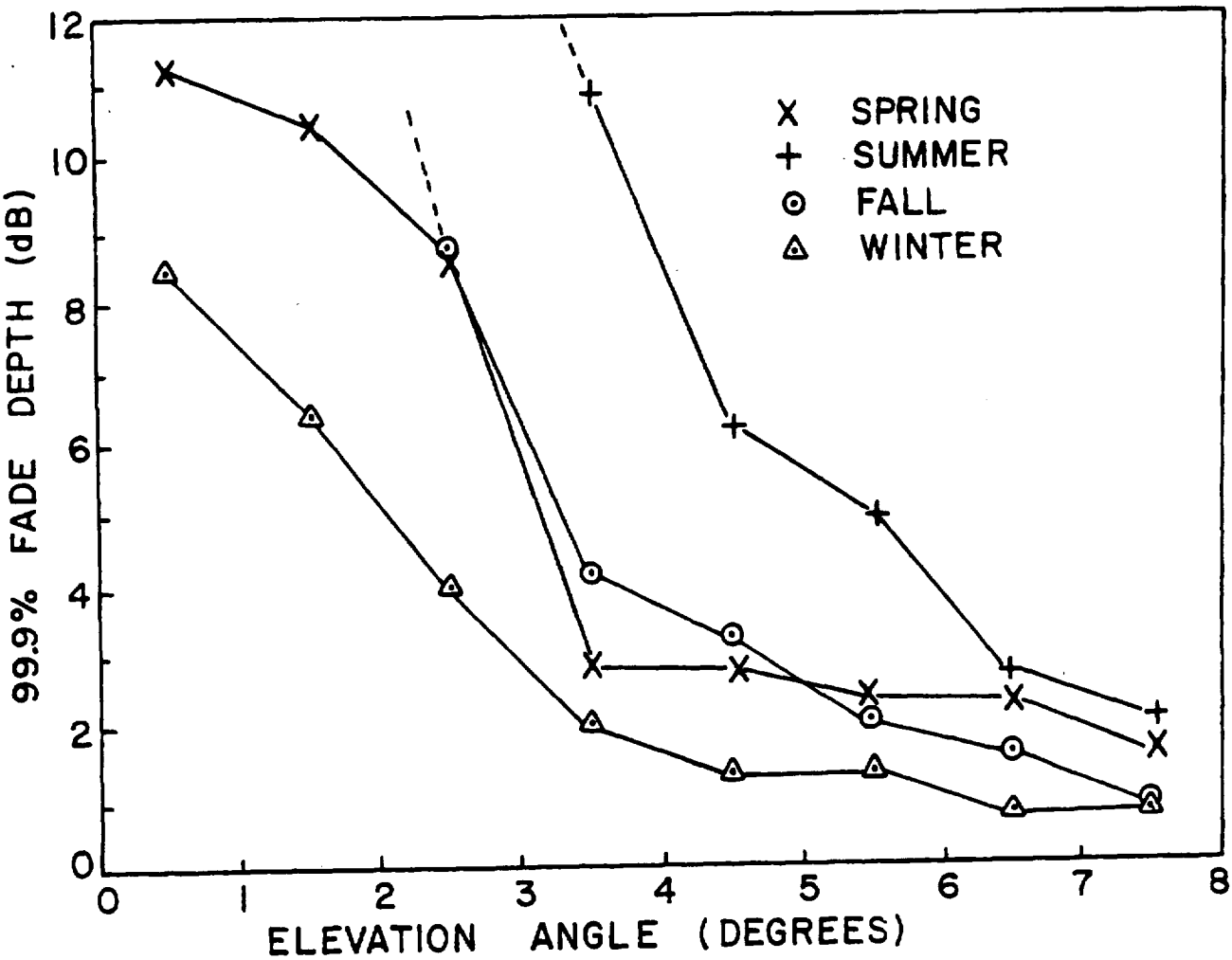

Figure 31 Combined seasonal and elevation effects on fading depth at the 99.9 percent of time exceeded level.

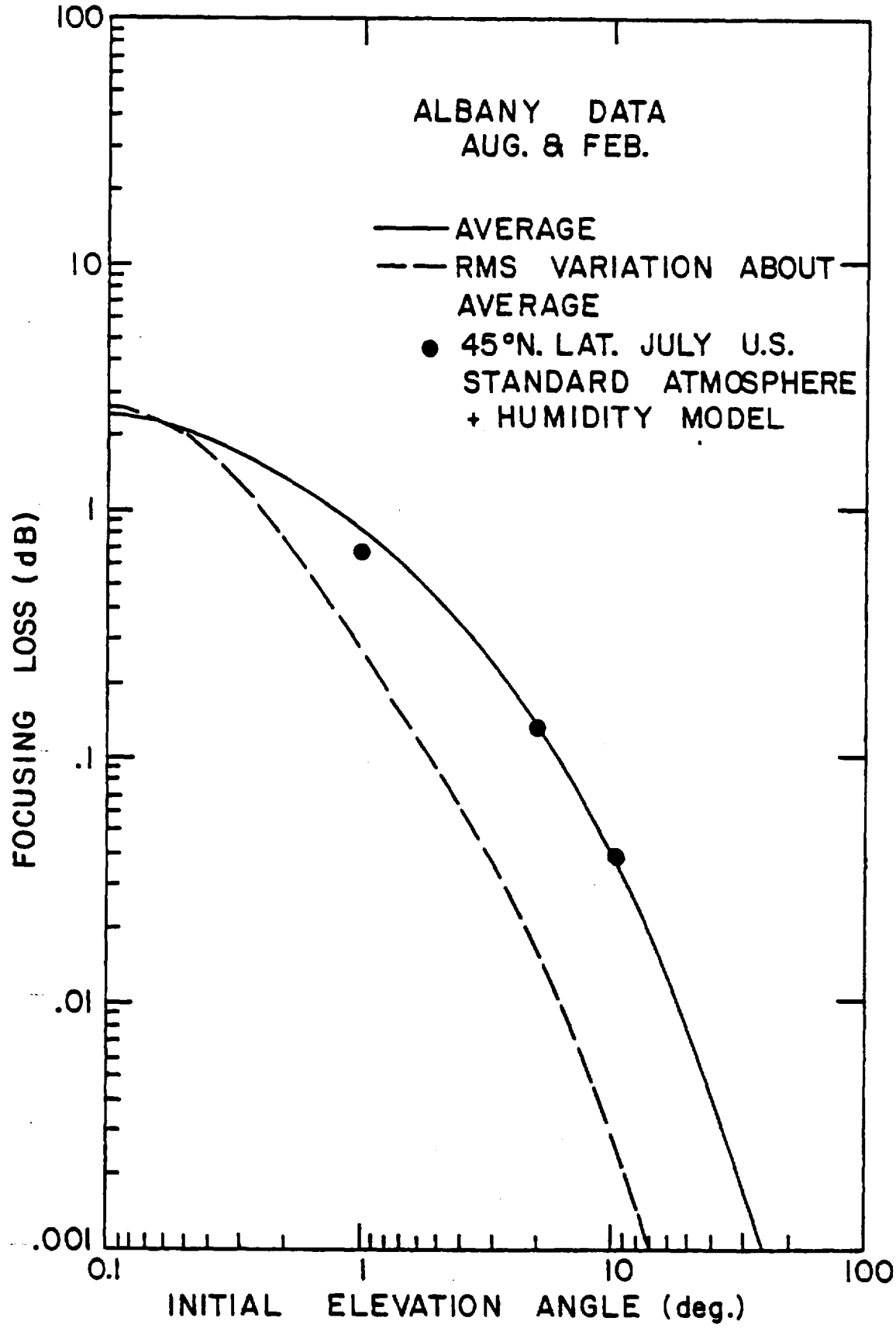

Figure 32 Focusing loss and RMS variation through the atmosphere at low elevation angles due to tropospheric refraction.

ous day and night refractive index profiles from Albany, N.Y. over a several year period. At one degree elevations, the focusing losses are about 0.8 dB±0.3 dB. At the horizon, the loss becomes greater than 2 dB with uncertainties of the same order as the average loss. These effects may be considered typical of effects observed over inland (continental) locations. For sites located near coastal areas, islands, at sea, or in tropical regions, the focusing losses may increase somewhat from these levels due to increased surface refractivity and different near-surface refractive index gradients (see also Yokoi, 1970). Focusing losses should be independent of frequency over the range of 1 to 100 GHz where water vapor is contributing to the refractive profile. The effects due to dry air alone and at higher frequencies have not been estimated but should be less significant.

2.4.3 Procedure

To estimate the system margins for atmospheric multipath and spreading loss at low elevations (below 5 degrees), the following steps may be used:

Step 1 - Obtain the elevation angle ranges of concern for earth-to-space path.

Step 2 - Choose percentage of times to be exceeded for selected system fade margin (e.g., 95%, 99% or 99.9%).

Step 3 - Enter curves of Figures 29a through d (for the four seasons) at appropriate elevation curve and percentages to obtain a table of fading depths L_{fade} (dB) versus season and percentage exceeded.

Step 4 - The effect of frequency on fading depth may now be estimated (at the users option):

$$\Delta dB = 10 \log_{10}\left[\frac{f_{op}}{7.3}\right]$$

where: ΔdB = correction to fading depth due to frequency different than 7.3 GHz

f_{op} = operating frequency (GHz)

This value may be added to all the losses obtained in the table of Step 3. It is not suggested to exercise this option for large frequency departures from 7.3 GHz due to lack of supporting measurements.

Step 5 - Obtain focusing loss L_{focus} (dB) from Figure 32 at the path elevation angle. This value may be considered a constant to be added without regard to percentage of time or season.

Step 6 - The maximum of Step 4 and losses from Step 5 may be retained for the determination of total losses and system margins.

2.5 Radome Attenuation

Though radomes ideally shelter an antenna structure from environmental exposure, some small degrading effects occur due to the radome's transmission loss which further degrades during periods of rain or wetness on the radome.

2.5.1 Dry Conditions

The transmission losses typically experienced due to a radome over an antenna vary with material, thickness, and operating frequency. Typically, the one-way losses (Skolnik, 1970) are designed to be a few tenths of a dB (0.2 to 0.5 dB typical). In some instances the loss L_{dry} may exceed 1 dB due to the rib construction or the need for a thick walled structure. Generally, losses exceeding 1 dB are considered non-optimum designs.

2.5.2 Wet Conditions

A factor often not adequately taken into account in system design is the additional system margin required due to a wet radome, L_{wet}. This effect is produced by a thin layer of water over the radome material due to a steady rainfall or dew condition. Losses exceeding 1 to 2 dB beyond that of normal radome attentuation may be experienced during rain.

2.6 Diversity Schemes

Localized cells of rain attenuation can produce earth-to-space path attenuations and correspondingly, higher noise temperatures at the higher frequencies (above 10 GHz) which tax the system margins for

small percentages of the time. To maintain a required level of reliability (minimum outage time) it may be necessary in some climate regions to employ site-diversity or large scale spatial antenna separations thereby avoiding high attenuations over any single path. In order to design a diversity system for a given location some estimates of rain cell size and separations is needed. From experiments using satellite and radiometric paths in diversity configurations, a data base is becoming available in order to estimate system performance and spacing requirements. It is always somewhat hazardous to generalize a particular set of empirical results to locations for which no data exists and caution should be exercised in the adoption of a simple model for a system design. In addition to direct diversity measurements, weather radar backscatter experiments are yielding measurements of rain-cell size and distribution statistics which are increasingly valuable in diversity system design and estimation.

2.6.1 Earth Terminal Site-Diversity

At any given site location, and period of weather and high rainfall a cluster of rain cells in an array constituting a storm region, may have a particular orientation with respect to the weather fronts passing over the region. The shape and orientation of the storm will have an effect on the diversity system providing two (or more) alternative paths through the region. Figure 33 shows a radar measurement of the structure of a New England summer shower (Crane, 1971). The radar used was the Millstone Hill L-band radar at Westford, Massachusetts having a resolution volume of about 1 km^3 (Crane, 1968).

The radar map of rain intensity shows several small cells with 10 dB down widths the order of 5 km across and peak to minimum rain intensity distances the order of 3 km. The rain rate tabulated along with the Z (radar reflectivity factor) values is computed from Z_e using the approximate expression $Z_e = 200\ R^{1.6}$. Attenuation coefficient estimates are also tabulated for 7.78 GHz. Using a model and calculating the attenuation along the ray from the radar through the shower cells, the attenuations estimate given in Figure 34 results. The data are the estimated values and the lines include the plus and minus rms fluctuations due both to uncertainties in the radar measurements and the drop-size distribution.

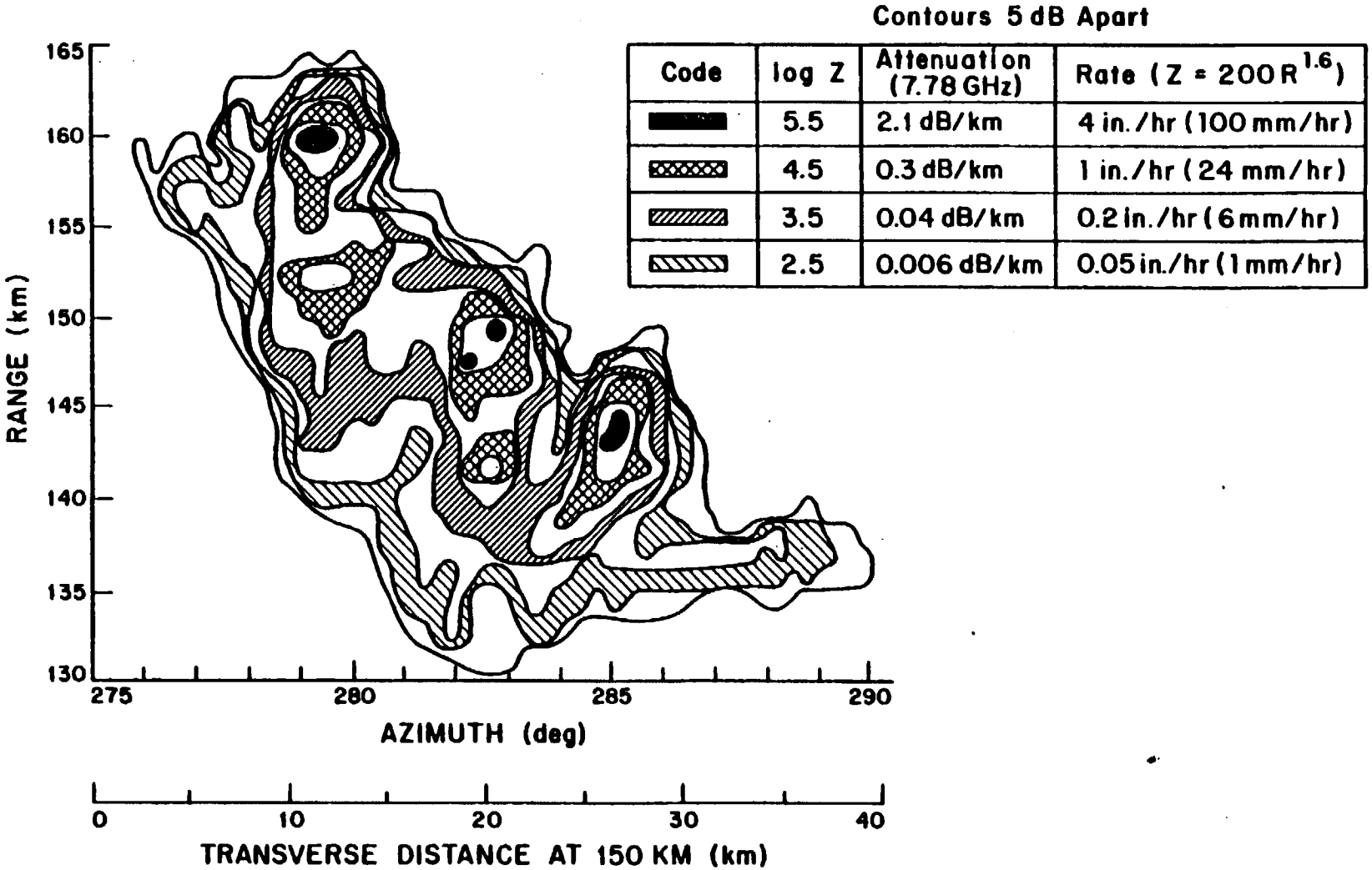

WEATHER RADAR DATA
24 JUL 1967 2052 GMT

MILLSTONE HILL RADAR
1.4° EL, 275°-290° AZ

Figure 33 Weather radar map for New England showers

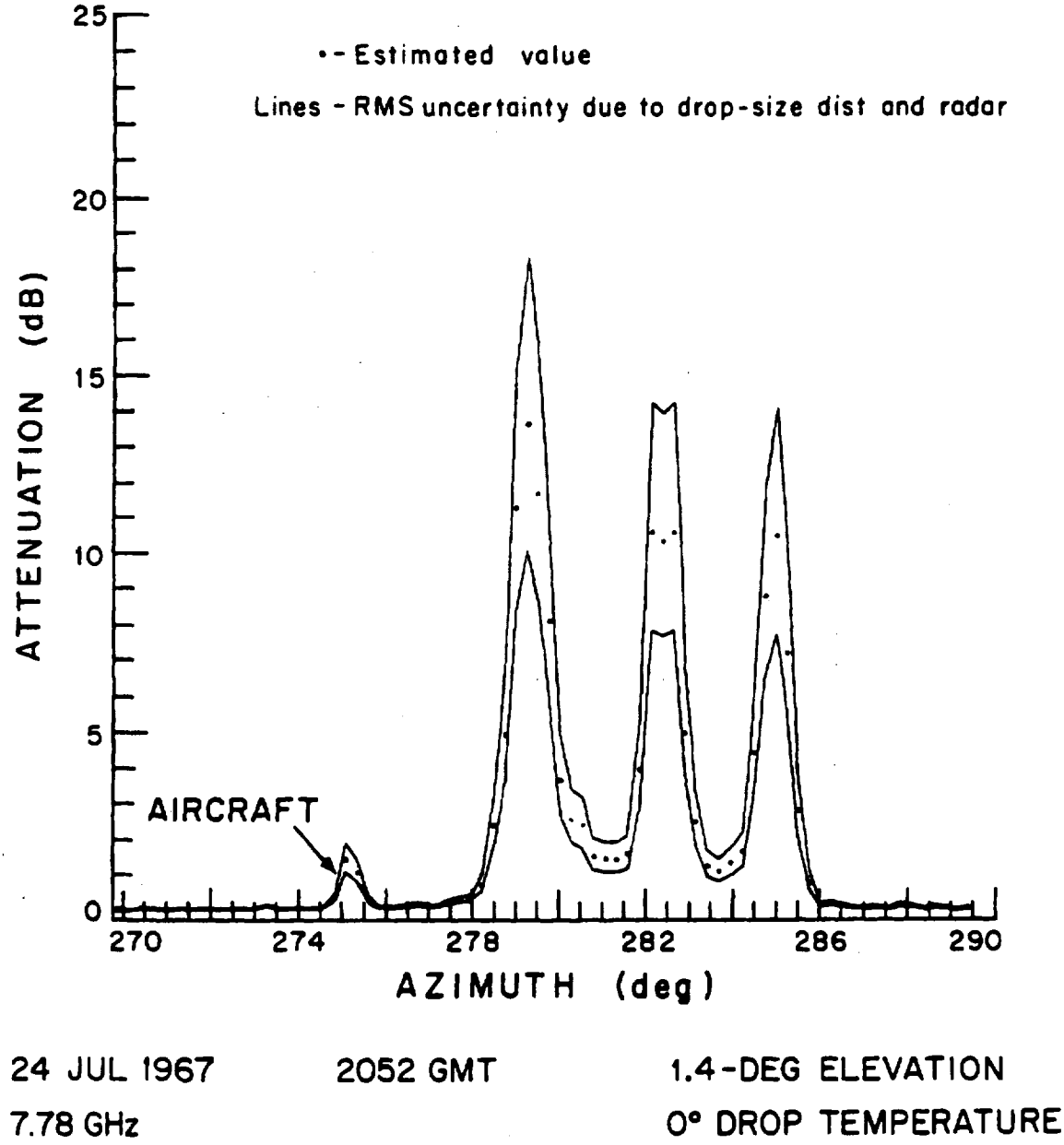

Figure 34 Estimated attenuation using Millstone Hill L-band radar data

From these results it is seen that the significant amounts of attenuation (10 dB or higher at X-band) are contributed by small areas of rain, less than 5 km in extent. Since the cells can be considered to be relatively uniform columns of rain, several km high, a communication path might intercept one or more of these cells depending on orientation. Similarly a set of S-band radar data from Ottawa during 1970 (Strickland, 1974a) was analyzed statistically to determine cell size distributions and joint probabilities of occurrence as a function of two path separation distance. These results showed that 80% of the cells had a size greater than 2 km, 50% exceeded about 6 km, and 20% exceeded 14 km extents for an attenuation level criterion of 3 dB. The attenuations were calculated for 15.3 GHz and compared with satellite (ATS-5) measurements. The cell separation statistics were distances of about 15, 30 and 45 km for the three percentages of occurrence exceeded. Recent measurements from Goodland, Kansas (Crane, 1979) have yielded (3 dB down reflectivity) cell diameters of about 2.5 km with cell separations of 5 to 6 km for all cells and 10 to 12 km for significant cell. Storm sizes of 30 to 60 km in length and 10 to 20 km in width are typically observed nominally agreeing with the Ottawa observations.

Given two (or more) propagation paths, the diversity gain, G, is defined (Hodge, 1974) as the difference in dB between the rain attenuation (A) on a single path and that obtained jointly with diversity paths (A_{div}) at a specified percentage of time exceeded. The diversity gain is therefore a function of the specified level of percentage of time the single path attenuation (or fade depth) is exceeded. A compilation of diversity path experimental data at 15.3 and 16 GHz was performed (Hodge, 1974) and is included in Figure 35. Shown is the two-path diversity gain versus path separation. The parameter in the set of connected data curves is the single path fade depth in dB produced by rain occurrences (not regarding the percentage of time the fade depth was exceeded). It can be noted and defined that diversity gain action begins (G_{div} = about 1 dB) when the single path attenuation reaches about 3 dB. This was achieved on all paths separated by more than 3 km. For a variety of rain climate region D communication paths at frequencies from 12 to 20 GHz (see Figures 16 and 18, Section 2.2), the 3 dB attenuation level is exceeded about 0.2% of the time. Figure 35 shows that most path

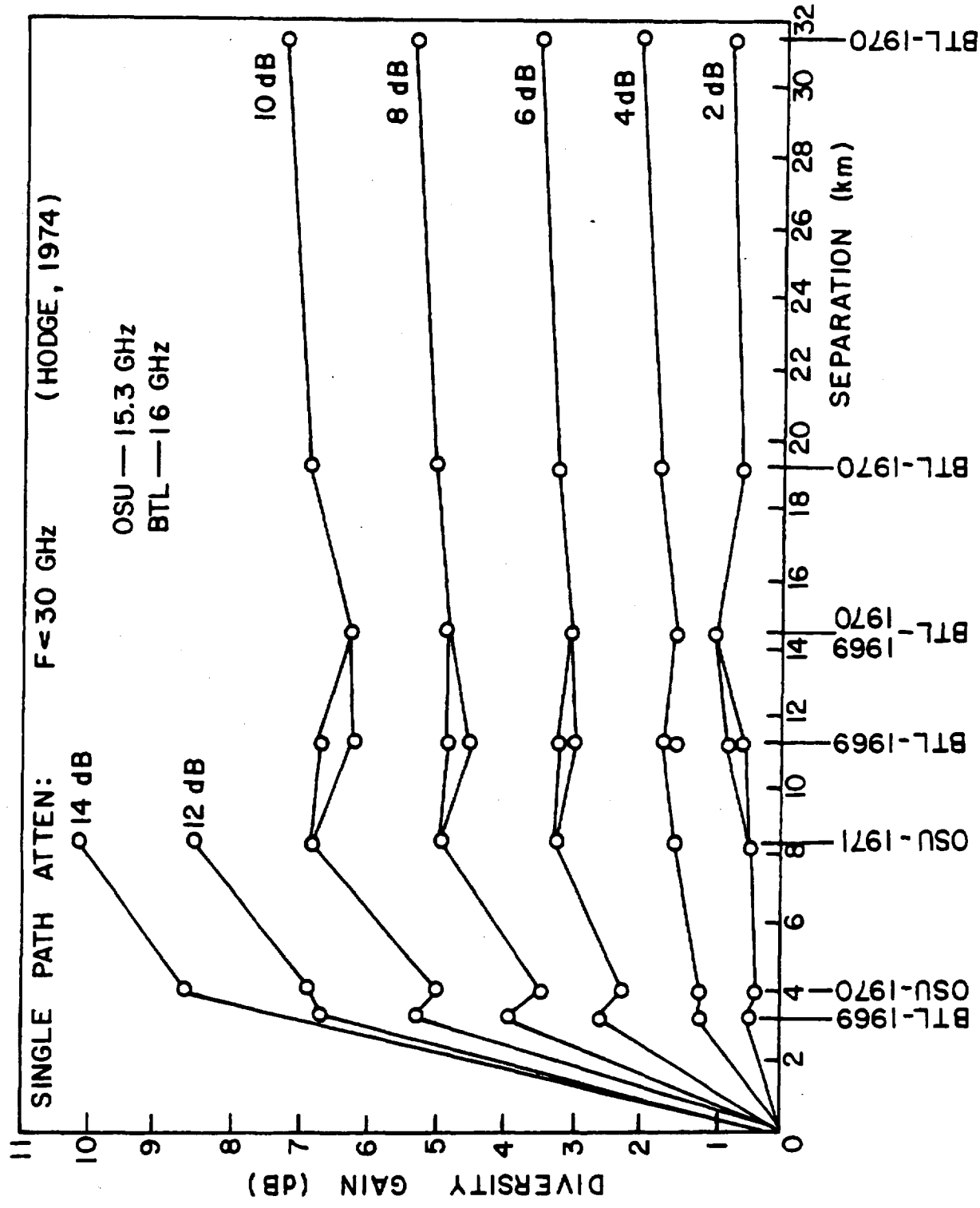

Figure 35 Diversity gain versus site separation [Hodge, 1974]

diversity gain improvement is achieved for paths separated a few km (of the order of one or two rain cell sizes). Beyond some nominal path separation, little improvement is achieved for a much larger path separation.

Caution should be exercised before attempting to apply a family of curves such as Figure 35 or an empirical model extending the concept to perhaps 30 GHz as suggested by Kaul, et al. (1978). The data base was limited to experiments in rain climate region D (New Jersey and Ohio). The model is based solely on attenuation rather than rain rate statistics. The diversity paths forming the model data base were nominally of the same configuration; e.g. NW-SE baseline orientation, elevation angles of 35°, azimuth angles of 220°, and link frequencies below 20 GHz. Therefore, the use of the model is not recommended for general application and for propagation paths departing significantly from the conditions and not at all for frequencies above 30 GHz.

To analyze the requirements for site diversity separation in rain climate region D ($F \lesssim 30$ GHz) one should first proceed with a path rain attenuation distribution analysis (Section 2.2). Once the single-path attenuation versus percent of year exceeded curve is obtained, the minimum site (path) separations may be estimated using the 15 GHz curves of Figure 35. The working level of fade depth (attenuation) permissible at the fading margin designed will thereby specify the diversity path separation required for protection against outages.

2.6.2 Satellite Terminal Techniques

Since spaced satellites analogous to site-diversity for the purpose of spatial diversity alone is both impractical from a cost standpoint and generally incompatible with narrow beam earth terminals it will not be considered an option. What may be allowable is multiple satellite paths from one earth terminal using dual antennas. This becomes impractical for rain occurrences near the earth terminal.

Options that may be open, in lieu of spatial separation diversity are frequency diversity and time diversity. The former requires shifting to a lower frequency band (usually at the sacrifice of a reduced information bandwidth) when attenuation exceeds the system margin. The latter also compromises information by some form of repeated message when outages occur.

The techniques of space, time or frequency diversity for the purpose of reducing short term outages such as due to scintillation will not be discussed. These subjects are adequately treated in communication texts and rely more heavily on hardware considerations than on propagation problems which may be circumvented.

2.7 Link Calculation

The total minimum received power (P_r) for the communication link system margin calculation may be estimated taking into account all of the gains and losses discussed in the previous sections:

$$P_r' = P_t + G_t - L_b - L_{atm} - A_{rain} - L_{scint} - L_{fade} - L_{focus} - L_{radome} + G_{div} + G_r \quad (1)$$

where the terms are defined as:

P_r' = minimum received power expected (dBW)

P_t = transmitted power (dBW)

G_t = transmitting antenna power gain (dB)

L_b = basic transmission loss due to free space

$= 10 \log_{10} \left[\frac{16\pi^2 R^2}{\lambda^2}\right]$, R = total path length (same units as λ)

L_{atm} = total attenuation due to atmospheric gases, Section 2.1 (dB)

A_{rain} = path attenuation due to rain, Section 2.2 (dB)

L_{scint} = loss due to tropospheric scintillation, Section 2.3 (dB)

L_{fade} = loss due to low elevation fading, Section 2.4 (dB)

L_{focus} = loss due to low elevation defocusing (or spreading), Section 2.4 (dB)

$L_{radome} = L_{dry} + L_{wet}$ = total radome loss expected, Section 2.5 (dB)

G_{div} = system diversity gain, Section 2.6 (dB)

G_r = receiving antenna power gain (dB)

$$= 10 \log_{10} \left[\frac{4\pi A_e}{\lambda^2}\right]$$

A_e = receiving antenna effective aperture (same units as λ^2) = $\eta \cdot A$

A = physical aperture of receiving antenna

η = aperture efficiency factor

Given that a link is required to maintain a specified signal carrier-to-noise level (R = S/N), the system fade margin (F) may be considered to be the protection built into the system design against variable propagation losses:

$$F_{dB} = A_{rain} + L_{scint} + L_{fade} + L_{wet} \text{ (dB)} \quad (2)$$

The combined signal-to-noise is:

$$S/N \text{ total} = R_{dB} + F_{dB} = P_r - P_n \quad (3)$$

where:

R_{dB} = required signal-to-noise under worst conditions (dB)

F_{dB} = designed system fade margin (dB)

P_r = received power under normal conditions (dBW)

P_n = total received noise power (dBW)

The required system fade margin, combining the fixed propagation losses (L_p) is therefore:

$$F_{dB} = P_t - P_N + G_t + G_r + G_{div.} - L_p - R_{dB} \quad (4)$$

where:

L_p = fixed propagation losses

$$= L_b + L_{atm.} + L_{focus} + L_{dry} \text{ (dB)}$$

3. RECEIVER NOISE

Though natural radio noise can be caused by other sources, the principal sources are due to atmospheric emission, the radio sky (such as the sun, Cassiopeia, and Cygnus), earth reradiation, and antenna contributions. These sources are to be distinguished from interference (man-made noise), a topic requiring separate treatment. The discussion will be limited to the noise producing the sensitivity limit on surface-based antennas looking skyward. The principal natural sources of noise emission are those of atmospheric origin encountered in the main antenna lobe and the low elevation energy from earth reradiation entering the side lobes of the antenna. Specifically, the areas considered will be limited to the microwave emission of the atmospheric gases, rain emission, and thermal noise contributions due to the antenna. The radio sky noise background and scattered energy sources are omitted or assumed to be sufficiently small to be neglected. Consequently, strong extraterrestrial noise sources, such as the sun, will be assumed to be out of the main lobe of the antenna.

Unlike the earth terminal, the satellite terminal experiences radiation from the earth and cloud tops within the main lobe as well as the atmospheric emissions. With larger antenna beam widths (smaller apertures), the satellite antenna system is usually constrained by other system design considerations (beyond the scope of this report) than sensitivity alone. The background noise and man-made interference are inseparable when considering the satellite terminal, as opposed to the earth terminal, and set the noise floor with which the up-link receiving system works.

3.1 Emission by Atmospheric Gases

The atmospheric gases, water vapor and oxygen, emit energy in the microwave region of the electromagnetic spectrum. The frequencies at which emission is strongest correspond to the absorption bands discussed in Section 2.1. The sky temperature (T_s) along a ray path can be expressed (Crane, 1971) as:

$$T_s = \int_o^S T(S)\beta(S)\ \exp\left[-\int_o^S \beta(x)dx\right] dS \qquad (1)$$

where: T_s = sky temperature at given ray angle (°K);

$T(S)$ = kinetic temperature of the gas at a position S along the ray (°K);

$\beta(S)$ = attenuation cross section per unit volume of the gas at position S along the ray;

= A/10 log e = A/4.34, where A is attenuation coefficient in dB per unit length.

The power received at the antenna is due to thermal noise or the apparent antenna temperature (T_a). The apparent temperature is composed of several terms including antenna temperature due to atmospheric emission (T_A). To enumerate other sources, T_a has contributions due to extra-terrestrial noise sources, hydrometeor emission, atmospheric scattered earth radiation, cloud emission and sources picked up by antenna side-lobes. If the noise source has an angular area larger than the antenna beamdwidth, the temperature of this source determines the antenna temperature contribution. The term due to atmospheric emission is expressed by the integral over the solid angle:

$$T_A = 1/4\pi \int_o^{4\pi} G(\Omega)\ T_s(\Omega)d\Omega \qquad (2)$$

where: T_A = antenna temperature due to atmospheric emission (°K);

$G(\Omega)$ = antenna angular gain function;

$T_s(\Omega)$ = sky temperature from equation (1) as a function of angle; and

Ω = unit solid angle (ster radians).

The antenna temperature may be approximated by:

$$T_A \approx \eta \cdot T_s(0) \qquad (3)$$

where: η = antenna efficiency

$$= \frac{Ae}{A} = \frac{\text{effective aperture}}{\text{physical aperture}} \text{ ; and}$$

$T_s(0)$ = on-axis sky temperature.

Using the approximation of horizontal stratification of the atmosphere, the sky temperature (T_s) may be computed given the temperature and humidity profiles appropriate to a specific location. Figure 36 shows the results of a computation of sky temperature (Crane, 1971) for several elevation angles together with measured values of $T_s = T_A/\eta$ by Wulfsberg (AFCRL) in Massachusetts. Good agreement is obtained at all elevation angles except the lowest at 15 and 17 GHz. The point of departure between the measured and calculated data occurred when the close-in sidelobes began to intercept the earth's surface. Some of the discrepancies are also due to profile measurement uncertainty. The dashed lines correspond to an approximation to equation (1) that assumes a cosecant law for the attenuation and a total attenuation of less than 1 dB. It is seen that the cosecant form of the approximation holds well for elevation angles above 10 degrees for 15 and 17 GHz, and above 15 degrees at 35 GHz.

The sky temperaure (T_s) as a function of elevation angle (Θ) and frequency (from 1 to 100 GHz) is shown in Figures 37, 38 and 39 (CCIR, 1978b) for three different surface humidity conditions. The computations are based on theory and assumptions cited in the reference and are for surface heights (sea level) and 20°C surface temperatures (293°K). The three absolute humidity values (ρ = 3, 10, 17 g/m^3) correspond to relative humidities of 17, 58 and 98 percent, respectively.

The thermal noise power contribution due to atmospheric emission alone is:

$$P_N = k\, T_A\, B = k\, \eta\, T_s(\Theta,F) B \qquad (4)$$

where: k = Boltzmann's constant = 1.38×10^{-23} (watt-sec/°K);

η = antenna efficiency;

T_s = on-axis sky temperature as a function of elevation angle (Θ) and operating frequency (F) from Figures 37, 38 or 39 as appropriate to location; and

B = received I.F. noise bandwidth (Hz).

Since there is variability in the value of T_s principally due to humidity in the atmosphere (depending on frequency), a refinement of the estimation procedure for atmospheric noise, such as accounting for site altitude, is probably not merited. The variability in T_s due to humidity may be estimated by comparing the values from Figures 37, 38 and 39.

3.2 Emission by Rain

The measurement of microwave emission by rain is usually accomplished with radiometric techniques. If the absorption loss and mean radiating temperature are known, the sky temperature due to rain emission may be computed by:

$$T_s = T_m \left(1 - \frac{1}{L}\right) \qquad (°K) \qquad (5)$$

where: T_m = mean radiating temperature of rain (°K); and

L = loss factor due to absorbing medium.

Simultaneous measurements of the sky temperature (T_s) during rainfall and corresponding satellite attenuation measurements (e.g., Ippolito, 1971; Strickland, 1974b; and Hodge, 1978), have generally compared favorably with attenuation from the calculations. The effective medium temperature (T_m) assumed ranges from 270° to 278°K from the references cited. To obtain the sky temperature, the procedures of Section 2.2 for rain attenuation may be followed. The resulting loss (factor) is used in equation (5) with a T_m estimated from surface temperature (Wulfsberg, 1964) by:

$$T_m = 1.12\, T_o - 50 \qquad (°K) \qquad (6)$$

where: T_o = temperature at the surface (°K)

Estimates of sky temperature increase due to rainfall as a function of rain rate are also available (Otsu, 1971) for ATS-5 satellite measurements at 15 and 35 GHz.

The ultimate deleterious effects on earth-to-space communication links due to a rain occurrence, therefore, are both an attenuation of the received signal strength and an increase in the noise level (antenna temperature, $T_A = \eta \cdot T_s$) beyond that attributable to the clear atmosphere.

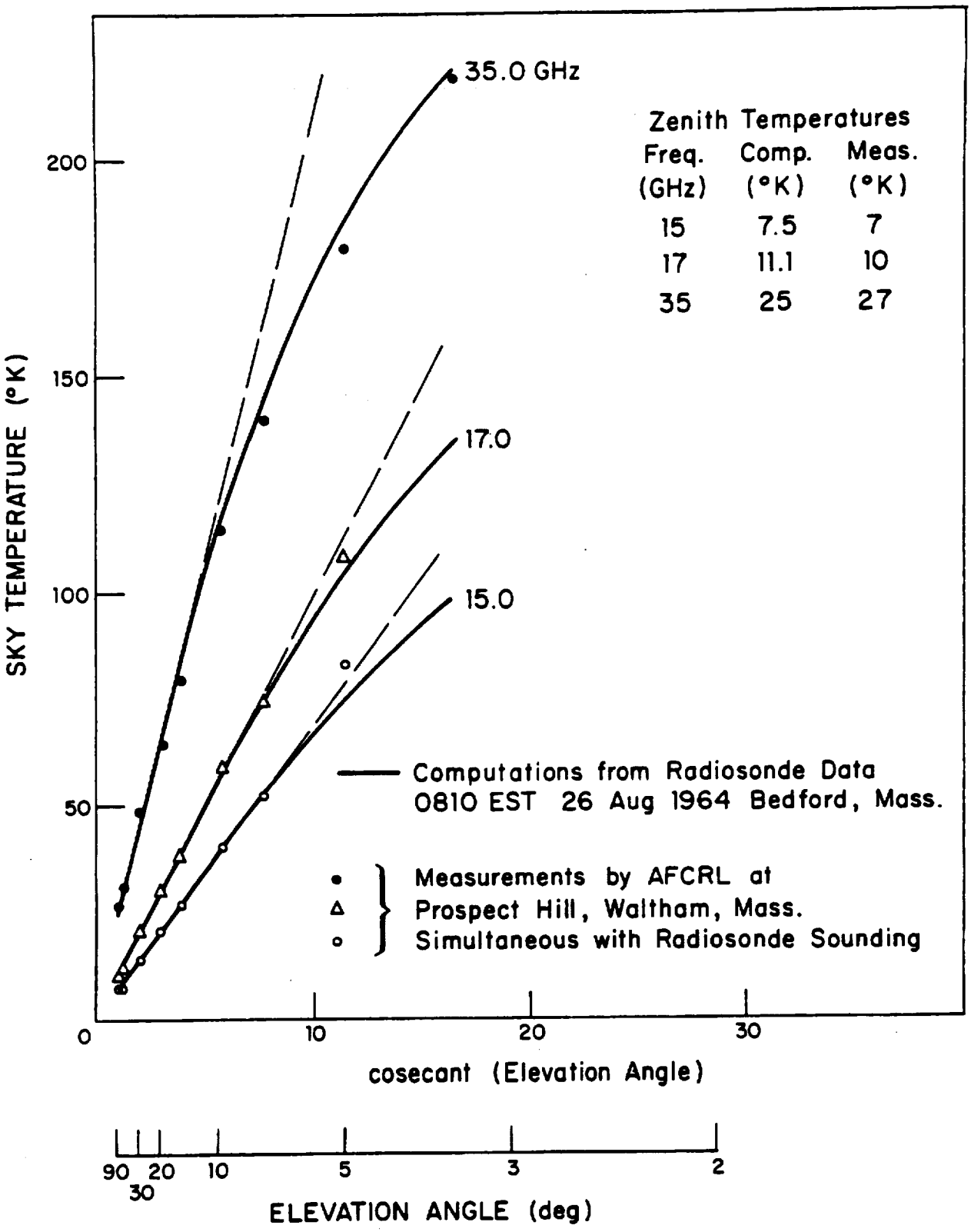

Figure 36 Comparison between measured and computed sky temperature

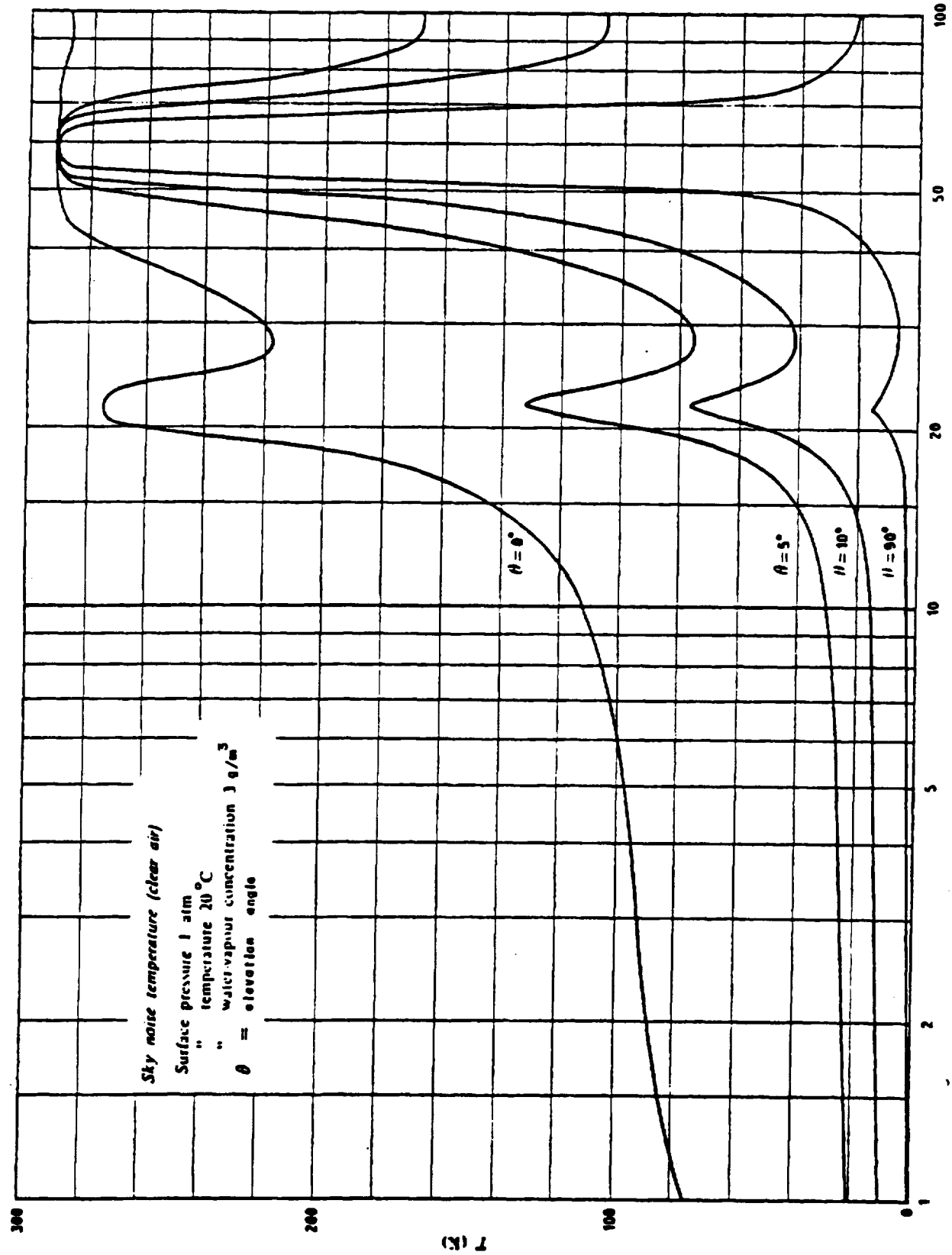

Figure 37 Sky noise temperature (clear air) at 3 g/m^3 surface water-vapor concentration

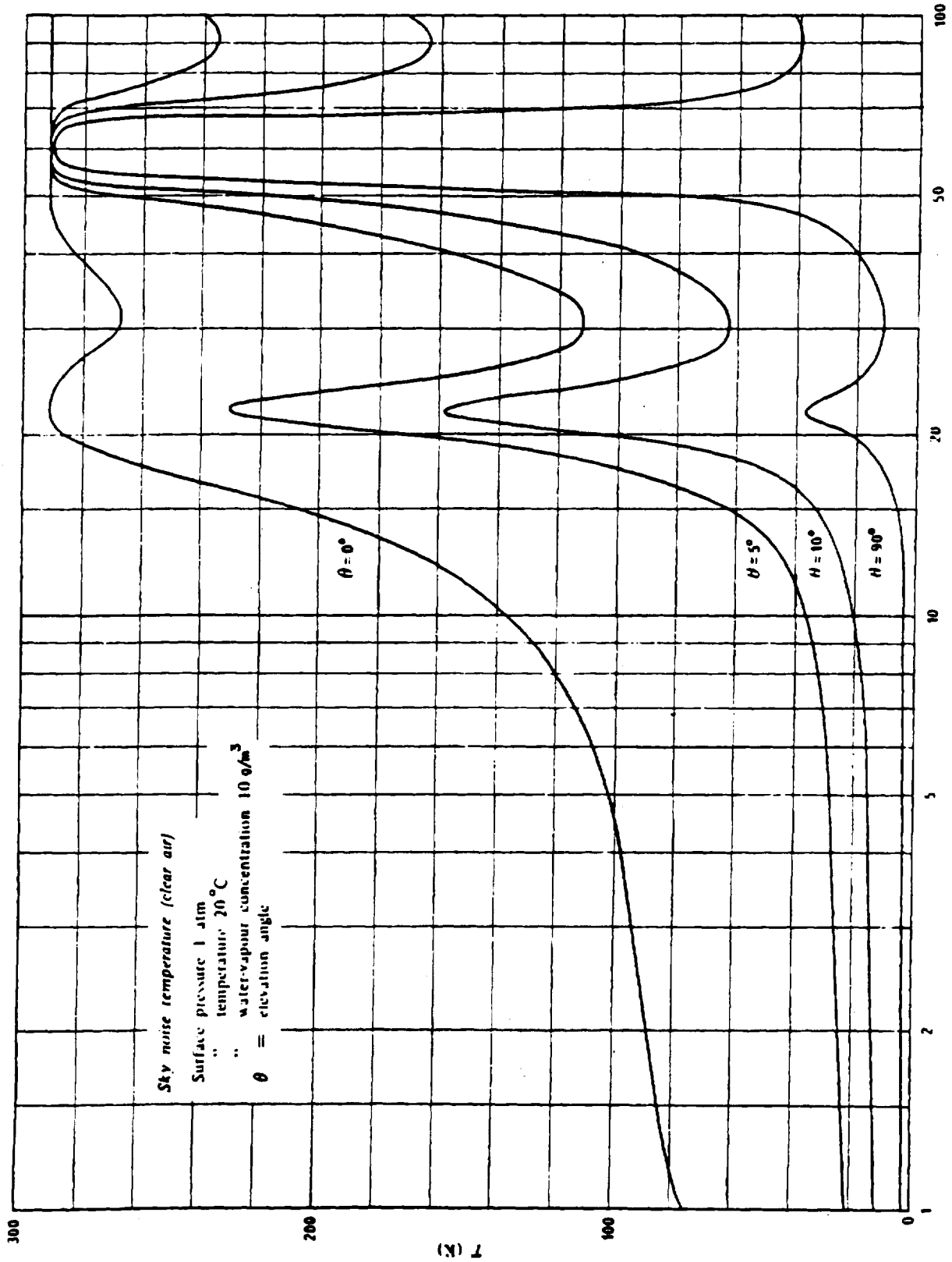

Figure 38 Sky noise temperature (clear air) at 10 g/m^3 surface water-vapor concentration

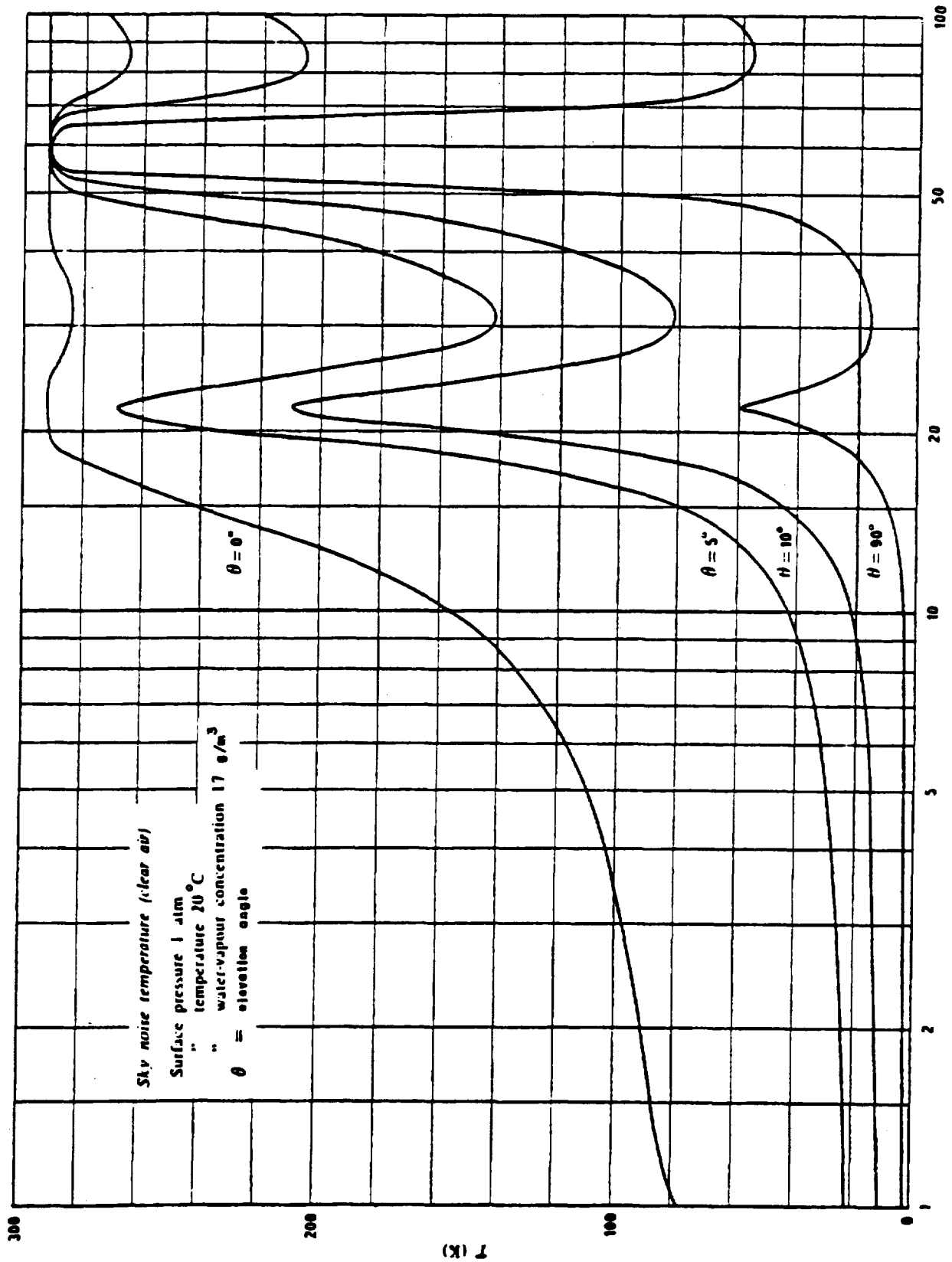

Figure 39 Sky noise temperature (clear air) at 17 g/m^3 surface water-vapor concentration.

3.3 Antenna Contributions

For a narrow beam antenna pointed above the horizon, a source of noise contributing to the antenna temperature T_A, additional to that discussed in Section 3.1 and 3.2) is due to sidelobe contributions. This noise can be significant since the ground provides a relatively high temperature source. The effect of the integrated sidelobe contribution is a reduction in the main-beam efficiency for antennas that have relatively high sidelobe levels. Shielding to reduce the emission from nearby ground surfaces can improve the performance.

For low elevation angles (near the horizon) the noise contribution from the ground and horizon temperatures may be particularly significant with the antenna temperature approaching that of the surface (T_o). The model for antenna temperature increase versus decreasing elevation angle depends both on the specific antenna design (and near side lobe antenna pattern structure) and the particular terrain features in the vicinity the antenna faces near the horizon. These design considerations are also beyond the scope of treatment here.

CONCLUSION

This report covers only the propagation path loss and noise considerations for earth-to-space communication links operating at frequencies from 1 to 300 GHz. Several topics are not addressed in this report, to be a subsection of the complete microwave propagation effects handbook. A treatment of the interference effects: intersymbol; interpolarization; and intersystem; is deferred to a subsequent contribution to the handbook. Users of this report are urged to submit comments and suggestions for improvement to the authors.

REFERENCES

Arnold, H.W., D.C. Cox, H.H. Hoffman and R.P. Leck, 1979: "Rain Attenuation Statistics from a 19 and 28 GHz COMSTAR Becon Propagation Experiment: One Year Cumulative Distributions and Relationships between Two Frequencies", IEEE Trans. Comm. (accepted for publication).

Baxter, R.A. and D.B. Hodge, 1978: "Spectral Characteristics of Earth-Space Paths at 2 and 30 GHz", Technical Report 784299-7, Ohio State University ESL, August.

Bean, B.R. and E.J. Dutton, 1966: Radar Meteorology, NBS Monograph 92, U.S. Dept. of Commerce, National Bureau of Standards, Boulder, Colorado, U.S. Government Printing Office, March.

CCIR, 1976: "Ionospheric Effects Upon Earth-Space Propagation", Report 263-3, Contained in Document 6/177-E dated 17 May 1976, CCIR Study Group 6 on Ionospheric Propagation, Geneva, 17 May 1976, 86-117.

CCIR, 1977: Report 5/270, CCIR XIV the Plenary Assembly, Kyoto, 1978, Draft Document 5/1024-E dated 23 Nov. 1977.

CCIR, 1978a: "Rain Attenuation Prediction", CCIR Study Groups, Special Preparatory Meeting (WARC-79) Doc. P/105-E, dated 6 June 1978, International Telecommunications Union, Geneva.

CCIR, 1978b: Report 5/269, CCIR XIVth Plenary Assembly, Kyoto, 1978, Draft Document 5/1925-E dated 11 January 1978.

Crane, R.K., 1966: "Microwave Scattering Parameters for New England Rain", MIT, Lincoln Laboratory, Lexington, Mass., Tech. Rept. 426, ASTIA Doc. AD647798, October.

Crane, R.K., 1968: "Simultaneous Radar and Radiometer Measurements of Rain Shower Structure", Technical Note 1968-33, Lincoln Laboratory, MIT, ASTIA Doc. AD-678079, September.

Crane, R.K., 1971: "Propagation Phenomena Affecting Satellite Communication Systems Operating in the Centimeter and Millimeter Wavelength Bands", Proc. IEEE, 59, February, 173-188.

Crane, R.K., 1976: "An Algorithm to Retrieve Water Vapor Information from Satellite Measurements", NEPRF Tech. Rept. 7-76 (ERT), Final Report, Project No. 1423, Environmental Research & Technology, Inc., November.

Crane, R.K., 1976a: "Spectral of Ionospheric Scintillation", J. Geophysical Res., Vol. 81, No. 13, May, 2041-2050.

Crane, R.K., 1976b: "Low Elevation Angle Measurement Limitations Imposed by the Troposphere: An Analysis of Scintillation Observations Made at Haystack and Millstone", Tech. Rept. 518, Lincoln Laboratory, MIT, May.

Crane, R.K., 1976c: Refraction Effects in the Neutral Atmosphere, Chapter 2.5 - Methods of Experimental Physics, Vol. 12, Astrophysics, Part B, Academic Press, New York.

Crane, R.K., 1977: "Ionospheric Scintillation", Invited Paper, Proc. IEEE, 65, February, 180-199.

Crane, R.K., 1977a: "Prediction of the Effects of Rain on Satellite Communication Systems", Proc. IEEE, Vol. 65, March, 456-474.

Crane, R.K., 1978: "Variance and Spectra of Angle-of-Arrival and Doppler Fluctuations Caused by Ionospheric Scintillation", J. Geophysical Res., Vol. 63, No. A5, May, 2091-2102.

Crane, R.K., 1979: "Automatic Cell Detection and Tracking", submitted to IEEE Trans. Geoscience Electronics.

Crane, R.K., 1979b: "Prediction of Attenuation by Rain", Paper submitted to IEEE Transactions on Communications, July.

Goldhirsh, J., 1979: "Cumulative Slant Path Rain Attenuation Statistics Associated with the COMSTAR Beacon at 28.56 GHz for Wallops Island, Virginia", IEEE Trans. Antennas and Propagation, AP-27 (accepted for publication).

Harris, J.M. and G. Hyde, 1977: "Preliminary Results of COMSTAR 19/29 GHz Beacon Measurements at Clarksburg, Maryland", COMSAT Tech. Review, 7, 599-623.

Hodge, D.B., 1974: "Path Diversity for Reception of Satellite Signals", Publication of IUCRM Colloquium, Nice, France, 23-31 October 1973, Journal de Recherches Atmospheriques, Vol. VIII, Nos. 1-2, 443-449.

Hodge, D.B., D.M. Theobold and R.C. Taylor, 1976: "ATS-6 Millimeter Wavelength Propagation Experiment", Report 3863-6, Ohio State University ESL.

Hodge, D.B., 1978: "Meteorological Radar Calibration", Technical Report 784650-1, Ohio State University ESL, February.

Ippolito, L.J., 1971: "Effects of Precipitation on 15.3 and 31.65 GHz Earth-Space Transmissions with the ATS-V Satellite", Proc. IEEE, 59, February, 189-205.

Ippolito, L.J., 1976: "20 and 30 GHz Millimeter Wave Experiments with ATS-6 Satellites", NASA TND-8197, NASA Goddard Space Flight Center, Greenbelt, Maryland.

Ippolito, L.J., 1979: "11.7 GHz Attenuation and Rain Rate Measurements with the Communications Technology Satellite (CTS)", NASA Tech. Memo. 80283, NASA Goddard Space Flight Center, Greenbelt, Maryland.

Kaul, R., D.B. Hodge and D.M. Theobold, 1978: Prediction of Millimeter Wave Propagation Effects on Earth-Space Paths, Technical Report 1418, ORI, Inc., Silver Spring, Maryland, for NASA/Goddard Space Flight Center, December.

Kinase, A. and A. Kinpara, 1973: "Statistics of Attenuation Due to Pieciketation of Radio Waves in 12 GHz Band at Higher Angles of Elevation", Note 101, NHK Tech. Res. Labs, Tokyo, Japan.

Laws, J.O. and D.A. Parsons, 1943: "The Relation of Raindrop-Size to Intensity", Am. Geophys. Union Trans., 24, 452-460.

McCormick, K.S. and L.A. Maynard, 1972: "Measurements of S.H.F. Tropospheric Fading Along Earth-Space Paths at Low Elevation Angles", Electronic Letters, Vol. 8, No. 10, May, 274-276.

Nackoney, D., 1978: "CTS 11.7 GHz Beacon Data", Technical Note TN 78-471.3, GTE Laboratories, Inc.

Olsen, R.L., D.V. Rogers and D.B. Hodge, 1978: "The aR^b Relation in the Calculation of Rain Attenuation", IEEE Trans. Antennas and Propagation, AP-26, 318-329.

Otsu, Yichi, 1971: "Measurement of Sky Noise Temperature at 16 GHz and 35 GHz", J. Radio Res. Labs., Vol. 18, 96, March, 87-911.

Rustako, A.J., 1979: "Measurement of Rain Attenuation and Depolarization of the CTS Satellite Beacon Signal at Holmdel, N.J." (abstract only), USNC-URSI Spring Meeting, Seattle, Washington.

Ruthroff, C.L., 1971: "Multiple-Path Fading on Line-of-Sight Microwave Radio Systems as a Function of Path Length and Frequency", Bell System Technical Journal, September, 2375-2398.

Skolnik, M.I.(ed.), 1970: Radar Handbook, Ch. 14, McGraw-Hill.

Strickland, J.I., 1974a: "Radar Measurements of Site-Diversity Improvement During Precipitation", Publication of IUCRM Colloquium, Nice, France, 23-31 October 1973, Journal de Recherches Atmospheriques, Vol. VIII, Nos. 1-2, 451-464.

Strickland, J.I., 1974b: "The Measurement of Slant Path Attenuation Using Radar, Radiometers and a Satellite Beacon", Publication of IUCRM Colloquium, Nice, France, 23-31 October 1973, Journal de Recherches Atmospheriques, Vol. VIII, Nos. 1-2, 347-358.

Stutzman, W.L. and G.W. Bostian, 1979: "A Millimeter Wave Attenuation and Depolarization Experiment using the COMSTAR and CTS Satellite", Final Report SATCOM-79-2, Virginia Polytechnic Institute and State Univ., Blacksburg, Virginia; U.S. Army Research Office, Grant No. PAAG 29-77-G-0083.

Tatarski, V.I., 1967: The Effects of the Turbulent Atmosphere on Wave Propagation, Nanka, Moscow (translation available - U.S. Dept. of Commerce, NTIS, Spring Hill, Virginia, 1971).

Valentin, R., 1977: "Statistiken der Regendämpfung fur Richtfunkverbindungen über 10 GHz", Deutsche Bundespost Forschungsinstitet beim FTZ, Report 455-TB-62.

Vogel, W.J., 1979: "CTS Attenuation and Cross Polarization Measurements at 11.7 GHz", Final Report Cont. NAS5-22576, Electrical Engineering Research Laboratory, Univ. of Texas at Austin.

Waters, J.W., 1976: "The Microwave Spectrum of the Atmosphere" in Methods of Experimental Physics, Vol. 12B, Astrophysical Methods (Meeks, ed.), Chapt. 2.3, Academic Press.

Wulfsberg, K.N., 1964: "Apparent Sky Temperatures at Millimeter-Wave Frequencies", Phys. Science Res. Paper No. 38, Air Force Cambridge Research Lab., No. 64-590, July.

Yokoi, H., M. Yamada and T. Satoh, 1970: "Atmospheric Attenuation and Scintillation of Microwaves from Outer Space", Astronomical Society, Vol. 22, 4, Japan, 511-524.